

# THÈSE DE DOCTORAT

Modélisation Tensorielle de l'ECG pour  
l'Analyse de la Fibrillation Atriale Persistante

Pedro Marinho Ramos de Oliveira

Laboratoire d'Informatique, Signaux et Systèmes de Sophia Antipolis (I3S)  
UMR7271 Université Côte d'Azur CNRS

Présentée en vue de l'obtention du  
grade de Docteur en Automatique,  
Traitement du Signal et des Images  
d'Université Côte d'Azur.

Dirigée par: Vicente Zarzoso

Soutenue le: 2 Octobre 2020

Devant le jury, composé de:

Vicente Zarzoso, Université Côte d'Azur - Directeur de thèse

Laurent Albera, Université de Rennes 1 - Rapporteur

José Joaquín Rieta, Universidad Politécnica de Valencia - Rapporteur

Luca Mainardi, Politecnico di Milano - Examinateur

Maxime Sermesant, INRIA Sophia Antipolis - Examinateur

Gérard Favier, CNRS - Président



UNIVERSITÉ CÔTE D'AZUR  
**ÉCOLE DOCTORALE STIC**  
SCIENCES ET TECHNOLOGIES DE L'INFORMATION  
ET DE LA COMMUNICATION

**THÈSE DE DOCTORAT**

pour obtenir le grade de

**Docteur en Automatique, Traitement du Signal et  
des Images**

d'Université Côte d'Azur

Présentée par

PEDRO MARINHO RAMOS DE OLIVEIRA

**Modélisation Tensorielle de l'ECG  
pour l'Analyse de la Fibrillation  
Atriale Persistante**

Dirigée par: Vicente Zarzoso

Laboratoire d'Informatique, Signaux et Systèmes de Sophia Antipolis (I3S)  
UMR7271 Université Côte d'Azur CNRS

Soutenue publiquement le 2 Octobre 2020

**Jury:**

<i>Directeur:</i>	Vicente Zarzoso	- Professeur, Université Côte d'Azur, France
<i>Rapporteurs:</i>	Laurent Albera	- Maître de conférence, Université de Rennes 1, France
	José Joaquín Rieta	- Professeur, Universidad Politécnica de Valencia, Espagne
<i>Examinateurs:</i>	Luca Mainardi	- Professeur, Politecnico di Milano, Italie
	Maxime Sermesant	- Chercheur, Inria Sophia Antipolis, France
<i>Président:</i>	Gérard Favier	- Directeur de recherche, CNRS, France



# Résumé

La fibrillation atriale (FA) est l'arythmie soutenue la plus couramment diagnostiquée dans la pratique clinique. Elle est responsable de taux élevés d'hospitalisation et de décès. Les mécanismes électrophysiologiques qui sous-tendent ce trouble du rythme cardiaque ne sont pas complètement compris. Une stratégie non invasive et efficace pour étudier cette arythmie consiste à analyser l'activité atriale (AA) présente dans l'électrocardiogramme (ECG) de surface. Toutefois, l'AA est masquée par l'activité ventriculaire (AV) dans chaque battement, et elle a une amplitude faible, ce qui rend difficile son analyse.

Au fil des années, des méthodes de traitement du signal ont aidé les cardiologues pour l'étude de la FA en extrayant l'AA de l'ECG. En particulier, des méthodes matricielles de séparation aveugle de sources (SAS) se sont révélées des outils d'extraction de l'AA efficaces. Cependant, certaines contraintes doivent être imposées pour garantir l'unicité de ces techniques de factorisation matricielle et, bien que mathématiquement cohérentes, elles peuvent manquer de fondements physiologiques, avec pour conséquence d'entraver l'interprétation des résultats.

En revanche, les décompositions tensorielles peuvent garantir l'unicité sous des contraintes moins restrictives. En particulier, la décomposition en termes de blocs (*Block Term Decomposition*, BTD), récemment proposée comme technique SAS, peut être unique sous certaines contraintes satisfaites par les facteurs matriciels, facilement vérifiées tant du point de vue mathématique que physiologique. Par ailleurs, les sources cardiaques peuvent être bien modélisées par des fonctions mathématiques spécifiques qui, lorsqu'elles sont mappées dans les facteurs matriciels structurés de la BTD, présentent un lien avec leur rang. Un autre avantage par rapport aux méthodes matricielles est que l'approche tensorielle est capable d'extraire l'AA à partir d'enregistrements ECG très courts.

Dans la présente thèse de doctorat, on étudie tout d'abord le modèle Hankel-BTD comme outil d'extraction d'AA dans des épisodes de FA persistante, avec une validation basée sur des expériences statistiques concernant une population de patients atteints de FA et plusieurs types de segments ECG. Les enregistrements ECG avec des intervalles courts entre les battements cardiaques et de l'AA à faible amplitude sont des cas difficiles courants à ce stade de l'arythmie. Ces cas motivent l'utilisation d'une autre approche tensorielle, appelée Löwner-BTD, pour estimer un signal AA de meilleure qualité. Une telle approche est présentée dans le cadre d'une nouvelle stratégie optimale pour assurer la structure de Löwner qui est implémentée comme une variante d'un algorithme robuste récemment proposé pour le calcul de la BTD. Une autre contribution est la modélisation des ECG en FA persistante par le modèle dit de Hankel-BTD couplé, qui offre une meilleure extraction d'AA avec un coût de calcul réduit par rapport à son homologue non couplé.

D'autres contributions concernent les défis qui découlent du problème de l'extraction d'AA des ECG de FA, tels que la détection de la source d'AA parmi d'autres sources séparées dans des expériences réelles, où la vérité est inconnue. Pour cette tâche, plusieurs approches utilisent des algorithmes d'apprentissage automatique et des réseaux de neurones sont évaluées, offrant une précision satisfaisante. Un autre défi à relever est la difficulté de mesurer la qualité de l'estimation de l'AA. De nouveaux indices sont proposés et évalués pour quantifier la qualité de l'estimation AA sur l'enregistrements ECG pendant la FA.

En résumé, cette thèse de doctorat fournit la première étude approfondie de l'application des techniques de traitement du signal tensoriel pour l'analyse de la fibrillation atriale, en mettant en évidence l'intérêt de l'approche tensorielle et son potentiel pour la prise en charge et la compréhension de ce trouble cardiaque complexe.

**Mots clés:** Décomposition en Terme de Bloc, Décompositions Tensorielles, Électrocardiogramme, Fibrillation Atriale, Séparation des Sources.



# Abstract

Atrial Fibrillation (AF) is the most common sustained arrhythmia diagnosed in clinical practice, responsible for high hospitalization and death rates. Furthermore, the electrophysiological mechanisms underlying this cardiac rhythm disorder are not completely understood. A non-invasive and efficient strategy to study this challenging cardiac condition is analyzing the atrial activity (AA) from the electrocardiogram (ECG). However, the AA during AF is masked by the ventricular activity (VA) in each heartbeat and often presents a very low amplitude, hampering its analysis.

Throughout the years, signal processing methods have helped cardiologists in the study of AF by extracting the AA from the ECG. In particular, matrix-based blind source separation (BSS) methods have proven to be efficient AA extraction tools. However, some constraints need to be imposed to guarantee the uniqueness of such matrix factorization techniques that, although mathematically coherent, may lack physiological grounds and hinder results interpretation.

In contrast, tensor decompositions can ensure uniqueness under more relaxed constraints. Particularly, the block term decomposition (BTD), recently proposed as a BSS technique, can be unique under some constraints over its matrix factors, easily satisfying in the mathematical and physiological sense. In addition, cardiac sources can be well modeled by specific mathematical functions that, when mapped into the structured matrix factors of BTD, present a link with their rank. Another advantage over matrix-based methods is that the tensor approach is able to extract AA from very short ECG recordings.

The present doctoral thesis has its first focus on the investigation of the Hankel-BTD as an AA extraction tool in persistent AF episodes, with validation based on statistical experiments over a population of AF patients and several types of ECG segments. ECG recordings with a short interval between heartbeats and an AA with significantly low amplitude are challenging cases common in this stage of the arrhythmia. Such cases motivate the use of other tensor-based approach to estimate an AA signal with better quality, the Löwner-BTD. Such an approach is presented along a novel optimal strategy to ensure the Löwner structure that is implemented as a variant of a recently proposed robust algorithm for BTD computation. Another contribution is the model of persistent AF ECGs by a coupled Hankel-BTD, which shows some advantages in terms of improved AA extraction and reduced computational cost over its non-coupled counterpart.

Further contributions focus on challenges that arise from the problem of AA extraction from AF ECGs, such as detecting the AA source among the other separated sources in real experiments, where the ground truth is unknown. For this task, several approaches that use machine learning algorithms and neural networks are assessed, providing satisfactory accuracy. Another challenge that is dealt with is the difficulty in measuring the quality of AA estimation. Here, new indices for AA estimation quality from ECG recordings during AF are proposed and assessed.

In summary, this PhD thesis provides the first thorough investigation of the application of tensor-based signal processing techniques to the analysis of atrial fibrillation, showing the interest of the tensor approach and its potential in the management and understanding of this challenging cardiac condition.

**Keywords:** Atrial Fibrillation, Block Term Decomposition, Electrocardiogram, Source Separation, Tensor Decompositions.



*I dedicate this work to my parents, Nertan and Hylana*





# Acknowledgments

In the first place, I thank God for giving me the gift of life and all the conditions I needed to conclude this important part of my career, my PhD. During this 3-year path, He put incredible people in my life that helped me to become a better professional and human being.

I thank my family, in special my parents Nertan Oliveira and Hylana Oliveira, for their infinite love and support not only during the period of my thesis, but ever since I can remember. To them, I'll be eternally grateful.

A special thanks to the person that believes in me more than myself, who is by my side no matter the circumstances, Paloma Meneses. My dear, thanks is not enough to express my gratitude for having you in my life.

To be supervised by a great researcher is the dream of many and the opportunity of few, which makes me very grateful to have Vicente Zarzoso as my thesis supervisor. Thank you, Vicente, for showing me the beauty of science. You trusted in my potential, giving me amazing opportunities that helped me to become a better researcher. I hope we can keep collaborating and also sharing some "geladinhas" once in a while.

Arriving in another country without knowing properly the spoken language and how bureaucracy works can make your life difficult. Fortunately, I was not alone. I can't help but thanks my amazing landlady Sherazade Bessa for helping me a lot in many situations, the Welcome Center department of Université Côte d'Azur for solving several administrative problems for me, and of course, my fellow countrymen Danilo, Danielle, Henrique, Luana, Pablo, Kallynna, Leandro, Guilherme, Lucas and Yuri, for so many things that if I write them all here it will give a whole chapter.

A very deep gratitude to the I3S Laboratory and all the amazing people I met there. In particular, I thank Gérard Favier, Rodrigo Cabral and Sylvie Icart for all the help and interesting discussions, Viviane Rosello for helping me with the academic mission documents, and my co-office workers Muhammad Haziq and Amina Ghrissi for all the support and good times at the office.

When I arrived in France, I was expecting to make new friends. Instead, I made pals that I am going to keep for life. The list is long, but I can't help citing Jean-Marie, Miguel, Melissa, Mohit, Davide, Ninad and Fernando, who were with me since the beginning of my journey. I must also mention Francisco, Antonio, Eva, Yao, Piotr, Oussama, Melpomeni, Dimitris, Mircea, Diana and Cyprien. Thank you guys for the incredible moments we shared, of which some I remember, others not so much, especially when they start with a "Po po po pooooor que bebes, companheiro?". I thank also all the staff of Akathor and Pompeï, the best pubs in Nice!

From Brazil, I thank my former supervisor Carlos Alexandre for all the help in my thesis and Walter Freitas for interesting discussions and collaborations. During my vacations in Brazil, I wasn't expecting less than amazing and unforgettable moments, for this I must thank all the members of the SoP, Tiago, Felipe, Giorgio, Juan, Rodrigo, Filipe, and all my friends from the Universidade Federal do Ceará in Sobral.

Finally, I would like to thank all the Jury Members of my PhD defense for the significant time and effort that they have dedicated to reviewing my thesis manuscript and for their valuable comments and suggestions that have allowed me to improve its quality and presentation. They were able to do an excellent work despite the difficult times that we are facing due to the Covid-19 pandemic.



# **Tensor Modeling of the ECG for Persistent Atrial Fibrillation Analysis**

**Pedro Marinho Ramos de Oliveira**



---

# Notation

Scalars, vectors, matrices, and tensors are represented, respectively, by lower-case ( $a, b, c, \dots$ ), boldface lower-case ( $\mathbf{a}, \mathbf{b}, \mathbf{c}, \dots$ ), boldface capital ( $\mathbf{A}, \mathbf{B}, \mathbf{C}, \dots$ ), and calligraphic ( $\mathcal{A}, \mathcal{B}, \mathcal{C}, \dots$ ) letters. If nothing else is explicitly stated, the meaning of the following symbols are:

$(\cdot)^T$	- matrix transpose
$\hat{(\cdot)}$	- estimate of its argument
$\ \cdot\ _2$	- $l_2$ -norm
$\ \cdot\ _{2,1}$	- matrix mixed $l_{2,1}$ -norm, defined as the sum of the $l_2$ -norms of its argument's columns
$\ \cdot\ _F$	- Frobenius norm
$ \cdot $	- absolute value
$E[\cdot]$	- mathematical expectation
$\text{diag}(\cdot)$	- builds a diagonal matrix by placing its vector argument along the diagonal
$D_i(\mathbf{A})$	- represents the diagonal matrix with the $i^{\text{th}}$ row of a matrix $\mathbf{A}$ forming its diagonal
$\text{bdiag}(\cdot)$	- builds a block diagonal matrix by placing its vector or matrix argument along the diagonal
$\text{vec}(\cdot)$	- builds a column vector by stacking the columns of its matrix argument
$\circ$	- outer product
$\otimes$	- Kronecker product
$\diamond$	- Khatri-Rao product (column-wise Kronecker product)
$\odot$	- Khatri-Rao product (partition-wise Kronecker product)
$\diamond_K$	- block Khatri-Rao product
$\mathbf{I}_N$	- identity matrix of order $N$
$\mathbf{1}_N$	- a column vector of ones of length $N$
$\mathbf{0}_{M \times N}$	- a matrix of zeros of dimensions $M \times N$

Given a third-order tensor  $\mathcal{A} \in \mathbb{C}^{I \times J \times K}$ , with scalars  $a_{i,j,k}$ , its frontal slices are represented by  $\mathbf{A}_{..k} \in \mathbb{C}^{I \times J}$ . Given a matrix  $\mathbf{A} \in \mathbb{C}^{I \times J}$ , with scalar entries  $a_{i,j}$ , its  $i$ th row and the  $j$ th column are represented by  $\mathbf{a}_i$  and  $\mathbf{a}_j$ , respectively. When not stated otherwise, the mean and standard deviation are represented by  $\mu$  and  $\sigma$ , respectively.



# List of Acronyms

AA	- Atrial Activity
ABS	- Average Beat Subtraction
AF	- Atrial Fibrillation
AGL	- Alternating Group Lasso
ASVC	- Adaptive Singular Value Cancellation
AUC	- Area Under the ROC Curve
AV	- Atrioventricular
BSS	- Blind Source Separation
BTD	- Block Term Decomposition
CA	- Catheter Ablation
CAGL	- Constrained Alternating Group Lasso
CNN	- Convolutional Neural Network
CV	- Cross Validation
DF	- Dominant Frequency
DFT	- Discrete Fourier Transform
ECDF	- Empirical Cumulative Distribution Function
ECG	- Electrocardiogram
FFT	- Fast Fourier Transform
HR	- Heart Rate
HRV	- Heart Rate Variability
ICA	- Independent Component Analysis
LA	- Left Atrium
LCAGL	- Löwner-Constrained Alternating Group Lasso
LS	- Least Squares
LV	- Left Ventricle
NLS	- Non-Linear Least Squares
NSR	- Normal Sinus Rhythm
PCA	- Principal Component Analysis
PVI	- Pulmonary Vein Isolation
RA	- Right Atrium
RV	- Right Ventricle
SA	- Sinoatrial
SC	- Spectral Concentration
SLRA	- Structured Low-Rank Approximation
SVD	- Singular Value Decomposition
VA	- Ventricular Activity
WCT	- Wilson Central Terminal
WS	- Window Slicing

# Contents

<b>List of Figures</b>	vii
<b>List of Tables</b>	xi
<b>I Introduction</b>	1
<b>1 Thesis Overview</b>	3
1.1 Context and motivation . . . . .	3
1.2 Objectives . . . . .	4
1.2.1 General objectives . . . . .	4
1.2.2 Specific objectives . . . . .	4
1.3 Database and preprocessing . . . . .	4
1.4 Thesis structure and contributions . . . . .	5
1.5 Scientific production . . . . .	7
1.5.1 Journals . . . . .	7
1.5.2 Conferences . . . . .	8
<b>2 Fundamentals of Cardiology</b>	9
2.1 Introduction . . . . .	9
2.2 The human heart . . . . .	9
2.3 Cardiac conduction system . . . . .	10
2.4 Principles of electrocardiography . . . . .	11
2.5 The 12-lead electrocardiogram system . . . . .	14
2.5.1 Limb leads . . . . .	14
2.5.2 Augmented limb leads . . . . .	14
2.5.3 Precordial leads . . . . .	15
2.5.4 Interpretation and preprocessing . . . . .	16
2.6 Arrhythmias . . . . .	16
2.7 Atrial fibrillation . . . . .	17
2.7.1 Statistics . . . . .	17
2.7.2 Mechanisms . . . . .	17
2.7.3 Classification . . . . .	19
2.7.4 Treatments . . . . .	20
2.8 Summary . . . . .	21
<b>3 Noninvasive Atrial Activity Extraction</b>	23
3.1 Introduction . . . . .	23
3.2 Average beat subtraction . . . . .	23
3.3 Weighed average beat subtraction . . . . .	24
3.4 Spatio-temporal QRST cancellation . . . . .	25
3.5 Adaptive singular value cancellation . . . . .	25
3.6 Other methods for VA suppression . . . . .	26
3.7 Blind source separation . . . . .	27
3.7.1 Principal component analysis . . . . .	27
3.7.2 Independent component analysis . . . . .	28

3.8	Summary	30
<b>4</b>	<b>Concepts of Tensor Algebra</b>	<b>31</b>
4.1	Introduction	31
4.2	Introduction to multilinear algebra	31
4.3	Tensor decompositions	34
4.3.1	PARAFAC decomposition	34
4.3.2	Tucker-3 decomposition	36
4.3.3	PARATUCK decomposition	38
4.4	Block term decomposition	39
4.5	Coupled block term decomposition	40
4.6	Hankel-BTD as an AA extraction tool	41
4.7	Summary	43
<b>II</b>	<b>Contributions</b>	<b>45</b>
<b>5</b>	<b>Quantification of AA Content and Source Classification</b>	<b>47</b>
5.1	Introduction	47
5.2	Indices for AA quantification	48
5.3	Automated methods for source classification	50
5.3.1	Classical method	50
5.3.2	Proposed method 1	50
5.3.3	Proposed method 2	51
5.3.4	Experimental data and setup	51
5.3.5	Source analysis and classification	52
5.4	Machine learning approach for source classification	53
5.4.1	Methods	54
5.4.2	Experimental data and setup	55
5.4.3	Classification	55
5.5	Neural networks approach for source classification	57
5.5.1	Data augmentation	58
5.5.2	Convolutional neural networks	58
5.5.3	Architecture optimization	59
5.5.4	Model training and evaluation	59
5.5.5	Experimental results	59
5.6	Summary	60
<b>6</b>	<b>Hankel-BTD Performance Evaluation on a Patient Database</b>	<b>63</b>
6.1	Introduction	63
6.2	Intra-patient variability: window position	64
6.2.1	Experimental data and setup	64
6.2.2	Experimental results	65
6.3	Intra-patient variability: window size	67
6.3.1	Experimental data and setup	67
6.3.2	Experimental results	68
6.4	Inter-patient variability	70
6.4.1	Experimental data and setup	70
6.4.2	Experimental results	71
6.5	Summary	73

---

<b>7 BTD Models for AF Analysis</b>	<b>77</b>
7.1 Introduction . . . . .	77
7.2 Löwner-based block term decomposition . . . . .	77
7.2.1 Model derivation . . . . .	78
7.2.2 Experimental data and setup . . . . .	79
7.2.3 Segments with short RR intervals . . . . .	80
7.2.4 Segments with disorganized and/or weak AA . . . . .	81
7.3 Coupled block term decomposition . . . . .	82
7.3.1 Model derivation . . . . .	83
7.3.2 Evaluation on synthetic data . . . . .	84
7.3.3 Evaluation on real data . . . . .	85
7.4 Summary . . . . .	87
<b>8 Improved Algorithms for BTD Computation</b>	<b>89</b>
8.1 Introduction . . . . .	89
8.2 Alternating group lasso and its constrained version . . . . .	89
8.2.1 Mathematical derivation . . . . .	89
8.2.2 Experimental evaluation of CAGL as an AA extraction tool . . . . .	91
8.3 CAGL as an AF complexity measurement tool . . . . .	97
8.3.1 Database and experimental setup . . . . .	98
8.3.2 Experimental Results . . . . .	99
8.4 Löwner-constrained alternating group lasso . . . . .	100
8.4.1 Mathematical derivation of LCAGL algorithm . . . . .	101
8.4.2 Synthetic AF data . . . . .	103
8.4.3 Real AF Database and Experimental Setup . . . . .	103
8.5 Summary . . . . .	108
<b>III Conclusions</b>	<b>111</b>
<b>9 Conclusions and Further Work</b>	<b>113</b>
9.1 Summary and conclusions . . . . .	113
9.2 Contributions . . . . .	114
9.2.1 Quantification of AA content and source classification . . . . .	114
9.2.2 Patient evaluation of Hankel-BTD performance . . . . .	114
9.2.3 BTD models for AF analysis . . . . .	114
9.2.4 Improved algorithms for BTD computation . . . . .	114
9.3 Discussion and limitations . . . . .	115
9.4 Further work . . . . .	116
<b>Bibliography</b>	<b>119</b>



# List of Figures

1.1	Block diagram summarizing the different contributions of the present doctoral thesis and their links.	7
2.1	Anatomy of the human heart <sup>1</sup> .	11
2.2	Electrical conduction system of the heart during a NSR <sup>2</sup> .	12
2.3	A typical ECG waveform during NSR for one cardiac cycle <sup>3</sup> .	13
2.4	The six bipolar leads: three limb leads and three augmented limb leads <sup>4</sup> .	15
2.5	The six precordial leads and the WCT <sup>5</sup> .	15
2.6	NSR <i>versus</i> AF <sup>6</sup> .	18
4.1	Matrix slices of a third-order tensor.	33
4.2	Mode-1 matrix unfolding of a third-order tensor.	33
4.3	Illustration of the PARAFAC or polyadic decomposition of a third-order tensor as a sum of $R$ rank-1 tensors.	35
4.4	Illustration of the Tucker-3 decomposition of a third-order tensor.	37
4.5	PARATUCK-2 decomposition of a third-order tensor.	38
4.6	Visual representation of the block term decomposition of an arbitrary third-order tensor.	39
4.7	Visual representation of coupled BTDs of arbitrary third-order tensors with common factor $\mathbf{c}_r$ , for $r = 1, 2, \dots, R$ .	41
5.1	Scatter plot showing the correlation between kurtosis and SC of the selected atrial source by the Hankel-based BTD, for an observed population of 20 AF patients. A positive correlation can be seen.	49
5.2	A single-beat segment of an AF ECG recording of one patient in lead II. The vertical line marks the location of the T-wave offset.	51
5.3	Potential atrial sources contribution to lead V1 estimated by PCA. Left: time domain (in mV). Right: frequency domain (in mV/ $\sqrt{\text{Hz}}$ ).	53
5.4	Potential atrial sources contribution to lead V1 estimated by RobustICA-f. Left: time domain (in mV). Right: frequency domain (in mV/ $\sqrt{\text{Hz}}$ ).	53
5.5	Potential atrial sources contribution to lead V1 estimated by Hankel-BTD for a single run. Left: time domain (in mV). Right: frequency domain (in mV/ $\sqrt{\text{Hz}}$ ).	54
5.6	Original ECG recording, AA source estimate and non-AA source estimates (VA and noises) on lead V1. The signals are vertically shifted for clarity.	56
5.7	AA source selection accuracy by different techniques. Left: SC proposed in [10]; PM1 and PM2 [24] (Sections 5.3.2 and 5.3.3). Right: NMSE-TQ; and the three classifiers: LDA, QDA and SVM.	57
5.8	Boxplot of the AUC and ACC metrics over CV.	60
5.9	CV confusion matrix.	61
6.1	The first 3 segments of the AF ECG recording composed of 56 segments. Although all the 12 leads are processed, only limb lead II is shown for clarity.	64
6.2	Distribution of SC values (%) for each version of Hankel-BTD, as well as PCA and RobustICA-f.	65

6.3	Variation of SC values (%) over the 56 segments for BTD-3, PCA and RobustICA-f. . . . .	66
6.4	Variation of DF (Hz) for each version of Hankel-BTD, as well as PCA and RobustICA-f. . . . .	67
6.5	Power contribution to lead V1 values ( $\text{mV}^2$ ) for the selected atrial source over the 56 segments for each version of Hankel-BTD, as well as PCA and RobustICA-f. . . . .	67
6.6	A 15-second segment of an AF ECG recording from the patient used for evaluate the time variability. For concision, only lead II is shown; all 12 leads are processed. . . . .	68
6.7	Atrial source contribution to lead V1 estimated by Hankel-BTD, RobustICA-f and PCA, for the 15-second segment, showed in the time domain (in mV). AA signal estimates are vertically shifted for clarity. The power contribution to lead V1 for each technique is also shown. . . . .	69
6.8	Atrial source contribution to lead V1 in the 15-second segment estimated by Hankel-BTD, RobustICA-f and PCA in the frequency domain (in $\text{mV}/\sqrt{\text{Hz}}$ ). . . . .	70
6.9	SC (%) of the AA signals estimated by Hankel-BTD from the observed AF ECG segments over ten independent runs. Runs that did not provided a sucessful AA extraction are not included. . . . .	71
6.10	Kurtosis of the AA signals estimated by Hankel-BTD from the observed AF ECG segments over ten independent runs. Runs that did not provided a sucessful AA extraction are not included. . . . .	72
6.11	A single heartbeat segment of an AF ECG recording, shown in lead II, from one patient of the observed population. A heartbeat consists in the QRST complex, followed by the TQ segment, where only AA is observed. . . . .	73
6.12	Potential atrial sources contribution to lead V1 estimated by Hankel-BTD for Patient 6. (a) In the time domain, measured in mV. (b) In the frequency domain, measured in $\text{mV}/\sqrt{\text{Hz}}$ . . . . .	75
6.13	Variation of SC (%) of the atrial source estimated by Hankel-BTD over 10 tensor factor initializations for the observed population of AF patients. Runs that did not provided a sucessful AA extraction are not shown. . . . .	75
6.14	Variation of DF (Hz) of the atrial source estimated by Hankel-BTD over independent runs for the observed population of AF patients. Runs that did not provided a sucessful AA extraction are not shown. . . . .	76
7.1	Top: A 1.5-second segment of an AF ECG recording with 4 QRS complexes from one patient (P2). The RR intervals are short and represented by the time difference between the peaks. Bottom: a single heartbeat segment of an AF ECG recording with a weak AA signal, from another observed patient (P6). Only bipolar limb lead II is shown for clarity, although the 8 independent leads (I, II, V1-V6) are processed in the experiments reported here. . . . .	80
7.2	Estimated atrial sources contribution to lead V1 in a segment of short RR intervals of Patient P4 by Hankel- and Löwner-BTDs, RobustICA-f and PCA in the time domain. AA signal estimates are vertically shifted for clarity with their respectives power contributions to lead V1. . . . .	82
7.3	Original recording, VA and AA estimates in lead II by the Löwner-BTD of Patient P7. The AA signal is vertically shifted for clarity. . . . .	83

7.4	Generated synthetic signal modeling an ECG with AF patterns plotted in time domain, where $t = m/F_s$ are the time values in seconds and $Y_{AF}(t)$ is the amplitude. . . . .	84
7.5	Top: the AF ECG recording of Patient 1 divided in three consecutive segments of different lengths. Bottom: the AF ECG recording of Patient 2 divided in two consecutive segments of same length. Only lead V1 is shown to ease visualization, although the 12 leads are processed in the experiments reported here. . . . .	86
7.6	Estimated atrial sources in lead V1 on time (top plot) and frequency domain (bottom plots) of Patient 2 by coupled BTD. . . . .	88
7.7	Number of iterations until convergence for both tensor-based methods. . . . .	88
8.1	Examples of generated semi-synthetic models: (a) AA sources generated as (1.1) with the parameters shown in Table 8.2; (b) overall semi-synthetic ECG signals in lead V1. . . . .	93
8.2	ECDF of rank chosen by CAGL for the AA source and of rank $L$ yielding the best AA extraction for BTD-NLS with different numbers of blocks $R$ . The curves are shown only up to $L = 30$ , for clarity. . . . .	94
8.3	Histogram of computed correlation coefficient $\rho$ (in absolute value) between ground-truth and estimated AA sources by both algorithms. . . . .	94
8.4	Results produced by CAGL with real ECGs: observed and estimated signals on lead V1. The estimated AA signals are vertically shifted by $-0.2$ mV for clarity. . . . .	96
8.5	Estimated AA sources produced by CAGL with ECG data from Patients 2 and 5. . . . .	98
8.6	Right: Boxplot showing the rank estimated by CAGL for all patients at different CA steps: initial (before ablation); intermediaries (CA between the first and penultimate steps); outcome (after the last CA step). Left: Boxplot at the beginning of CA and after PVI for the group of 17 patients who underwent this CA step. Notation (n) indicates the number of ECG segments considered in each box. . . . .	99
8.7	Scatter plot of the initial estimated rank (before CA) of the tensor block that provides the AA signal versus AF recurrence. A negative correlation can be observed. . . . .	100
8.8	Synthetic AF ECG models simulating the challenging cases where the AA signal is weak (Top) and the RR intervals are short (Bottom). The blue, red and yellow lines represent the VA, AA and noise interference, respectively. . . . .	104
8.9	Original and estimated VA signals in blue dashed and gray solid lines, respectively, along with the NMSE (dB) between them and the rank of its block, $\text{rank}_B$ . . . . .	105
8.10	Top lines: an example of a single heartbeat segment of an AF ECG recording with a weak AA signal (solid green) and its respective AA signal estimate (dashed red) by the Hankel-BTD method CAGL. Bottom lines: an example of an AF ECG recording used in these experiments with 3 QRS complexes (solid blue) and its respective AA signal estimate (dashed orange), also by CAGL. It can be seen that the Hankel-based method fails to perform the AA extraction. . . . .	106

8.11 Left: Original recording, VA and AA estimates in lead V1 by LCAGL of Patient P2 in time domain. Right: Power spectrum of AA estimate. The AA signal is vertically shifted for clarity. . . . .	107
8.12 SC values (%) of the AA source estimated by NLS and LCAGL for each patient of the observed database. Top: patients P1-P10 with segments presenting disorganized and/or weak AA signals. Bottom: patients P11-P20 whose segments are characterized by short RR intervals. . . . .	108
8.13 The power contribution to lead V1 in mV <sup>2</sup> of the AA source estimated by NLS and LCAGL for each patient of the observed database. Left: patients P1-P10 with segments presenting disorganized and/or weak AA signals. Right: patients P11-P20 whose segments are characterized by short RR intervals. . . . .	109
8.14 Original recording, VA and AA estimates in lead V1 of Patient P20 by LCAGL. The AA signal is vertically shifted for clarity. . . . .	109
8.15 Estimated atrial source contribution to lead V1 in a segment of short RR intervals of Patient P18 by CAGL and the Löwner-BTDs computed by the NLS method and LCAGL. AA signal estimates are vertically shifted for clarity. . . . .	110

# List of Tables

3.1	Summary of the matrix-based AA extraction techniques with their goals, advantages and limitations. . . . .	30
5.1	Overall physiological characteristics of the 10-patient population. . . . .	52
5.2	Overall physiological characteristics of the 30-patient population. . . . .	55
5.3	Confusion matrix of LDA, QDA and SVM. AcA: actual AA sources, AcN: actual non-AA sources, PrA: predicted AA sources and PrN: predicted non-AA sources. . . . .	57
5.4	Overall physiological characteristics of the 58-patient population. . . . .	58
5.5	Optimized parameters for the shallow CNN architecture. . . . .	60
6.1	Mean values of SC (%) and $K$ for the three versions of Hankel-BTD, as well as PCA and RobustICA-f. . . . .	66
6.2	Values of SC (%) for PCA and RobustICA-f. For Hankel-BTD, the maximum ( $BTD_{max}$ ) and the mean ( $BTD_{mean}$ ) values of SC (%) of ten independent runs are shown. . . . .	69
6.3	Overall physiological characteristics of the 20-patient population. . . . .	71
6.4	Values of SC (%) for PCA and RobustICA-f. For Hankel-BTD, the maximum ( $BTD_{max}$ ) and the mean ( $BTD_{mean}$ ) values of SC (%) of ten independent runs are shown. . . . .	74
7.1	Overall physiological characteristics of the 10-patient population. . . . .	79
7.2	SC values (%) of the AA and the number of iterations (mean $\pm$ standard deviation) of the NLS method for the Löwner-BTD (BTD-L) and the Hankel-BTD (BTD-H) in ten Monte Carlo runs. . . . .	81
7.3	NMSE (dB) between the estimated and original AA sources for the coupled BTD and BTD. . . . .	85
7.4	Values of SC (%), $\kappa$ , and $P(r)$ in mV <sup>2</sup> of the AA signal estimated by coupled BTD and BTD, for all the processed segments of both patients. The best solution out of ten Monte Carlo runs is chosen. . . . .	87
8.1	Pseudocode for CAGL algorithm [20]. . . . .	91
8.2	Parameters of the synthetic AA signal model of (1.1). . . . .	92
8.3	Block ranks of the ECG sources extracted by CAGL and characteristics of the potential AA sources. . . . .	95
8.4	Overall physiological characteristics of the 20-patient population . . . . .	98
8.5	Parameters of the synthetic AA signal models . . . . .	103
8.6	Overall physiological characteristics of the 20-patient population used in the experiments with LCAGL. . . . .	104



# Part I

## Introduction



## CHAPTER 1

# Thesis Overview

---

## Contents

---

<b>1.1</b>	<b>Context and motivation</b>	<b>3</b>
<b>1.2</b>	<b>Objectives</b>	<b>4</b>
1.2.1	General objectives	4
1.2.2	Specific objectives	4
<b>1.3</b>	<b>Database and preprocessing</b>	<b>4</b>
<b>1.4</b>	<b>Thesis structure and contributions</b>	<b>5</b>
<b>1.5</b>	<b>Scientific production</b>	<b>7</b>
1.5.1	Journals	7
1.5.2	Conferences	8

---

## 1.1 Context and motivation

Atrial Fibrillation (AF) is the most frequent sustained arrhythmia encountered in clinical practice, responsible for an increasingly high number of hospitalizations and deaths [51], [78], [59]. This challenging cardiac condition is known as the last great frontier in cardiac electrophysiology, as the electrophysiological mechanisms responsible for its triggering and maintenance are not completely understood [60]. A non-invasive and cost-effective way to study this cardiac rhythm disorder is analyzing the atrial activity (AA) signal from the electrocardiogram (ECG). However, the AA during AF is characterized by low-amplitude fibrillatory waves, called f-waves, that are masked by the QRS complex, responsible for the ventricular activity (VA), in each heartbeat and sometimes present an amplitude lower than the noise, making difficult its analysis [74].

Over the years, signal processing techniques have helped cardiologists to better understand AF by extracting and analyzing the AA from the ECG. Pioneering techniques focused on subtracting an average beat from each QRS complex of the ECG [96], [101]. Such techniques require long duration recordings and assume that an average beat can well model each QRS complex [2], which actually presents some variations due to respiratory and muscular activity. An alternative approach takes advantage of the fact that AA and VA during AF are decoupled and uses matrix-based blind source separation (BSS) methods to perform the AA extraction [66], [88]. Matrix factorization techniques requires imposing some constraints and assumptions about the sources in order to guarantee uniqueness. Such constraints may be mathematically coherent, but they are not always physiologically satisfied and may lack physiological grounds, making difficult results interpretation.

On the other hand, tensor decompositions present some remarkable features, such as uniqueness up to mild conditions. In particular, the block term decomposition (BTD) [64], which was recently proposed as a tensor-based BSS method [65], can be unique

by imposing some constraints over its matrix factors that are both mathematically and physiologically easy to satisfy. Also, cardiac sources can be well modeled by particular mathematical functions that, when mapped into structured matrix factors, lead quite naturally to this tensor decomposition, pointing to its suitability for AF ECG analysis. To date, this decomposition has not yet been fully explored in the BSS approach for AA analysis during AF, opening some challenging questions about the feasibility and performance of tensor factorization approaches in this increasingly active research field of biomedical engineering.

## 1.2 Objectives

The present doctoral thesis takes a step from the matrix-based BSS formulation, aiming to investigate and explore the feasibility and efficiency of the tensor-based formulation in this challenging biomedical scenario. Such approach is motivated by the remarkable features presented by tensor decompositions and its connection with mathematical models that can well approximate physiological signals in AF ECGs.

### 1.2.1 General objectives

The first goal of the present thesis is to validate and investigate the performance of the Hankel-BTD in varying-length segments in a population of patients suffering from persistent AF, as well as analyze the source signals after performing BSS. Such investigation leads to the definition of new indices to measure AA estimation quality and complexity, novel approaches to classify cardiac sources, and the use of new tensor-based techniques for challenging persistent AF scenarios. The latter results in an improved optimization strategy that ensures the structure of the employed tensor decomposition, proving to be essential to the improvement of BSS performance.

### 1.2.2 Specific objectives

More detailed, the specific objectives of the present doctoral thesis are the following:

- Investigate and validate the feasibility and performance of the Hankel-BTD as an AA extraction tool for AF analysis.
- Propose new indices to measure AA estimation quality and complexity in AF ECGs.
- Propose and validate new tensor models to perform AA extraction in challenging scenarios of persistent AF ECGs.
- Assess classification algorithms to accurately select the AA source among the other source estimates after performing BSS.
- Propose and implement a novel optimal strategy to ensure the structure of the Löwner-BTD matrix factor.

## 1.3 Database and preprocessing

The experiments reported in this doctoral thesis consider segments of synthetic models and real standard 12-lead AF ECG recordings from different patients suffering from persistent AF.

The real AF ECG recordings belong to the PERSIST database provided by the Cardiology Department of the Princess Grace Hospital Center, Monaco. All the recordings are acquired at a 977 Hz sampling rate and are preprocessed by a zero-phase forward-backward type-II Chebyshev bandpass filter with cutoff frequencies of 0.5 and 40 Hz, in order to suppress high-frequency noise and baseline wandering. A detailed description of the real AF ECG database used in the experiments is given at each chapter of the Part II of the present doctoral thesis. Experiments consider a population of up to 58 persistent AF patients.

When not stated otherwise, the synthetic signals are generated as follows. To simulate the AA signal during AF, the model proposed in [101] that mimics the f waves is used. This model is given by:

$$S_{AA}(m) = -\sum_{p=1}^P a_p(m) \sin(p\theta(m)) \quad (1.1)$$

with modulated amplitude and phase respectively given by:

$$a_p(m) = \frac{2}{p\pi} \left[ a + \Delta a \sin\left(2\pi \frac{f_a}{F_s} m\right) \right]$$

and

$$\theta(m) = 2\pi \frac{f_0}{F_s} m + \left(\frac{\Delta f}{F_f}\right) \sin\left(2\pi \frac{F_f}{F_s} m\right)$$

where  $a$  is the sawtooth amplitude,  $\Delta a$  the modulation peak amplitude,  $f_a$  the amplitude modulation frequency,  $F_s$  the sampling frequency,  $f_0$  the frequency value around which  $\theta(m)$  varies sinusoidally,  $\Delta f$  the maximum frequency deviation and  $F_f$  the modulation frequency.

In order to simulate the VA signal, a synthetic T-wave modeled by a cosinus function as in [31] and three synthetic QRS complexes modeled by rational functions were generated according to the model function proposed in [4] and added together. This model is given by:

$$S_{VA}(m) = \Re(e^{-i\Theta} r_a^n(e^{im})) \quad (1.2)$$

where  $\Theta$  is the coefficient parameter and  $r_a^n(\cdot)$  is a basic normalized rational function given by:

$$r_a^n(z) := \left[ \frac{1 - |a|}{1 - \bar{a}z} \right]^n \quad (1.3)$$

where  $\bar{a}$  is the reciprocal of the pole  $a$  and  $n$  is a multiplicity order. The three synthetic models are given by varying different values of  $\Theta \in \{\frac{\pi}{2}, \frac{\pi}{4}, 0\}$ .

Finally, the noise signal that simulates the interference present in ECGs is represented by an additive white Gaussian noise (AWGN) with zero-mean and variance  $\sigma^2$ . The mixing matrix is also generated according to a Gaussian distribution, with scaling factors chosen to obtain an average power ratio between the signals consistent with clinical ECGs.

In addition, alternative models to generate synthesized AF recordings can be found in the literature [91], [104], [83].

## 1.4 Thesis structure and contributions

The remaining of the present doctoral thesis consists in 8 chapters (Chapters 2 – 9) grouped in 3 parts. Part I includes the present chapter and other 3 chapters (Chapters 2 – 4) and presents a theoretical background necessary for the comprehension of this thesis, as well as the fundamental state-of-the-art that supports and motivates the contributions

reported later. Part II consists in 4 chapters (Chapters 5 – 8) and presents the original contributions of the present doctoral thesis. Finally, Part III concludes this work and consists in a single chapter, that is, Chapter 9. More specifically:

- **Chapter 2** presents the basic concepts of cardiology, starting from the anatomy of the human heart and its conduction system. Then, a particular attention is given to the ECG, a well-known non-invasive tool whose interpretation and pre-processing are fundamental to detect arrhythmias, generally described in this chapter. The last section of this chapter is entirely devoted to AF. First some statistics on AF are presented, followed by theories and current knowledge of the electrophysiological mechanisms underlying this challenging arrhythmia. The section continues presenting some classification schemes of AF and finishes by describing its main therapies.
- **Chapter 3** describes the main literature behind the problem of noninvasive AA extraction for AF analysis. First, the classical methods that focus on VA cancellation are presented, then the matrix- and tensor-based BSS approaches finish the chapter.
- **Chapter 4** enters in the mathematical background part of the present doctoral thesis, introducing the fundamental concepts of multilinear algebra, with particular attention to the main tensor decompositions, including those used in the experiments reported in the following chapters, i.e., BTD and coupled BTD.
- **Chapter 5** is the first chapter of the contributions part, focusing on the proposed indices to measure the AA estimation quality of a source. Different approaches for AA source detection are also explored in this chapter.
- **Chapter 6** focuses on the investigation of the feasibility and reproducibility of Hankel-BTD as an AA extraction tool. Experiments over a population of patients suffering from persistent AF and a whole AF ECG recording are reported in this chapter.
- **Chapter 7** proposes alternative tensor-based approaches to perform AA extraction for AF analysis. First, the Löwner-BTD is introduced as a tool to estimate the VA that, when subtracted from the original ECG, ideally results in the AA signal. Then, the coupled Hankel-BTD is introduced as a more cost-effective AA extraction tool than its non-coupled counterpart.
- **Chapter 8** starts by presenting a recently proposed algorithm, called alternating group lasso (AGL), to compute the BTD that presents interesting advantages over the existing ones. Then, its Hankel-constrained version is assessed as an AA extraction tool over a few patients suffering from persistent AF. The chapter finishes with a proposal of an optimal strategy, yielding the Löwner-constrained version of AGL, to compute the Löwner-BTD approach presented in Chapter 7. The Löwner-constrained AGL is also validated as an AA extraction tool at the end of this chapter.
- **Chapter 9** concludes the manuscript by summarizing the study that has been conducted and discussing the experimental results that validate the presented contributions. Then, the present doctoral thesis is ended by focusing on potential new perspectives of tensor-based AA extraction for persistent AF analysis.

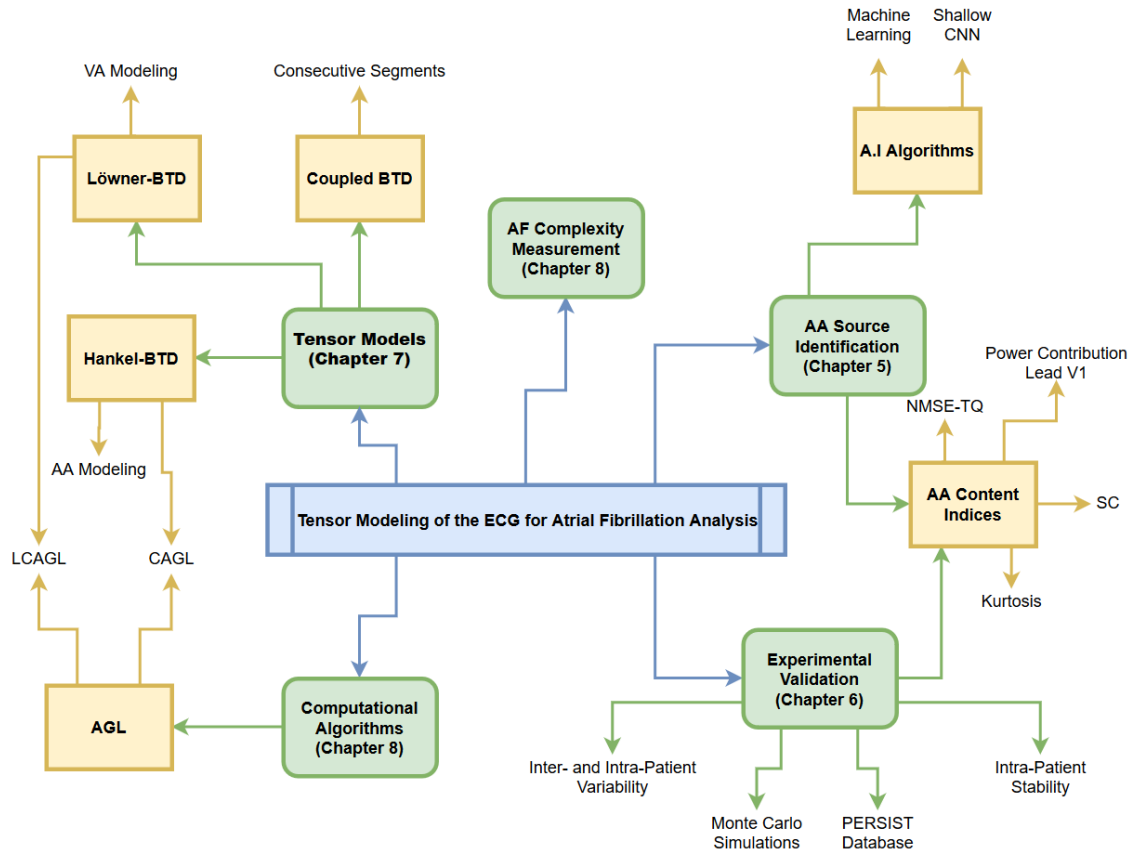


Figure 1.1: Block diagram summarizing the different contributions of the present doctoral thesis and their links.

To facilitate the comprehension of the different contributions and their links presented in this doctoral thesis, a block diagram is shown in Figure 1.1.

## 1.5 Scientific production

The results of the present doctoral thesis have yielded several publications in high quality international journals and conferences.

### 1.5.1 Journals

1. J. H. de M. Goulart, P. M. R. de Oliveira, R. C. Farias, V. Zarzoso, and P. Comon, “Alternating group lasso for block-term tensor decomposition and application to ECG source separation”, *IEEE Transactions on Signal Processing*, vol. 68, pp. 2682-2696, 2020.
2. P. M. R. de Oliveira and V. Zarzoso, “Block term decomposition of ECG recordings for atrial fibrillation analysis: temporal and inter-patient variability”, *Journal of Communication and Information Systems*, vol. 34, no. 1, pp. 111-119, Apr. 2019.
3. P. M. R. de Oliveira, J. H. de M. Goulart, C. A. R. Fernandes and V. Zarzoso, “Persistent atrial fibrillation analysis using a tensor decomposition with Löwner constraints”, submitted, 2020.

### 1.5.2 Conferences

4. P. M. R. de Oliveira, V. Zarzoso and C. A. R. Fernandes, “Coupled tensor model of atrial fibrillation ECG”, to appear in Proc. *EUSIPCO-2020, 28th European Signal Processing Conference*, Amsterdam, Netherlands, Jan. 18-22, 2021.
5. L. de S. Abdalah, P. M. R. de Oliveira, V. Zarzoso and W. Freitas Jr, “Tensor-based noninvasive atrial fibrillation complexity index for catheter ablation”, to appear in Proc. *CinC-2020, Computing in Cardiology 2020*, Rimini, Italy, Sep. 13-16, 2020.
6. I. N. Lira, P. M. R. de Oliveira, W. Freitas Jr and V. Zarzoso, “Automated atrial fibrillation source detection using shallow convolutional neural networks”, to appear in Proc. *CinC-2020, Computing in Cardiology 2020*, Rimini, Italy, Sep. 13-16, 2020.
7. P. M. R. de Oliveira, V. Zarzoso and C. A. R. Fernandes, “Source classification in atrial fibrillation using a machine learning approach”, in *Proc. CinC-2019, Computing in Cardiology 2019*, Biopolis, Singapore, Sep. 8-11, pp. 1-4, 2019.
8. P. M. R. de Oliveira and V. Zarzoso, “Löwner-based tensor decomposition for blind source separation in atrial fibrillation ECGs”, in *Proc. EUSIPCO-2019, 27th European Signal Processing Conference*, A Coruña, Spain, Sep. 2-6, pp. 1-5, 2019.
9. P. M. R. de Oliveira and V. Zarzoso, “Temporal stability of block term decomposition in noninvasive atrial fibrillation analysis”, in *Proc. Asilomar-2018, 52nd Annual Asilomar Conference on Signals, Systems, and Computers*, Pacific Grove, U.S.A, Oct. 28-31, pp. 816-820, 2018.
10. P. M. R. de Oliveira and V. Zarzoso, “Block term decomposition analysis in long segments of atrial fibrillation ECGs”, in *Proc. SBRT-2018, XXXVI Simpósio Brasileiro de Telecomunicações e Processamento de Sinais*, Campina Grande, Brazil, Sep. 16-19, pp. 578-582, 2018.
11. P. M. R. de Oliveira and V. Zarzoso, “Source analysis and selection using block term decomposition in atrial fibrillation”, in *Proc. LVA/ICA-2018, 14th International Conference on Latent Variable Analysis and Signal Separation*, Guildford, United Kingdom, Jul. 2-6, pp. 46-56, 2018.

## CHAPTER 2

# Fundamentals of Cardiology

---

## Contents

---

<b>2.1</b>	<b>Introduction</b>	<b>9</b>
<b>2.2</b>	<b>The human heart</b>	<b>9</b>
<b>2.3</b>	<b>Cardiac conduction system</b>	<b>10</b>
<b>2.4</b>	<b>Principles of electrocardiography</b>	<b>11</b>
<b>2.5</b>	<b>The 12-lead electrocardiogram system</b>	<b>14</b>
2.5.1	Limb leads	14
2.5.2	Augmented limb leads	14
2.5.3	Precordial leads	15
2.5.4	Interpretation and preprocessing	16
<b>2.6</b>	<b>Arrhythmias</b>	<b>16</b>
<b>2.7</b>	<b>Atrial fibrillation</b>	<b>17</b>
2.7.1	Statistics	17
2.7.2	Mechanisms	17
2.7.3	Classification	19
2.7.4	Treatments	20
<b>2.8</b>	<b>Summary</b>	<b>21</b>

---

## 2.1 Introduction

The present chapter first aims at providing a general description of the human heart anatomy, the cardiac conduction system, the basic concepts of the ECG and its 12-lead configuration. The main objective of this first part of the chapter is to provide the reader the fundamental knowledge of the heart activity and the electrophysiological mechanisms behind it. Particular attention is given to the mechanisms of the ECG and its 12-lead configuration, a well-known tool used to record heart's electrical activity and essential for a rapid diagnosis of arrhythmias. The second part of this chapter is entirely devoted to AF, showing some statistics and the current knowledge of the mechanisms, classification and treatments of this challenging cardiac condition. The goal of this second part is to show the reader the worrisome scenario of AF and provide the electrophysiological knowledge necessary to understand the connections between AF and the signal processing techniques presented later in this thesis.

## 2.2 The human heart

Located within the thoracic cavity, between the two lungs and above the diaphragm, the heart is one of the most important organs in the human body. Its function is to

pump oxygenated blood from the lungs to all the tissues of the body and pump back deoxygenated blood from all the body tissues to the lungs, for oxygenation. The heart is covered by a thick fibroelastic sac called pericardium, which is composed of three layers: epicardium (the outer membrane), myocardium (the middle cardiac muscle), and endocardium (the thin inner layer).

The internal anatomy of the heart is illustrated in Figure 2.1 and consists in four chambers made entirely of myocardium. The two upper chambers are named atria, whereas the two lower chambers are called ventricles. The right side of the heart is responsible to pump blood from the body to the lungs and it is separated by a wall of tissue called septum from the left side, whose function is to pump blood from the lungs throughout the body [106]. More specifically, the circulatory circuit consists in the following steps:

1. The right atrium (RA) receives deoxygenated blood from the body via the superior vena cava and inferior vena cava, sending it right after to the right ventricle (RV) through the tricuspid valve.
2. The RV then sends the blood to the lungs for oxygenation via the pulmonary artery, passing through the pulmonary valve. After, the blood now rich in oxygen is sent to the left atrium (LA) through the four pulmonary veins and then from the LA to the left ventricle (LV) via the mitral valve.
3. Passing through the aortic valve, the blood is now pumped from the LV into the aorta artery, which is the largest and most important artery in the human body. The aorta then sends the oxygenated blood to all the body tissues.
4. The deoxygenated blood returns from the body to the heart entering in the RA and the cycle starts again.

The first two steps compose the pulmonary circuit, whereas the last two steps consist in the systemic circuit. Together, the pulmonary and systemic circuits establish the circulatory circuit, allowed by the relaxation and contraction of the four chambers of the heart. The phase of the circulatory circuit when the heart muscles relaxes is called diastole and the phase when occurs the contraction is called systole. The bloodflow in the heart cycle is illustrated by white arrows in Figure 2.1, where the right side of the heart is in purple color, representing the deoxygenated blood, and the left side is in light red color, representing the oxygenated blood.

## 2.3 Cardiac conduction system

The cardiac conduction system is an electrophysiological system where the myocardium performs its contraction independently, that is, without the necessity of any external incitement. Briefly, this contraction is initiated by an electrical impulse and propagates through the atria and ventricles [55].

During the normal sinus rhythm (NSR), i.e., the normal activation of the heart, an electrical impulse is generated from the sinoatrial (SA) node, located in the RA. This impulse propagates uniformly throughout the atria (causing its contraction) via internodal pathways, until it reaches the atrioventricular (AV) node. Before conducting the impulse to the bundle of His, the AV node delays it by a fraction of seconds. This

---

<sup>1</sup>[https://commons.wikimedia.org/wiki/File:Diagram\\_of\\_the\\_human\\_heart\\_\(cropped\).svg](https://commons.wikimedia.org/wiki/File:Diagram_of_the_human_heart_(cropped).svg)

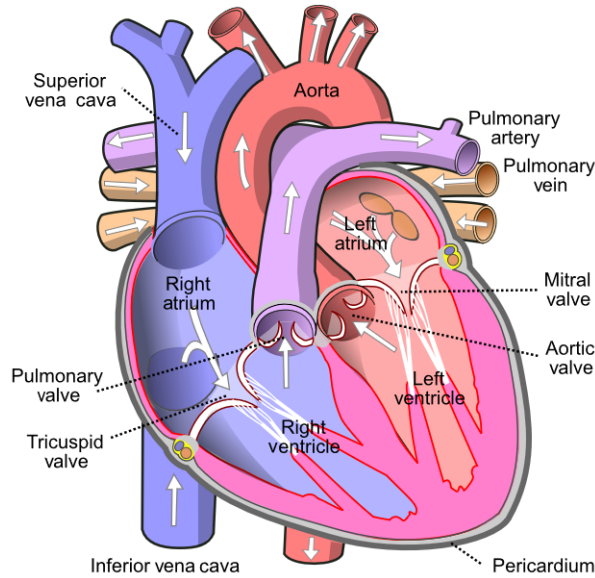


Figure 2.1: Anatomy of the human heart<sup>1</sup>.

delay is vital to guarantee the atrial-ventricular synchrony. Finally, the electrical impulse travels through the bundle of His, which is divided in two branches (right bundle branch and left bundle branch), ending in the Purkinje fibers, located in the inner ventricular chambers. The Purkinje fibers are responsible for the ventricular contraction, being essential to ensure a regular and synchronized heart rhythm. The His-Purkinje system is in charge of rapidly conducting the electric impulse in the ventricles. It coordinates the contraction of the ventricles in order to ensure that sufficiently blood is pumped.

An abnormal cardiac conduction system can be the cause of cardiac diseases, as for example, arrhythmias, affecting millions of people worldwide as will be discussed later in the chapter. The normal cardiac electrical conduction system is illustrated in Figure 2.2, where the conduction pathway of the cardiac impulse is highlighted in green color.

## 2.4 Principles of electrocardiography

Recalling from the previous section that, during the circulatory circuit, the heart performs contraction and relaxation, induced by an electrical impulse that propagates through the heart chambers. In this process, one part of the myocardium is depolarized and another part polarized, resulting in an electric dipole, i.e., a charge separation system. This electric dipole is responsible for the generation of an electric field throughout the body, whose voltage can be detected by using electrodes on the body surface, providing then the electrocardiogram (ECG) [33].

The ECG is a voltage versus time graph of the heart's electrical activity. The process of producing an ECG is called electrocardiography and the machine that produces the ECG is called electrocardiograph. In 1842, Carlo Matteucci reported for the first time an electrical current in the heart. Willem Einthoven discovered the mechanisms of the ECG in 1885 and, along with Étienne-Jules Marey, invented the first practical electrocardiograph in 1903. Later in 1924, Willem Einthoven was awarded with the Nobel Prize in Physiology or Medicine for his contributions. The cardiac signals are detected by elec-

<sup>2</sup><https://www.medicalxamprep.co.uk/wp-content/uploads/2016/02/Cardiac-Conduction-System.jpeg>

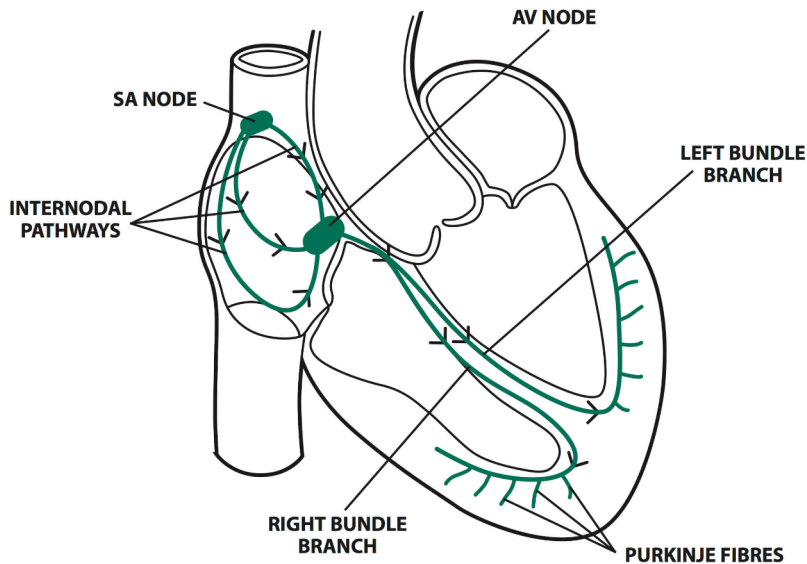


Figure 2.2: Electrical conduction system of the heart during a NSR<sup>2</sup>.

trodes placed on the body surface, amplified, and recorded by the electrocardiograph, generally in mV per second. The instantaneous difference of voltage measured between each pair of electrodes is called lead. Conventionally, 10 electrodes are placed on the body surface in order to generate 12 leads, producing then the well-known standard 12-lead ECG.

ECGs are a noninvasive, cheap and efficient tools in clinical practice for detecting several cardiac problems by analyzing abnormalities in the ECG waveform or duration of wave intervals [76]. Indeed, cardiac diseases like myocardial infarction, coronary artery disease, arrhythmias, etc., can be efficiently detected by ECGs, which are also frequently used to monitor surgeries and interventions like catheter ablation.

During a normal circulatory circuit, the ECG waveform of a cardiac cycle is illustrated in Figure 2.3, where it can be observed the following characteristic waves, segments and intervals:

- **P wave:** represents the depolarization, i.e., activation, of the atria and has around 80-100 ms of duration. With an amplitude typically smaller than 0.25 mV, this wave is the first deflection on the ECG recording.
- **QRS complex:** it is composed of 3 waves (Q, R, and S waves) that, together, represents the ventricular depolarization. It has around 60-120 ms of duration and its shape varies depending on the lead where it is recorded. In parallel with the ventricular depolarization, the atria are performing the repolarization. However, its effect is usually not detected in the ECG, due to the much larger amount of myocardium that is involved in the generation of the QRS complex [33].
- **T wave:** it is the last wave recorded in the ECG of one heart cycle and it represents the repolarization of the ventricles. Normally, the T wave has a duration of 100-250 ms and always succeeds the QRS complex and precedes the P wave of the next cardiac cycle.

<sup>3</sup><https://commons.wikimedia.org/wiki/File:SinusRhythmLabels.svg>

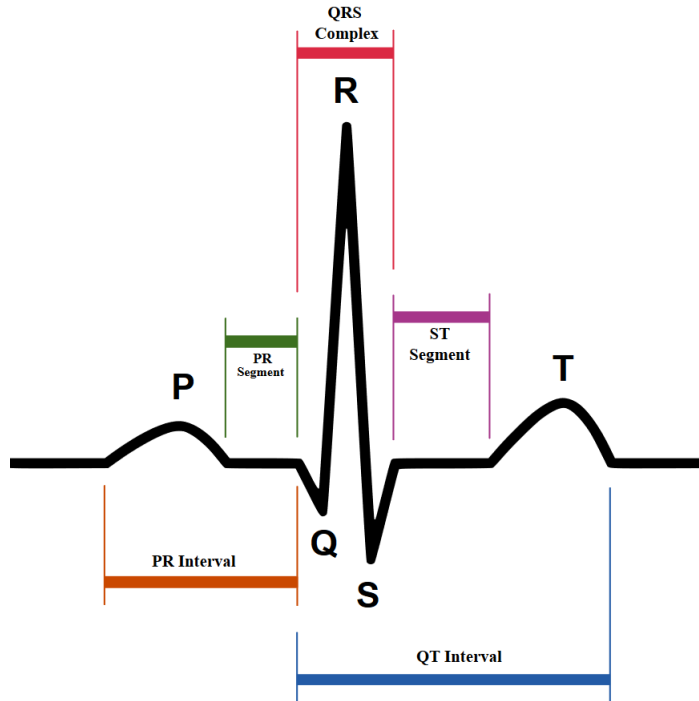


Figure 2.3: A typical ECG waveform during NSR for one cardiac cycle<sup>3</sup>.

- **PR segment:** it is the time segment measured from the end of the P wave to the beginning of the QRS complex. This segment represents the time delay between atrial and ventricular depolarization, which is around 60 ms.
- **ST segment:** measured from the end of the QRS complex to the beginning of the T wave, the ST segment can have a duration ranging from 5 to 150 ms. It represents the time period in which the ventricles are completely depolarized, performing contraction.
- **PR interval:** from the beginning of the P wave to the beginning of the QRS complex, this intervals reflects the propagation time of the electrical impulse from the SA node to the Purkinje fibers. A normal PR interval has between 120 to 200 ms of duration.
- **QT interval:** it is the time interval from the moment when the ventricles start depolarizing to the moment when they are completely depolarized. This interval is typically 400 ms long and it is measured from the beginning of the QRS complex until the end of the T wave.

Another interval that is not shown in Figure 2.3 but is important to describe is the RR interval, measured by the distance between the R waves of two consecutive cardiac cycles. RR intervals are usually 600-1200 ms long and are crucial to determine the heart rate (HR) and heart rate variability (HRV). The TQ segment also deserves some attention. It measures the time distance between the end of the T wave to the beginning of the QRS complex and it is about 400 ms long. As will be presented later, the AA is visible and free from VA in the TQ segments during AF episodes. It is also important to highlight that segments are used to analyze variations in the isoelectric line of the ECG, different from intervals, which are used to analyze their duration.

## 2.5 The 12-lead electrocardiogram system

Commonly, the ECG is measured by placing 10 electrodes on the body surface, generating 12 leads, each measuring a specific electrical potential. The standard 12-lead ECG is subdivided in three limb leads, three augmented limb leads, and six precordial leads. The limb leads are bipolar, i.e., they measure the electrical potential difference between two electrodes, whereas the augmented limb leads and precordial leads are unipolar, i.e., they record the absolute electrical potential at one electrode, relative to a reference potential.

### 2.5.1 Limb leads

Forming the Einthoven's triangle, bipolar leads I, II and III are denoted limb leads. Each limb lead measures the electrical potential difference between two electrodes out of the three electrodes, placed in both arms and the left leg. More precisely:

- Lead I measures the electrical potential difference between the electrode placed on the left arm ( $\Phi_{LA}$ ) and the one placed on the right arm ( $\Phi_{RA}$ ):

$$I = \Phi_{LA} - \Phi_{RA} .$$

- Lead II measures the electrical potential difference between the electrode placed on the left leg ( $\Phi_{LL}$ ) and the one placed on the right arm ( $\Phi_{RA}$ ):

$$II = \Phi_{LL} - \Phi_{RA} .$$

- Lead III measures the electrical potential difference between the electrode placed on the left leg ( $\Phi_{LL}$ ) and the one placed on the left arm ( $\Phi_{LA}$ ):

$$III = \Phi_{LL} - \Phi_{LA} .$$

Bipolar limb leads I, II and III are illustrated in Figure 2.4 and are linearly dependent between them, as according to Kirchhoff's law, each one of them can be expressed as a linear combination of the other two. Indeed, one can note that  $I = II - III$ ,  $II = I + III$  and  $III = II - I$ .

### 2.5.2 Augmented limb leads

Also referred as Goldberger's leads, the three augmented limb leads measure the electrical potential between one limb electrode and a theoretical reference potential called Wilson Central Terminal (WCT), which is considered to be zero in ideal circumstances. The WCT can be seen in Figure 2.5 and is created as a combination of two limb electrodes, forming the negative end. Then, the positive end of the augmented limb lead is created by the limb electrode that is referenced against the WCT. For this reason, the augmented limb leads are unipolar and are expressed as:

$$\begin{aligned} aVF &= \Phi_{LL} - \frac{1}{2}(\Phi_{RA} + \Phi_{LA}) = II - \frac{1}{2}I \\ aVL &= \Phi_{LA} - \frac{1}{2}(\Phi_{RA} + \Phi_{LL}) = I - \frac{1}{2}II \\ aVR &= \Phi_{RA} - \frac{1}{2}(\Phi_{LA} + \Phi_{LL}) = -\frac{I + II}{2} . \end{aligned}$$

---

<sup>4</sup>[https://commons.wikimedia.org/wiki/File:Limb\\_leads\\_of\\_EKG.png](https://commons.wikimedia.org/wiki/File:Limb_leads_of_EKG.png#/media/File:Limb_leads_of_EKG.png)

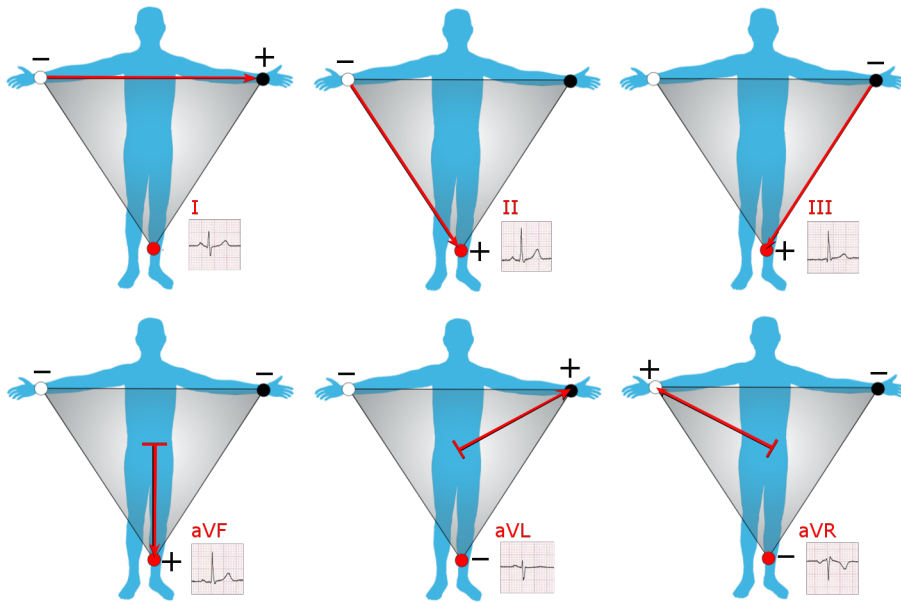


Figure 2.4: The six bipolar leads: three limb leads and three augmented limb leads<sup>4</sup>.

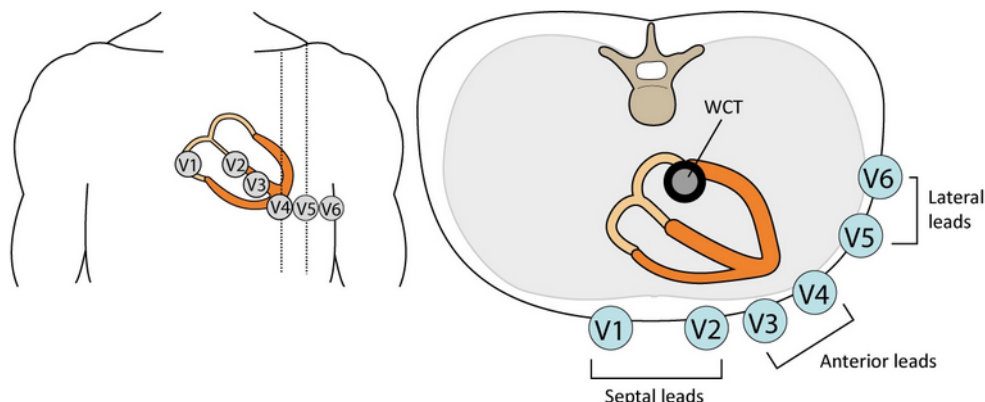


Figure 2.5: The six precordial leads and the WCT<sup>5</sup>.

One can see that the electrical potential difference between the left leg and the WCT generated by a combination of the electrical potential in the right and left arms produces the lead aVF. Augmented leads aVL and aVR are produced analogously. Together with the bipolar limb leads, the unipolar augmented limb leads record the cardiac electrical activity forming a frontal plane, relative to the heart.

### 2.5.3 Precordial leads

Providing a different view of the cardiac electrical activity, the six unipolar precordial leads (or chest leads) record the voltage between positive electrodes placed in specific regions around the rib cage and the WCT. Leads V1 and V2 are called septal leads, leads V3 and V4 are denoted anterior leads, while leads V5 and V6 are referred as lateral (or anterolateral) leads. Their specific placement over the chest is illustrated in Figure 2.5. Together, the six precordial leads (V1-V6) form a transverse plane, which is orthogonal to the frontal plane, and are linearly independent, i.e., they cannot be mathematically derived from the other leads.

### 2.5.4 Interpretation and preprocessing

In the standard 12-lead ECG there are only 8 independent leads. However, it is important to record the other redundant leads, as they provide information in different planes and angles, enhancing pattern recognition [76]. The 12-lead ECG is considered one of the most important tools for diagnosing cardiovascular diseases and is commonly used in clinical practice. Indeed, ECG waveform interpretation have a diagnostic significance. For example, determination of the PR intervals provides information about the conduction through the AV node, elevation of the ST segment normally indicates ventricular ischemia [33], variations in the RR interval are solid indicators of arrhythmias, common cardiac diseases that will be detailed later in this chapter.

The ECG interpretation can be hindered by interference, noise and artifacts that may change its isoelectric waveform, also modifying important information about the cardiac electrical activity. For this reason, a proper preprocessing of the ECG signal is crucial to suppress such interfering components, giving then a clear electrophysiological signal and easing its interpretation. Interference can be technical or physiological. Understanding their origin is an important task before choosing and applying the preprocessing methods that suits the objectives of ECG interpretation.

## 2.6 Arrhythmias

Arrhythmias, also called cardiac arrhythmias, are heart diseases characterized by abnormal ECG waveforms where the heartbeat is irregular, beating too fast (tachycardia) or too slow (bradycardia). There are two groups of heart rhythm conditions:

- **Ventricular arrhythmias:** affecting the ventricles, this group of arrhythmias makes the heart beat too fast, preventing the oxygenated blood from circulating to the body tissues. Examples of ventricular arrhythmias are:
  - **Ventricular fibrillation:** characterized by a very rapid and irregular electrical activation of the ventricles, leading to sudden cardiac death if not treated rapidly. Several deaths per year are caused by this type of arrhythmia, which requires medical attention as soon as it is detected.
  - **Premature ventricular contractions:** as the name tells, this rhythm disorder occurs when the ventricles contract too soon. Typically this arrhythmia is not serious and does not require treatment, unless the patient already has some heart disease or history.
- **Supraventricular arrhythmias:** occur in the area above the ventricles, usually the atria, and are also known as atrial arrhythmias. They can cause shortness of breath and a fast pulse. Some examples are:
  - **Supraventricular tachycardia:** happens when the electrical signals from the atria fire abnormally, making the heart rate very rapid.
  - **Atrial flutter:** is a common abnormal arrhythmia whose activation starts in the atria, producing a fast heart rate. It is characterized by waves with a saw-tooth pattern on the ECG.
  - **Atrial fibrillation (AF):** abnormal generation and conduction of electrical impulses throughout the atria, causing impaired atrial contraction. This type

---

<sup>5</sup><https://ecgwaves.com/topic/ekg-ecg-leads-electrodes-systems-limb-chest-precordial/>

of arrhythmia is the focus of the present doctoral thesis, and for this reason it will be detailed later in the remaining of this chapter.

## 2.7 Atrial fibrillation

### 2.7.1 Statistics

Especially affecting the elderly, AF is the most common sustained cardiac arrhythmia encountered in clinical practice, considered as the last great frontier of cardiac electrophysiology [110]. Decreasing life quality and increasing healthcare costs, this supraventricular tachyarrhythmia is characterized by an uncoordinated, chaotic and irregular atrial activation. This challenging cardiac condition represents an important economical burden, as a patient with AF costs, annually, approximately \$8 700 more to the healthcare system than a patient without AF. Indeed, the treatment of AF is estimated to add \$26 billion per year to the USA healthcare costs [51]. Also a major health and social concern, AF has about 467 000 hospitalizations as the primary diagnosis every year in USA, and the number of deaths are estimated to be more than 99 000 [51]. In 2010, it was estimated that the number of patients suffering from AF worldwide is around 33.5 million [78] and, about 160 000 new patients are diagnosed with AF every year only in USA, with similar numbers reported in European countries. By 2050, if the number of hospitalizations per year stays stable, AF prevalence is expected to increase from 2.3 to about 12.1 – 15.9 million patients only in USA, becoming then a new epidemic [74].

With its electrophysiological mechanisms still not completely understood, the number of patients suffering from AF is increasing each year worldwide. Considering this worrisome scenario, the intensive clinical research of this challenging cardiac rhythm disturbance has increased in the past decades and is expected to increase further in the following years.

### 2.7.2 Mechanisms

Earlier in this chapter, it was described that in a NSR an electrical impulse is generated in the SA node and travels towards the LA and the ventricles. This normal activation makes the atria beat in a regular and synchronized way with the ventricles. During AF episodes, electrical impulses are generated elsewhere in the atria, typically around the pulmonary veins. These abnormal impulses propagate in a chaotic and irregular way across the atria, making it beat in a irregular and unsynchronized way with the ventricles.

In an AF ECG, the P wave is replaced by fibrillatory waves, called f waves, which fire at around 150-300 bpm and are present throughout the whole ECG recording. However, they are masked by the QRS complex and the T wave in each heartbeat. While AF is mainly characterized by an abnormal AA, ventricular response is also affected, as reflected by irregular RR intervals in an AF ECG. Figure 2.6 illustrates a comparison between the electrical propagation during a NSR and AF episodes.

The precise electrophysiological mechanisms underlying AF are still unclear, reflecting in the suboptimal success rate of AF treatments. Indeed, a better understanding of such mechanisms is essential to improve strategies for AF termination. In general, the temporal evolution of this arrhythmia has three phases: initiation, transition, and maintenance, which are described in more detail next.

<sup>6</sup><https://medimoon.com/wp-content/uploads/2014/02/atrial-fibrillation.jpg>

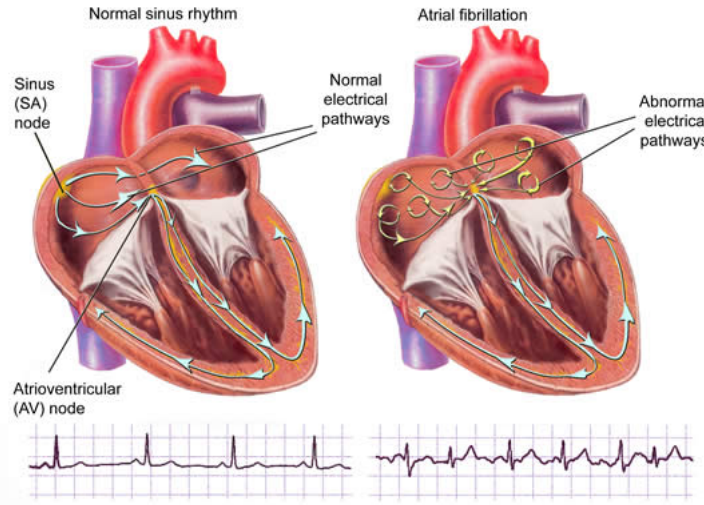


Figure 2.6: NSR *versus* AF<sup>6</sup>.

#### 2.7.2.1 Initiation

This temporal phase of AF consists in the rapid activation from several sources, such as the pulmonary veins and other venous (or non-venous) structures. Nonetheless, there is an intense debate about the mechanism of such activations [60].

In [11] it is suggested that this rapid activation is due to triggered activity, caused by an increase in the delay after depolarizations. The work [48] points out other ectopic mechanisms that can reflect unusual handling of calcium. Other studies suggest that this rapid activation is related to the cellular architecture and some electrophysiological properties of the pulmonary vein myocardium [34], [12], [68].

The initiation phase can last up to 2 minutes long (although the precise duration is still unclear) and leads to the transition phase.

#### 2.7.2.2 Transition

This phase is characterized by functional wavefront block and induction of reentry, that can be eased by several factors, as described in [60]. For example, atrial fibrosis, decreased activation latency, slowed conduction velocity, etc. The specific function of each factor (or the combinations of them) is still unclear, and may be specific to different patients. Research into treatments of the transition phase of AF are still being performed and focus on reducing the probability of wavefront block and induction of reentry.

#### 2.7.2.3 Maintenance

The main factor responsible for AF maintenance is still unclear. The major theories have been put forward in the literature [60]:

- **Multiwavelet reentry:** basically states that, during ongoing AF, the increased number of random wavelets promote sustained AF, difficulting its spontaneous termination [77].
- **Pulmonary vein triggers:** the role of pulmonary vein triggers during the initiation phase is generally acknowledged. However, their role during the maintenance

phase is an ongoing debate. The efficacy of pulmonary vein isolation is referred as an evidence to support this theory [102].

- **Autonomic sources:** this hypothesis affirms that sites with a great number of autonomic nerves, present throughout the atria, may play the role of AF sources, as a consequence of autonomic remodeling [85].
- **Rotors:** despite the little evidence of rotor sources in human AF, some studies have shown excellent outcomes in rotor ablation of AF [61], [71].

### 2.7.3 Classification

According to the clinical guidelines of the European Society of Cardiology [56], AF can be classified in five forms, regarding clinical presentation and duration of the episodes:

- **First detected AF:** when an AF episode is diagnosed for the first time by any electrocardiographic device. This first detection does not take into account the duration or the gravity of the AF episodes.
- **Paroxysmal AF:** also known as intermittent AF, it is a type of AF that self-terminates in less than 7 days, commonly within 48 hours.
- **Persistent AF:** represents a particularly complex case of this arrhythmia, where extensive atrial remodelling has taken place due to sustained AF, significantly affecting AA and AF perpetuation itself. Usually, persistent AF episodes last longer than 7 days and need termination by cardioversion.
- **Long-standing AF:** in this form of AF, episodes last longer than one year. Strategies to restore a normal heart rhythm are required. However, those methods are less likely to be effective than in earlier forms of the disease.
- **Permanent AF:** episodes are present for more than one year and strategies to restore a normal heart rhythm have failed or are no longer attempted. At this stage, the arrhythmia is accepted by both patient and cardiologist.

In addition to these five-type classification of AF, this arrhythmia can be also classified as Valvular AF, when it is caused by problems with the valves, like mitral valve stenosis or mitral regurgitation, and Nonvalvular AF, when the causes are not valve-related problems, like high blood pressure or stimulants (alcohol, caffeine, tobacco, etc). This binary classification is somehow important, as it has strong significance on appropriate AF treatments.

Another AF classification scheme was proposed in [54], that takes into account the degree of organization of the episodes, based on the bipolar atrial electrogram morphology and its baseline nature. This classification system characterizes AF into four types:

- **Type I:** distinguished by discrete atrial electrogram complexes of variable morphology. The isoelectric baseline is free of perturbation.
- **Type II:** atrial electrogram complexes are similar to Type I. However, the baseline is not isoelectric and has perturbations of several degrees.
- **Type III:** in this type, atrial electrograms have neither discrete complexes nor isoelectric intervals, presenting a completely chaotic nature.

- **Type IV:** reflected by alternating periods between atrial electrograms similar to Type III and the ones similar to Type I or Type II (or both).

Having knowledge of the type of this challenging cardiac arrhythmia is essential to decide what treatment is the most appropriate for the patient.

#### 2.7.4 Treatments

AF treatments focus on the prevention of AF burdens and the suppression of AF episodes, restoring the normal heart rate and rhythm. The choice of the best treatment for the patient significantly depends on several factors, including, AF type, patient health condition, cardiac disease history, etc. Mainly, there are three well-known types of AF treatments: pharmacological, electrical cardioversion, and catheter ablation.

##### 2.7.4.1 Pharmacological treatment

Pharmacological treatment is typically employed in patients suffering from an early stage of AF (like paroxysmal AF), where the episodes are short, since the efficacy of the medicaments are considerably reduced as AF episodes last longer than 48 hours [76]. There are three main drug categories that are employed in AF patients:

- **Blood clots prevention:** the risk of stroke is significantly increased with AF and is necessary to reduce the probability of blood clots formation. For this purpose, some medications like apixaban and edoxaban may be employed.
- **Normal heart rate restoration:** AF is a tachyarrhythmia, and then it is often necessary to reduce the heart rate. Some medications as atenolol, verapamil and propranolol may be used.
- **Normal heart rhythm restoration:** in addition to the fast heart rate, AF is characterized by the irregular heart beat, i.e., when the atria is unsynchronized with the ventricles. Medications like flecainide and amiodarone may be prescribed to restore NSR.

##### 2.7.4.2 Electrical cardioversion

The electrical cardioversion is a simple and efficient procedure in which a low-voltage electric current is applied to the chest wall to reset the heart rhythm back to NSR. The electric current causes all the heart cells to perform contraction at the same time, terminating the abnormal heart rhythm. If the initial shocks do not provide any success, the cardiologist can repeat the procedure again.

This is a non-emergency procedure to terminate AF that has not self-terminated and its success depends on the duration of AF episodes, being less successful for patients with AF episodes longer than 1 year.

##### 2.7.4.3 Catheter ablation procedure

When pharmacological treatment, electrical cardioversion, and other non-invasive AF therapies do not work, the cardiologist may suggest the catheter ablation procedure. It is a minimally invasive intervention that focuses on destroying sources of abnormal electrical activity in the heart tissue, in order to restore the normal heart rate and rhythm, terminating AF.

In this procedure, the cardiologist will insert several flexible thin tubes, named catheters, into the patient's blood vessels, usually through the femoral vein. The catheters are guided through the blood vessels towards the heart to burn (ablate) fibrillatory targets in the atria. Catheter ablation for AF has a significant success rate, which strongly depends on the correct choice of fibrillatory sites to be ablated. A common ablation strategy is pulmonary vein isolation, where the catheters are used to prevent that abnormal electrical signal triggers originating in the pulmonary veins enter the atria.

Generally, there are two types of catheter ablation, that are distinguished by the type of energy that is applied:

- **Radiofrequency ablation:** it is a heat-based procedure where electrical energy is delivered through the catheter to the fibrillatory sites in order to stop the abnormal rhythm conduction from these sites to the rest of the heart.
- **Cryoablation:** it is a cold-based procedure that focuses on removing the heat from the fibrillatory sites by using extreme cold. This way, the selected tissue will be destroyed, preventing the abnormal electrical conduction.

This procedure presents some risks, like bleeding, damage to the heart, infection, etc. After the ablation procedure finishes, the patient may rest in the bed for up to 8 hours and go home in the following day.

## 2.8 Summary

This introductory chapter has provided fundamental concepts of cardiology, electrophysiology and a general overview of the current knowledge of AF. Detailed description of the cardiac conduction system and the 12-lead ECG system configuration helps the reader to distinguish the differences between NSR and AF. A general description of this challenging cardiac disease, including its main causes and the known information about its electrophysiological mechanisms, generation and maintenance, show the reader the worrisome scenario caused by AF nowadays. Termination becomes increasingly difficult in advanced stages of this arrhythmia. Among the existing therapies, catheter ablation is a invasive procedure, that, although having a significant success rate, presents some risks. All this knowledge is necessary to understand the importance of non-invasive techniques to analyze AF, which is the focus of the next chapter.



# Noninvasive Atrial Activity Extraction

---

## Contents

<b>3.1</b>	<b>Introduction</b>	<b>23</b>
<b>3.2</b>	<b>Average beat subtraction</b>	<b>23</b>
<b>3.3</b>	<b>Weighed average beat subtraction</b>	<b>24</b>
<b>3.4</b>	<b>Spatio-temporal QRST cancellation</b>	<b>25</b>
<b>3.5</b>	<b>Adaptive singular value cancellation</b>	<b>25</b>
<b>3.6</b>	<b>Other methods for VA suppression</b>	<b>26</b>
<b>3.7</b>	<b>Blind source separation</b>	<b>27</b>
3.7.1	Principal component analysis	27
3.7.2	Independent component analysis	28
<b>3.8</b>	<b>Summary</b>	<b>30</b>

---

## 3.1 Introduction

This chapter presents the main signal processing techniques for non invasive AA extraction during AF that can be formulated by means of matrix algebra tools. The goal of this chapter is to provide the reader a state-of-the-art of the matrix-based methods along with their physiological links and constraints. The importance of this chapter relies on the limitations presented by the most used matrix-based AA extraction tools, which motivates the approach of the present doctoral thesis, that takes a step forward with the use of tensor factorization techniques to perform this task.

## 3.2 Average beat subtraction

Average beat subtraction (ABS) was first proposed as a method for P-wave identification in ventricular tachycardias [95]. A couple of years later, this method was used to extract f-waves from ECG recordings for AF analysis [96], since, during AF episodes, AA is assumed to be uncoupled from VA. Basically, this method consists in the computation of an average beat from a single lead of the ECG recording and its subtraction from each QRST complex, resulting in a signal that, ideally, contains the AA [100].

Before performing the subtraction, it is essential to align in time each average beat to each QRST complex, in order to avoid a resulting AA signal with ventricular residuals. This temporal alignment can be formulated as the following minimization problem:

$$\min_{\tau} \varepsilon(\tau) \triangleq \|\mathbf{x} - \mathbf{J}_{\tau}\bar{\mathbf{x}}\|^2 \quad (3.1)$$

where  $\mathbf{x} \in \mathbb{R}^{N \times 1}$  is the observed signal with  $N$  samples and  $\bar{\mathbf{x}} \in \mathbb{R}^{N+2\Delta \times 1}$  is the average beat signal with  $2\Delta$  additional samples, which are used for time alignment. The average beat is performed using algorithms for beat detection, such as the Pan-Tompkins algorithm [81]. Note that ABS performance is affected if incorrect detection appears. In order to allow for a temporal delay, a shift matrix  $\mathbf{J}_\tau$  is used, given by:

$$\mathbf{J}_\tau = [\mathbf{0}_{N \times \Delta+\tau} \quad \mathbf{I}_N \quad \mathbf{0}_{N \times \Delta-\tau}] \in \mathbb{R}^{N \times N+2\Delta} \quad (3.2)$$

where  $\tau$  is the time shift value.

ABS is easy implementable and, for single lead ECG processing, is the most widely used method, based on the assumption that an average beat can precisely model each individual QRST complex [2]. However, the QRST waveform is sensitive to some variations, mainly due to respiratory activity and ectopic beats, which have significant influence on the ECG leads, resulting in some ventricular residuals after performing ABS.

### 3.3 Weighed average beat subtraction

The weighed average beat subtraction (WABS) algorithm was later proposed in order to reduce the distortion present in the AA signal extracted by ABS [18]. This algorithm models the QRS template as the weighed average of the adjacent QRS complexes.

The QRS in  $i^{th}$  heartbeat can be expressed as:

$$x_i(m) = x_i^{VA}(m) + x_i^{AA}(m), \quad \text{for } m = 1, \dots, M \quad (3.3)$$

where  $x_i^{VA}(m)$  and  $x_i^{AA}(m)$  are the VA and AA, respectively, and  $M$  is the length of the QRS complex. The QRS template is computed as:

$$x_t(m) = \sum_{n=1}^N p_{n,m} x_n(m) \quad (3.4)$$

where  $\sum_{n=1}^N p_{n,m} = 1$ . The estimated AA signal is then given by:

$$\hat{x}_i^{AA}(m) = x_i(m) - x_t(m) \quad (3.5)$$

$$= x_i^{VA}(m) + x_i^{AA}(m) - \sum_{n=1}^N p_{n,m} x_n(m). \quad (3.6)$$

The estimating error can be expressed as:

$$e_i(m) = x_i^{VA}(m) - \sum_{n=1}^N p_{n,m} x_i^{VA}(m) - \sum_{n=1}^N p_{n,m} x_i^{AA}(m). \quad (3.7)$$

Since AA and VA are uncoupled during AF episodes,  $x_i^{AA}$  and  $x_i^{VA}$  can be seen as independent sources. Then, assuming that  $E(x^{AA}) = 0$  (which can be done by vertically shifting the ECG recording) one can have that:

$$E[e_i^2(m)] = \sigma_{x^{AA}}^2 \sum_{n=1}^N p_{n,m}^2 + \sigma_{x^{VA}(m)}^2 \left( 1 - 2p_{i,m} + \sum_{n=1}^N p_{n,m}^2 \right). \quad (3.8)$$

Then, considering  $P_m = [p_{1,m}, p_{2,m}, \dots, p_{N,m}]$ , the optimum coefficients acquired by solving  $\hat{P}_m = \arg \min E[e_i^2(m)]$  subject to  $\sum_{n=1}^N p_{n,m} = 1$  are given by [18]:

$$\hat{P}_{n,m} = \begin{cases} \frac{\sigma_{x^{AA}}^2 / N}{\sigma_{x^{AA}}^2 + \sigma_{x^{VA}(m)}^2}, & n \neq i \\ \frac{\sigma_{x^{VA}(m)}^2 + \sigma_{x^{AA}}^2 / N}{\sigma_{x^{AA}}^2 + \sigma_{x^{VA}(m)}^2}, & n = i \end{cases} \quad (3.9)$$

The WABS algorithm provides a better performance than the ABS method, specially when the QRS morphology varies more. However, the WABS cannot model a T wave template, as in many AF episodes the T wave is difficult to detect, and only the QRS complex is cancelled with this technique.

### 3.4 Spatio-temporal QRST cancellation

Aiming to overcome the limitation of ABS by exploring multi-lead ECG processing, the spatio-temporal QRST cancellation method [101] replaces the single lead vector  $\mathbf{x} \in \mathbb{R}^{N \times 1}$  by the multi-lead matrix  $\mathbf{X} \in \mathbb{R}^{N \times K}$ , composed of  $K$  signal leads with  $N$  samples each. As stated before, AA and VA are assumed to be uncoupled during AF, allowing  $\mathbf{X}$  to be modeled as:

$$\mathbf{X} = \mathbf{X}_{AA} + \mathbf{X}_{VA} + \mathbf{N} \quad (3.10)$$

where  $\mathbf{N}$  is an additive noise, representing other interference signals,  $\mathbf{X}_{AA}$  is the AA signal, and  $\mathbf{X}_{VA}$  is the VA signal, modeled as:

$$\mathbf{X}_{VA} = \mathbf{J}_\tau \bar{\mathbf{X}} \mathbf{S} \quad (3.11)$$

where  $\bar{\mathbf{X}} \in \mathbb{R}^{N+2\Delta \times K}$  is the average beat matrix and  $\mathbf{S} \in \mathbb{R}^{K \times K}$  is a spatial alignment matrix that admits the factorization  $\mathbf{S} = \mathbf{D}\mathbf{Q}$ , with  $\mathbf{D}$  being a diagonal amplitude scaling matrix and  $\mathbf{Q}$  a rotation matrix. The role of matrix  $\mathbf{S}$  is to transfer information between ECG leads, in order to compensate for some variations in the electrical axis of the heart and tissue conductivity [100].

Now, replacing (3.11) in (3.10), we have:

$$\mathbf{X} - \mathbf{J}_\tau \bar{\mathbf{X}} \mathbf{D} \mathbf{Q} = \mathbf{X}_{AA} + \mathbf{N}. \quad (3.12)$$

From (3.12) one can see that the accuracy of the fitting  $\mathbf{X} - \mathbf{J}_\tau \bar{\mathbf{X}} \mathbf{D} \mathbf{Q}$  is limited not only by  $\mathbf{N}$ , but so also by  $\mathbf{X}_{AA}$ . To handle this, an intermediate estimate  $\tilde{\mathbf{X}}_{AA}$ , representing a reconstructed signal that contains only fibrillatory waveforms, is subtracted from both sides of (3.12):

$$\mathbf{Y} - \mathbf{J}_\tau \bar{\mathbf{X}} \mathbf{D} \mathbf{Q} = \mathbf{X}_{AA} - \tilde{\mathbf{X}}_{AA} + \mathbf{N} \quad (3.13)$$

where  $\mathbf{Y} = \mathbf{X} - \tilde{\mathbf{X}}_{AA}$ . This strategy is called AF reduction, and reconstructs a signal with fibrillatory waveforms by interpolating successive TQ intervals (where only AA is observed) in order to fill the QT interval with f-waves [101]. Then the problem relies on the estimation of  $\tau$ ,  $\mathbf{D}$  and  $\mathbf{Q}$  by solving the following minimization problem:

$$\min_{\tau, \mathbf{D}, \mathbf{Q}} \varepsilon(\tau, \mathbf{D}, \mathbf{Q}) \triangleq \|\mathbf{Y} - \mathbf{J}_\tau \bar{\mathbf{X}} \mathbf{D} \mathbf{Q}\|_F^2. \quad (3.14)$$

In (3.14), it is assumed that  $\mathbf{D}$  is known and  $\mathbf{Q}$  is minimized with an alternating and iterative approach using the singular value decomposition (SVD), whereas  $\tau$  is minimized by an exhaustive search in the interval  $[-\Delta, \Delta]$  [100], [101].

### 3.5 Adaptive singular value cancellation

Also in order to overcome the limitations of the ABS technique, an alternative QRST cancellation method called adaptive singular value cancellation (ASVC), applied to each single beat, was proposed in [2]. This strategy is able to extract the VA basis signal

by exploiting the mutual information available in the set of QRST complexes under processing.

First, all the R waves are detected by the Pan-Tompkins algorithm. Then, the  $i^{\text{th}}$  QRST complex start point is defined as:

$$s_i = r_i - 0.3RR_{\min} \quad (3.15)$$

where  $r_i$  is the R peak wave event and  $RR_{\min}$  is the minimum RR interval found in the analyzed ECG. The  $i^{\text{th}}$  QRST complex end point is then selected as  $e_i = r_i + 0.7RR_{\min}$ .

Representing each N-sample QRST complex as a column vector  $\mathbf{x}_i$  and stacking them into a matrix as  $\mathbf{X} = [\mathbf{x}_1 \ \mathbf{x}_2 \ \dots \ \mathbf{x}_K] \in \mathbb{R}^{N \times K}$ , one can express the SVD of  $\mathbf{X}$  as:

$$\mathbf{X} = \mathbf{U}\Sigma\mathbf{V}^T \quad (3.16)$$

where matrix  $\mathbf{U}$  holds the  $K$  normalized principal components of  $\mathbf{X}$  and matrix  $\Sigma$  holds the amplitude coefficients corresponding to the  $K$  principal components of matrix  $\mathbf{X}$  [2].

Then, the  $K$  non-normalized principal components can be obtained as the columns of the matrix  $\mathbf{P} = \mathbf{U}\Sigma$ , where the first component corresponds to the main VA, the following components are related to AA, and the remaining ones to the noise. This way, one can use the first principal component of  $\mathbf{X}$ , denoted  $\mathbf{t}$ , as a QRST template to cancel out VA, as it contains the basis representation of the QRST complexes in the analyzed ECG [2].

Finally, each amplitude is individually adapted to each QRST complex as:

$$\mathbf{v}\mathbf{a}_i = \frac{QR_i}{QR_t} \mathbf{t} \quad (3.17)$$

where  $QR_i$  and  $QR_t$  are the amplitude distances between the Q and R points of the  $i^{\text{th}}$  complex and the template, respectively [2].

Stacking each column vector  $\mathbf{v}\mathbf{a}_i$  into a matrix as  $\mathbf{VA} = [\mathbf{v}\mathbf{a}_1 \ \mathbf{v}\mathbf{a}_2 \ \dots \ \mathbf{v}\mathbf{a}_K] \in \mathbb{R}^{N \times K}$ , the AA estimation contained in each QRST interval can be acquired as:

$$\hat{\mathbf{X}}_{AA} = \mathbf{X} - \mathbf{VA} \in \mathbb{R}^{N \times K}. \quad (3.18)$$

The ASVC technique is able to individually adapt the amplitude to each heart beat, providing a better performance than the ABS method. However, this technique still requires a sufficient number of beats to explore the mutual information among different QRST complexes of the same ECG. Also, one must note that the estimated AA will contain the noise present in the ECG, although part of this interference signal is suppressed during the pre-processing.

### 3.6 Other methods for VA suppression

Many other methods for VA cancellation are proposed apart from the classical ones previously described. In [18] an AA extraction method based on maximum likelihood estimation is put forward. This method is optimum by means of maximum probability, as it aims to obtain the most possible AA signal. It basically consists in modeling the probability density functions of AA and VA signals using a Gaussian model and then, extracting the AA by maximizing the likelihood function. Two different methods are proposed in [69]. The first one is an ABS-based method that creates two templates: one for the ventricular depolarization and other for the ventricular repolarization. The

second one consists in suppressing the VA in each heartbeat in an independent way and also treats the ventricular depolarization and repolarization separately. A novel method based on an echo state neural network is introduced in [84], which suppresses the VA by estimating the time-varying, nonlinear transfer function between two leads: one with AA and other without. The network adapts the weights that define the output layers for every new sample to be processed. More recently, we may cite the method proposed in [75], which is an ABS-based algorithm, where the VA template is estimated by combining the diffusion distance and the non-local Euclidean median. This algorithm operates on single leads and is very suitable for long-term monitoring, such as Holter recordings. Also, we may cite the work [90], where a Bayesian filtering framework is put forward to separate AA and VA during AF episodes. In this framework, the waves that represent the VA are modeled with a sum of Gaussian functions, whereas the f waves, representing the AA, are modeled using a trigonometrical function. Then, the state variables of both models are estimated using a Kalman smoother.

### 3.7 Blind source separation

The previous mentioned methods focus on the VA cancellation by the suppression of the QRST complex from the ECG. Despite differences in performance, they share the same limitations, like the inability to eliminate artifacts from electrode movement [88] and the needing of ECG recordings of long duration, in order to perform an accurate average beat estimation. Nonetheless, recalling that AA and VA are assumed to be uncoupled during AF, this allows, under certain assumptions, the AA extraction problem to accept a blind source separation (BSS) formulation [88]. In AF ECG recordings, AA and VA are mixed at the electrode outputs in the ECG.

Indeed, ECG recordings from  $K$  leads composed of  $N$  time samples can be stored in a matrix:

$$\mathbf{Y} = \mathbf{MS} \in \mathbb{R}^{K \times N} \quad (3.19)$$

where  $\mathbf{M} \in \mathbb{R}^{K \times R}$  is the mixing matrix, modeling the propagation of the cardiac electrical sources from the heart to the body surface,  $\mathbf{S} \in \mathbb{R}^{R \times N}$  is the source matrix that contains the atrial, ventricular and some interference sources (noise, respiration, muscular activity, etc.), and  $R$  is the number of sources [109]. Since the goal is to estimate  $\mathbf{M}$  and  $\mathbf{S}$  from matrix  $\mathbf{Y}$  (the only observed data), it is clear that AA extraction in an AF ECG recording is a BSS problem. The BSS model is justified by considerations from the direct problem in electrocardiography [88].

The main disadvantage of the matrix model (3.19) is the lack of uniqueness. Indeed, consider the matrices  $\mathbf{M}' = \mathbf{MA}$  and  $\mathbf{S}' = \mathbf{A}^{-1}\mathbf{S}$ , where  $\mathbf{A} \in \mathbb{R}^{R \times R}$  is an arbitrary nonsingular matrix, one can see that:

$$\mathbf{Y} = (\mathbf{MA})(\mathbf{A}^{-1}\mathbf{S}) = \mathbf{M}'\mathbf{S}' . \quad (3.20)$$

For this reason, matrix-based techniques need to impose further constraints on  $\mathbf{M}$  and  $\mathbf{S}$  in order to ensure the uniqueness of the decomposition.

#### 3.7.1 Principal component analysis

The principal components analysis (PCA) consists in performing an orthogonal linear transformation of the data by maximizing the joint variance in the least-squares sense of the resulting principal components [53]. When applied to multi-lead ECG recordings,

PCA becomes a BSS tool that was first used for AA extraction during AF in [66]. This method decomposes the multi-lead ECG in a way that the first components correspond to VA signals, whereas the next components typically includes the AA signal and noise signals present in the ECG [100].

Considering the ECG data matrix  $\mathbf{Y}$  in (3.19), PCA exploits inter-lead correlation by estimating the correlation matrix as:

$$\hat{\mathbf{R}}_{YY} = \frac{1}{N} \mathbf{Y} \mathbf{Y}^T \in \mathbb{R}^{K \times K}. \quad (3.21)$$

Then, the orthogonal linear transformation used to compute the principal components is given by the eigenvectors  $\Psi$  resulting from the diagonalization of  $\hat{\mathbf{R}}_{YY}$ . The mutually uncorrelated principal components are then given by:

$$\mathbf{w}_{.n} = \Psi^T \mathbf{y}_{.n}. \quad (3.22)$$

Comparing (3.22) and (3.19), one can see that PCA obtains the following BSS estimates:

$$\begin{aligned}\hat{\mathbf{M}} &= \Psi \\ \hat{\mathbf{S}} &= \Psi^T \mathbf{Y}.\end{aligned}$$

Note that  $\hat{\mathbf{M}}$  always has, by definition, orthogonal columns. Hence, PCA is only expected to provide a successful source separation when the true mixing matrix  $\mathbf{M}$  also has orthogonal columns.

### 3.7.2 Independent component analysis

The performance of PCA considerably depends on the orthogonality of the columns of the mixing matrix. Generally, such orthogonality can only be assured through an appropriate placement of electrodes and will be strongly patient-dependent. Also, PCA is a second-order statistical approach, and since AA and VA are assumed to be independent at orders higher than two with non-Gaussian distribution [101], [88], a method that exploits higher order statistics is expected to provide a better performance.

The independent component analysis (ICA) [14] is a powerful method that separates a multivariate signal into subcomponents, assuming that they are statistically mutually independent with non-Gaussian distribution. Considering the BSS model of (3.19), the goal of ICA is to solve the following linear equation system:

$$\hat{\mathbf{S}} = \Omega \mathbf{Y} \quad (3.23)$$

where the source matrix estimate  $\hat{\mathbf{S}}$  contains signals that are statistically independent and the linear transformation matrix  $\Omega$  has full column rank, being able to have any structure. Many ICA-based methods have been developed over the years [16], like FastICA [50] and RobustICA [112]. Such algorithms have been applied in several research areas, with a particular success in biomedical engineering. In particular, RobustICA presents some advantages over other ICA techniques, such as:

- The treatment of real- and complex-valued source signals by the same algorithm.
- No requirement of prewhitening, avoiding the limitations it imposes and improving asymptotic performance.

- The capability to deal with sub- and super-Gaussian sources.
- A considerably high convergence speed by means of source extraction quality versus number of operations.

RobustICA is based on the normalized kurtosis contrast function, which is globally optimized by an algebraically iterative technique, being able to extract any independent component with non-zero kurtosis. This algorithm along with all its advantages are described in [112].

In AA extraction for AF analysis, ICA was first applied in [89] and needs the fulfillment of three basic assumptions [88]:

1. **Statistical independence between AA and VA:** during AF episodes, several independent electrical impulses are generated and propagated throughout the atria. However, only a small part of them reaches the AV node, which tends to limit the ventricular activation [70], [51]. This makes the atria and the ventricles beat in a unsynchronized and irregular way, making reasonable to consider AA and VA as physically independent activities, thus, being generated by statistically independent cardioelectric sources [88].
2. **AA and VA have non-Gaussian distribution:** during the circulatory circuit, VA presents low values except during the ventricular depolarization, presenting high values represented by the QRS complex in the ECG. This makes the histogram of VA present a super-Gaussian distribution [93]. During AF episodes, the f-waves characterizing AA can be well-modeled as a sawtooth signal with several harmonics [101], whose histogram presents then a sub-Gaussian distribution.
3. **ECG is an instantaneous linear mixture model:** in [88], it was shown that the electrical potential at any point of the body surface can be obtained by a linear combination of the heart potentials, that is:

$$\Phi_B = T_{BH} \Phi_H , \quad (3.24)$$

where  $\Phi_B$  and  $\Phi_H$  are potential column vectors on the body surface (representing the leads) and on the epicardium (representing the sources), respectively, and  $T_{BH}$  is a transfer matrix. From (3.24) one can see that the ECG data matrix corresponds to a linear mixing model where a set of potentials on the body surface (leads) are obtained by a linear combination of a set of bioelectric potentials (cardiac sources).

It is important to highlight that interference sources that come from outside the heart (respiration, muscular activity, etc.) are necessarily independent. However, some types of interference sources, as muscular activity, are approximately Gaussian [13], which may cause some muscular residuals in the component that contains the AA.

Matrix-based techniques to solve BSS problems, such as PCA and ICA previously described, have proven useful in noninvasive AA extraction [66], [35], [88], [10], [109], [100]. However, matrix decompositions are known to have some limitations, since constraints need to be imposed to guarantee uniqueness: orthogonality of the mixing matrix (PCA) or statistical independence between the sources (ICA). Such constraints are mathematically convenient, but they may lack physiological grounds, making difficult the results interpretation.

Table 3.1: Summary of the matrix-based AA extraction techniques with their goals, advantages and limitations.

Method	Goal	Advantage	Limitations
<b>ABS</b>	QRST suppression	Easy implementation	Sensitive to QRST variations
			Long ECG recordings
<b>WABS</b>	QRST suppression	Optimum QRS template	Cannot model T wave
			Long ECG recordings
<b>S-T QRST Canc.</b>	QRST suppression	Multi-lead ECG	Artifacts from electrode movement
			Long ECG recordings
<b>ASVC</b>	QRST suppression	QRST mutual information	Noise residuals
			Long ECG recordings
<b>PCA</b>	BSS	Uncoupling of VA and AA	Orthogonal mixing matrix
		Short ECG recordings	Performance patient-dependent
		Multi-lead ECG	Second-order statistics
<b>ICA</b>	BSS	Uncoupling of VA and AA	Sources statistical independent
		Short ECG recordings	Muscular residuals
		High-order statistics	
		Multi-lead ECG	

### 3.8 Summary

This chapter provided a global overview of the main non-invasive AA extraction tools, with their advantages and limitations. To date, the techniques that fully exploit the spatial diversity of the ECG are the matrix-based methods to solve BSS problems. However, such matrix factorization tools require strong constraints to guarantee uniqueness. PCA requires the columns of the mixing matrix  $\mathbf{M}$  to be orthogonal. On the other hand, ICA assumes an arbitrary mixing matrix  $\mathbf{M}$  as long as it is full column rank, but imposes statistical independence between the sources, requiring high-order statistics for proper exploitation. Matrix-based AA extraction techniques with their goals, advantages and limitations are summarized on Table 3.1.

In the next chapter, it will be shown that, if compared to matrix-based techniques, tensor decompositions present some remarkable features like, for example, their essential uniqueness under more relaxed constraints. Another example is the fact that the rank of the tensor can exceed its largest dimension, whereas in matrices the rank is limited by its lowest dimension. These interesting features open promising prospects for the use of tensor techniques for BSS in general and AA extraction in AF ECGs in particular.

## CHAPTER 4

# Concepts of Tensor Algebra

---

## Contents

---

<b>4.1</b>	<b>Introduction</b>	<b>31</b>
<b>4.2</b>	<b>Introduction to multilinear algebra</b>	<b>31</b>
<b>4.3</b>	<b>Tensor decompositions</b>	<b>34</b>
4.3.1	PARAFAC decomposition	34
4.3.2	Tucker-3 decomposition	36
4.3.3	PARATUCK decomposition	38
<b>4.4</b>	<b>Block term decomposition</b>	<b>39</b>
<b>4.5</b>	<b>Coupled block term decomposition</b>	<b>40</b>
<b>4.6</b>	<b>Hankel-BTD as an AA extraction tool</b>	<b>41</b>
<b>4.7</b>	<b>Summary</b>	<b>43</b>

---

## 4.1 Introduction

ECG analysis techniques studied in this doctoral thesis are based on tensor decompositions. In order to facilitate the comprehension of the tensor-based ECG modeling and further contributions presented later in the thesis, this chapter introduces the basic concepts and tools of multilinear algebra. Important definitions of the tensor algebra are first introduced, followed by the main tensor decompositions. The chapter ends presenting the BTD built from Hankel matrices and its application in the non-invasive AA extraction from AF ECGs.

## 4.2 Introduction to multilinear algebra

In the literature, one can find different definitions of the word tensor. Indeed, depending on the research field, the definition of tensors can be a little bit different. Our approach is focused on digital signal processing, where a tensor is used to generalize the representations of scalars, vectors, and matrices. In the literature, several definitions of tensors that leads to the same concept can be found. For example, [15] defines a tensor as a mathematical entity that has multilinearity properties after a change of the coordinate system. In [58] a tensor is defined as a multidimensional array. In other words, a  $N^{\text{th}}$ -order (or  $N$ -way) tensor is a multilinear array that results from the tensor product of  $N$  vector spaces, where each one has its own coordinate system. Also, [63] interprets a  $N^{\text{th}}$ -order tensor as an array that offers a linear dependency regarding  $N$  vector spaces, where elements can be accessed by  $N$  indices.

The present doctoral thesis will use the definition that treats a tensor as a multidimensional array [58]. A zero-order tensor is a scalar, a first-order tensor is a vector, a second-order tensor is a matrix, a third-order tensor is a rectangular cuboid, and so

on.  $N^{\text{th}}$ -order tensors, where  $N \geq 3$ , are called higher-order tensors. The goal of this chapter is to provide an overview of higher-order tensors, as well as some of its most known decompositions.

Some definitions are very important to the understanding of tensor algebra, like, for example, the outer product between tensors. Let  $\mathcal{X} \in \mathbb{C}^{I_1 \times I_2 \times \dots \times I_N}$  be a  $N^{\text{th}}$ -order tensor and  $\mathcal{Y} \in \mathbb{C}^{J_1 \times J_2 \times \dots \times J_M}$  a  $M^{\text{th}}$ -order tensor. The outer product between these two arbitrary tensors is given by:

$$\mathcal{Z}_{i_1, i_2, \dots, i_N, j_1, j_2, \dots, j_M} = [\mathcal{X} \circ \mathcal{Y}]_{i_1, i_2, \dots, i_N, j_1, j_2, \dots, j_M} = x_{i_1, i_2, \dots, i_N} y_{j_1, j_2, \dots, j_M}. \quad (4.1)$$

Note that the outer product of  $\mathcal{X}$  and  $\mathcal{Y}$  is another tensor  $\mathcal{Z}$ , with order given by the sum of the orders of the two other tensors, that is,  $N + M$ .

Given matrices  $\mathbf{A} \in \mathbb{C}^{I_1 \times I_2}$ ,  $\mathbf{B} \in \mathbb{C}^{I_3 \times I_4}$  and  $\mathbf{C} \in \mathbb{C}^{I_5 \times I_2}$ , the Kronecker product, represented by  $\otimes$ , between matrices  $\mathbf{A}$  and  $\mathbf{B}$  is given by:

$$\mathbf{A} \otimes \mathbf{B} = \begin{bmatrix} a_{11}\mathbf{B} & \dots & a_{1I_2}\mathbf{B} \\ \vdots & \ddots & \vdots \\ a_{I_1}\mathbf{B} & \dots & a_{I_1I_2}\mathbf{B} \end{bmatrix} \in \mathbb{C}^{I_1 I_3 \times I_2 I_4}. \quad (4.2)$$

The Khatri-Rao (column-wise Kronecker) product, represented by  $\diamond$ , between matrices  $\mathbf{A}$  and  $\mathbf{C}$  is given by:

$$\mathbf{A} \diamond \mathbf{C} = [\mathbf{a}_{\cdot 1} \otimes \mathbf{c}_{\cdot 1} \quad \dots \quad \mathbf{a}_{\cdot I_2} \otimes \mathbf{c}_{\cdot I_2}] \in \mathbb{C}^{I_1 I_5 \times I_2}. \quad (4.3)$$

If the matrices  $\mathbf{A}$  and  $\mathbf{C}$  are partitioned into matrices, i.e.,  $\mathbf{A} = [\mathbf{A}_1 \quad \dots \quad \mathbf{A}_R]$  and  $\mathbf{C} = [\mathbf{C}_1 \quad \dots \quad \mathbf{C}_R]$ , where  $\mathbf{A}_r \in \mathbb{C}^{I_1 \times L_r}$  and  $\mathbf{C}_r \in \mathbb{C}^{I_5 \times K_r}$ , then we can alternatively define the Khatri-Rao product as the partition-wise Kronecker product, denoted  $\odot$ , as [64]:

$$\mathbf{A} \odot \mathbf{C} = [\mathbf{A}_1 \otimes \mathbf{C}_1 \quad \dots \quad \mathbf{A}_R \otimes \mathbf{C}_R] \in \mathbb{C}^{I_1 I_5 \times \sum_{r=1}^R L_r K_r}. \quad (4.4)$$

The block Khatri-Rao product, represented by  $\diamond_K$ , between matrices  $\mathbf{X} = [\mathbf{x}_1 \cdots \mathbf{x}_R] \in \mathbb{C}^{I \times R}$  and  $\mathbf{Y} = [\mathbf{y}_1 \cdots \mathbf{y}_{KR}] \in \mathbb{C}^{J \times KR}$ , yields a horizontal block matrix that has its  $r^{\text{th}}$  block given by:

$$[\mathbf{X} \diamond_K \mathbf{Y}]_r = \mathbf{x}_r \otimes [\mathbf{y}_{(r-1)K+1} \cdots \mathbf{y}_{(r-1)K+K}] \in \mathbb{C}^{IJ \times K}. \quad (4.5)$$

Another important definition in tensor algebra is the concept of the rank of a tensor. Considering the previously defined  $N^{\text{th}}$ -order tensor  $\mathcal{X}$ , its rank is denoted by  $\text{rank}(\mathcal{X})$  and is defined as the minimal number of rank-1 tensors that linearly combined yield exactly  $\mathcal{X}$ . Particularly, a rank-1 tensor can be written as the outer product of  $N$  vectors, that is:

$$\mathcal{X} = \mathbf{v}^{(1)} \circ \mathbf{v}^{(2)} \circ \dots \circ \mathbf{v}^{(N)}, \quad (4.6)$$

where  $\mathcal{X}$  is the rank-1 tensor and  $\mathbf{v}^{(n)} \in \mathbb{C}^{I_n}$ , for  $n = 1, \dots, N$ , are the vectors called the components of  $\mathcal{X}$ . In the present doctoral thesis as well as in many works based on tensor algebra, the Frobenius norm of a tensor, that is interpreted as the energy of the tensor, is often used. The Frobenius norm of the arbitrary tensor  $\mathcal{X}$ , is given by:

$$\|\mathcal{X}\|_F = \left( \sum_{i_1=1}^{I_1} \sum_{i_2=1}^{I_2} \dots \sum_{i_N=1}^{I_N} |x_{i_1, i_2, \dots, i_N}|^2 \right)^{\frac{1}{2}}. \quad (4.7)$$

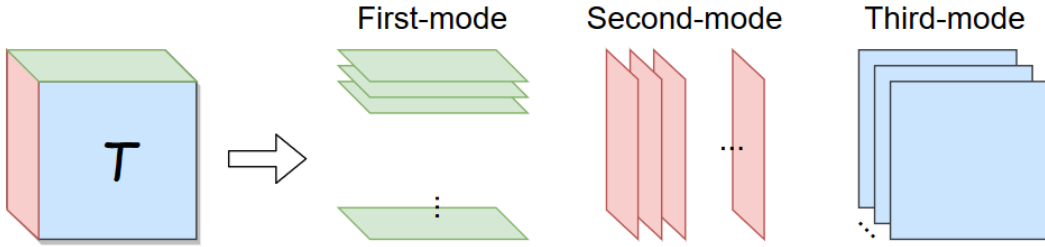


Figure 4.1: Matrix slices of a third-order tensor.

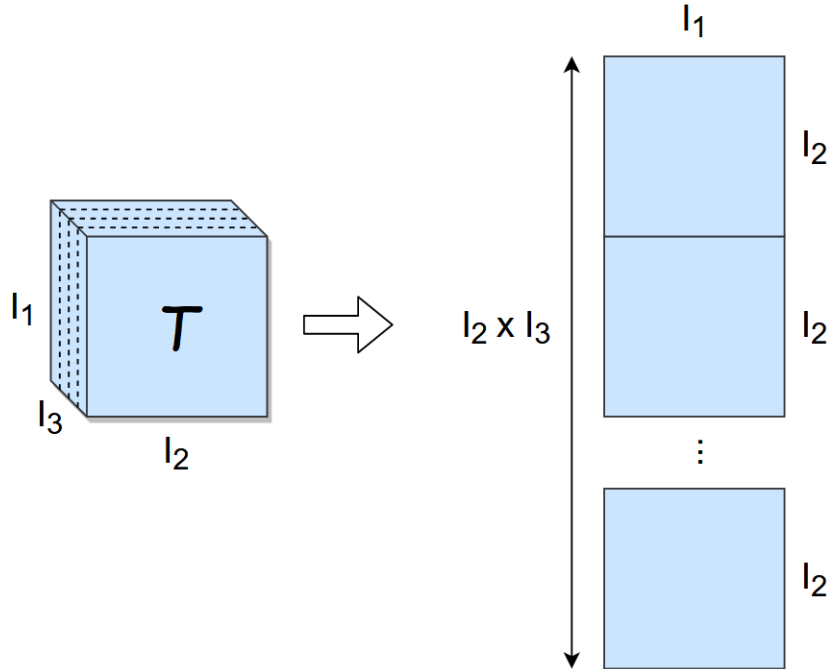


Figure 4.2: Mode-1 matrix unfolding of a third-order tensor.

Before presenting and describing some remarkable tensor decompositions, three basic concepts need to be introduced. The first one is the definition of the matrix slices, which are all the two-dimensional sections of a tensor, by fixing all but two indices of it [58]. For an arbitrary third-order tensor, Figure 4.1 illustrates the three modes matrix slices.

The second one is the concept of matrix unfoldings of a tensor. The  $n^{\text{th}}$ -mode matrix unfolding  $\mathbf{T}_n$  of a tensor  $\mathcal{T} \in \mathbb{C}^{I_1 \times I_2 \times \dots \times I_N}$  is defined as a matrix of dimensions  $I_1 I_2 \dots I_{n-1} I_{n+1} I_N \times I_n$ , which is obtained by stacking all the matrix slices that compose the  $n^{\text{th}}$ -mode of the tensor. Indeed, by using the definition of slices previously described, one can say that the matrix unfolding is obtained by all the matrix slices stacked in a given mode of the tensor. The way that these slices are stacked depends on the definition of the matrix unfolding, which may vary among different works in the literature. Again, we follow the definition of [58].

In Figure 4.2, the mode-1 matrix unfolding of dimensions  $I_2 I_3 \times I_1$  of an arbitrary third-order tensor  $\mathcal{T} \in \mathbb{C}^{I_1 \times I_2 \times I_3}$  is illustrated for clarity. Mode-2 and mode-3 matrix unfoldings can be derived analogously.

The third and last one is the concept of mode- $n$  rank of a tensor, which is defined as the rank of its mode- $n$  matrix unfolding, i.e.,  $\text{rank}(\mathbf{T}_n)$ . A third-order tensor has multilinear rank- $(L_1, L_2, L_3)$  if its mode-1 rank, mode-2 rank, and mode-3 rank are

equal to  $L_1$ ,  $L_2$ , and  $L_3$ , respectively [64, Definition 1.6].

## 4.3 Tensor decompositions

Tensor decompositions aim at representing a tensor as a sum of simpler tensors or components. In turn, each component is obtained from some matrix or vector factors. For instance, in the PARAllel FACTor (PARAFAC) decomposition, the tensor is represented by a linear combination of outer product factors, as it will be described later in this chapter. Tensor decompositions are very useful tools in problems where the multilinear nature of the data can be explored. Significant contributions of these remarkable multilinear factorization methods have been made in several research fields, as for example, signal processing, wireless communications, biomedical engineering, blind source separation, chemometrics, psychometrics, and many others.

### 4.3.1 PARAFAC decomposition

The PARAFAC decomposition (or polyadic decomposition, or even CANDECOMP) was first proposed by Frank L. Hitchcock [47] in 1927 and then, was developed by Richard A. Harshman [45] and J. Douglas Carroll & Jih-Jie Chang [9] in different works in 1970. Considering a third-order tensor, one can say that this decomposition is a sum of triple products, or equivalently, a sum of several rank-1 tensors. The PARAFAC decomposition of an arbitrary third-order tensor  $\mathcal{X} \in \mathbb{C}^{I_1 \times I_2 \times I_3}$  can be written in scalar form as:

$$x_{i_1, i_2, i_3} = \sum_{r=1}^R a_{i_1, r} b_{i_2, r} c_{i_3, r}, \quad (4.8)$$

where  $a_{i_1, r}$ ,  $b_{i_2, r}$  and  $c_{i_3, r}$  are the scalar components of factor matrices  $\mathbf{A} \in \mathbb{C}^{I_1 \times R}$ ,  $\mathbf{B} \in \mathbb{C}^{I_2 \times R}$  and  $\mathbf{C} \in \mathbb{C}^{I_3 \times R}$ , respectively, and  $R$  is the rank of the decomposition (or the number of factors). If  $R$  is minimal, then the decomposition is called canonical, referred to as canonical polyadic decomposition (CPD), and then  $R$  is the rank of the tensor. The PARAFAC decomposition can also be written using the outer product notation as:

$$\mathcal{X} = \sum_{r=1}^R \mathbf{A}_{\cdot r} \circ \mathbf{B}_{\cdot r} \circ \mathbf{C}_{\cdot r} = \sum_{r=1}^R \mathbf{a}_r \circ \mathbf{b}_r \circ \mathbf{c}_r. \quad (4.9)$$

where  $\mathbf{a}_r$ ,  $\mathbf{b}_r$ , and  $\mathbf{c}_r$  are the  $r^{\text{th}}$  column vectors of matrices  $\mathbf{A}$ ,  $\mathbf{B}$ , and  $\mathbf{C}$ , respectively, and are also known as factor vectors. A compact notation of the PARAFAC decomposition can be written as:

$$\mathcal{X} = [\![\mathbf{A}, \mathbf{B}, \mathbf{C}]\!]. \quad (4.10)$$

A PARAFAC decomposition of an arbitrary third-order tensor  $\mathcal{X}$  is illustrated in Figure 4.3 as a sum of  $R$  rank-1 tensors.

One can represent the matrix slices of the PARAFAC decomposition of the third-order tensor previously defined as:

$$\mathbf{X}_{i_1 \cdot \cdot} = \mathbf{B} D_{i_1}(\mathbf{A}) \mathbf{C}^T \quad (4.11)$$

$$\mathbf{X}_{\cdot i_2 \cdot} = \mathbf{C} D_{i_2}(\mathbf{B}) \mathbf{A}^T \quad (4.12)$$

$$\mathbf{X}_{\cdot \cdot i_3} = \mathbf{A} D_{i_3}(\mathbf{C}) \mathbf{B}^T. \quad (4.13)$$

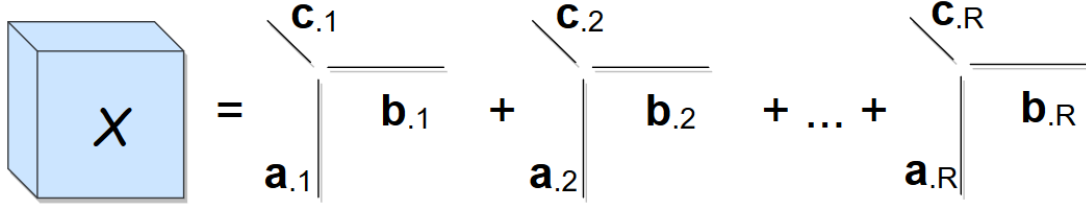


Figure 4.3: Illustration of the PARAFAC or polyadic decomposition of a third-order tensor as a sum of  $R$  rank-1 tensors.

A celebrated property states that:

$$\mathbf{A} \diamond \mathbf{B} = \begin{bmatrix} \mathbf{B}D_1(\mathbf{A}) \\ \vdots \\ \mathbf{B}D_{I_1}(\mathbf{A}) \end{bmatrix}. \quad (4.14)$$

If we stack the first-, second- and third-mode slices, according to (4.14) we will have the matrix unfoldings given by:

$$\mathbf{X}_1 = \begin{bmatrix} \mathbf{X}_{.1.} \\ \vdots \\ \mathbf{X}_{.I_2.} \end{bmatrix} = \begin{bmatrix} \mathbf{C}D_1(\mathbf{B}) \\ \vdots \\ \mathbf{C}D_{I_2}(\mathbf{B}) \end{bmatrix} \mathbf{A}^T = (\mathbf{B} \diamond \mathbf{C})\mathbf{A}^T \in \mathbb{C}^{I_2 I_3 \times I_1} \quad (4.15)$$

$$\mathbf{X}_2 = \begin{bmatrix} \mathbf{X}_{..1} \\ \vdots \\ \mathbf{X}_{..I_3} \end{bmatrix} = \begin{bmatrix} \mathbf{A}D_1(\mathbf{C}) \\ \vdots \\ \mathbf{A}D_{I_3}(\mathbf{C}) \end{bmatrix} \mathbf{B}^T = (\mathbf{C} \diamond \mathbf{A})\mathbf{B}^T \in \mathbb{C}^{I_3 I_1 \times I_2} \quad (4.16)$$

$$\mathbf{X}_3 = \begin{bmatrix} \mathbf{X}_{1..} \\ \vdots \\ \mathbf{X}_{I_1 ..} \end{bmatrix} = \begin{bmatrix} \mathbf{B}D_1(\mathbf{A}) \\ \vdots \\ \mathbf{B}D_{I_1}(\mathbf{A}) \end{bmatrix} \mathbf{C}^T = (\mathbf{A} \diamond \mathbf{B})\mathbf{C}^T \in \mathbb{C}^{I_2 I_1 \times I_3}. \quad (4.17)$$

The PARAFAC decomposition can be unique for ranks greater than one up to scaling and permutation factors. To understand the PARAFAC uniqueness condition, lets first define the concept of Kruskal-rank (k-rank), proposed by Kruskal in 1977 [62].

The k-rank of a matrix  $\mathbf{A}$ , denoted  $\text{krank}(A)$ , is the maximum number  $k$  such that every set of  $k$  columns of  $\mathbf{A}$  is linearly independent. One can see that the k-rank  $\text{krank}(A)$  is always less than or equal to the rank of  $\mathbf{A}$ , that is:

$$\text{krank}(A) \leq \text{rank}(A) \leq \min(I_1, R). \quad (4.18)$$

Let us consider the set of factor matrices  $\mathbf{A}$ ,  $\mathbf{B}$  and  $\mathbf{C}$ , previous defined in Equation (4.9).  $\mathbf{A}$ ,  $\mathbf{B}$ , and  $\mathbf{C}$  are unique up to permutation and scaling factors if [58]:

$$\text{krank}(A) + \text{krank}(B) + \text{krank}(C) \geq 2R + 2. \quad (4.19)$$

That is, if (4.19) holds, any matrices  $\tilde{\mathbf{A}}$ ,  $\tilde{\mathbf{B}}$ , and  $\tilde{\mathbf{C}}$  that satisfy (4.9) are connected to  $\mathbf{A}$ ,  $\mathbf{B}$ , and  $\mathbf{C}$  as:

$$\tilde{\mathbf{A}} = \mathbf{A}\boldsymbol{\Pi}\boldsymbol{\Delta}_A \quad (4.20)$$

$$\tilde{\mathbf{B}} = \mathbf{B}\boldsymbol{\Pi}\boldsymbol{\Delta}_B \quad (4.21)$$

$$\tilde{\mathbf{C}} = \mathbf{C}\boldsymbol{\Pi}\boldsymbol{\Delta}_C, \quad (4.22)$$

where  $\boldsymbol{\Pi}$  is a permutation matrix and  $\boldsymbol{\Delta}_A$ ,  $\boldsymbol{\Delta}_B$ , and  $\boldsymbol{\Delta}_C$  are diagonal matrices such that:

$$\boldsymbol{\Delta}_A \boldsymbol{\Delta}_B \boldsymbol{\Delta}_C = \mathbf{I}_R . \quad (4.23)$$

Condition (4.19) is the most general condition to assure the uniqueness of a PARAFAC decomposition, being sufficient, but not necessary. Other more relaxed sufficient conditions have been proposed through the years to assure the uniqueness of some specific PARAFAC decompositions. In [99, Theorem 4.6], for example, it is shown that if  $\mathbf{C}$  is known,  $\mathbf{B}$  has full-column rank, and:

$$\text{rank}([\mathbf{C} \diamond \mathbf{A}, \mathbf{c}_r \otimes \mathbf{I}_{I_1}]) = I_1 + R - 1, \forall r \in 1, \dots, R , \quad (4.24)$$

then the PARAFAC decomposition is unique. Generically, the above conditions hold if:

$$\min((I_3 - 1)I_1 + 1, I_2) \geq R . \quad (4.25)$$

A variant of the PARAFAC model, called nested PARAFAC model, was proposed in [19] and it corresponds to two nested third-order PARAFAC models sharing a common matrix factor. Let us consider an arbitrary fourth-order tensor  $\mathcal{X} \in \mathbb{C}^{I_1 \times I_2 \times I_3 \times I_4}$ , its Nested PARAFAC decomposition can be written in scalar form as:

$$x_{i_1, i_2, i_3, i_4} = \sum_{r_1=1}^{R_1} \sum_{r_2=1}^{R_2} a_{i_1, r_1}^{(1)} b_{i_2, r_1}^{(1)} a_{i_3, r_2}^{(2)} b_{i_4, r_2}^{(2)} g_{r_1, r_2} , \quad (4.26)$$

where  $a_{i_1, r_1}^{(1)}$ ,  $b_{i_2, r_1}^{(1)}$ ,  $a_{i_3, r_2}^{(2)}$ ,  $b_{i_4, r_2}^{(2)}$ , and  $g_{r_1, r_2}$  are the scalar components of the matrices  $\mathbf{A}^{(1)} \in \mathbb{C}^{I_1 \times R_1}$ ,  $\mathbf{B}^{(1)} \in \mathbb{C}^{I_2 \times R_1}$ ,  $\mathbf{A}^{(2)} \in \mathbb{C}^{I_3 \times R_2}$ ,  $\mathbf{B}^{(2)} \in \mathbb{C}^{I_4 \times R_2}$ , and  $\mathbf{G} \in \mathbb{C}^{R_1 \times R_2}$ , respectively.

The PARAFAC decomposition and its variants have proven useful in several research fields, such as chemometrics [7], neuroscience [80], psychometrics [9], signal processing [94], and many others.

### 4.3.2 Tucker-3 decomposition

The Tucker-3 decomposition [103] was proposed in 1966 by Ledyard R. Tucker. This tensor decomposition represents a tensor  $\mathcal{X} \in \mathbb{C}^{I_1 \times I_2 \times I_3}$  in scalar form as:

$$x_{i_1, i_2, i_3} = \sum_{p=1}^P \sum_{q=1}^Q \sum_{r=1}^R a_{i_1, p} b_{i_2, q} c_{i_3, r} g_{p, q, r} , \quad (4.27)$$

where  $a_{i_1, p}$ ,  $b_{i_2, q}$  and  $c_{i_3, r}$  are the scalar components of the matrices  $\mathbf{A}^{I_1 \times P}$ ,  $\mathbf{B}^{I_2 \times Q}$  and  $\mathbf{C}^{I_3 \times R}$ , respectively, and  $g_{p, q, r}$  is a scalar component of the so-called core tensor  $\mathcal{G} \in \mathbb{C}^{P \times Q \times R}$ .  $P$ ,  $Q$ , and  $R$  are the number of factors in the first, second, and third mode of the tensor. Figure 4.4 illustrates this tensor decomposition for an arbitrary third-order tensor  $\mathcal{X}$ . Tucker decomposition is an extension of CPD, allowing for interactions between vector factors with different indices. Indeed, a Tucker decomposition with identity core tensor is equivalent to a CPD.

One can see that the Tucker-3 decomposition is not unique, since there exists infinite solutions for the core tensor and the factor matrices that lead to the same tensor  $\mathcal{X}$ .

There exist two special cases of the Tucker decomposition known as Tucker-2 and Tucker-1 decompositions. Considering the Tucker-3 decomposition in (4.27), one can rewrite this equation as:

$$x_{i_1, i_2, i_3} = \sum_{p=1}^P \sum_{q=1}^Q a_{i_1, p} b_{i_2, q} \left( \sum_{r=1}^R c_{i_3, r} g_{p, q, r} \right) = \sum_{p=1}^P \sum_{q=1}^Q a_{i_1, p} b_{i_2, q} h_{p, q, i_3} . \quad (4.28)$$

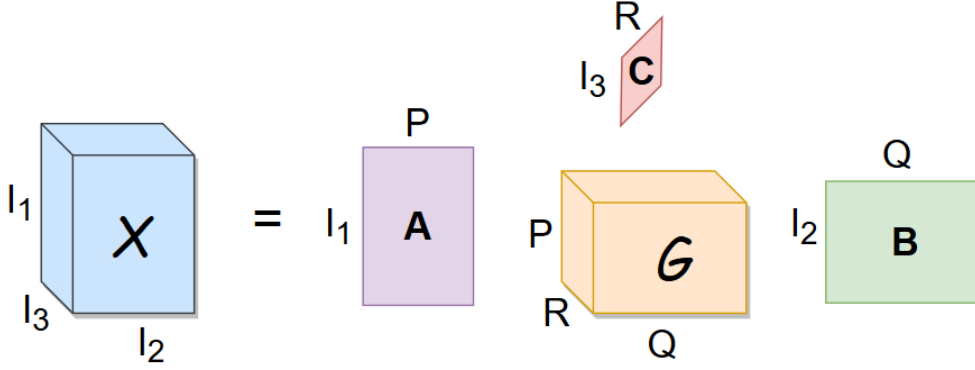


Figure 4.4: Illustration of the Tucker-3 decomposition of a third-order tensor.

One can see that (4.28) is the scalar form of the Tucker-2 decomposition, where  $c_{i_3,r}$  and  $g_{p,q,r}$  form the equivalent core tensor  $h_{p,q,i_3}$ .

Equation (4.27) can also be rewritten as:

$$x_{i_1,i_2,i_3} = \sum_{p=1}^P a_{i_1,p} \left( \sum_{q=1}^Q \sum_{r=1}^R b_{i_2,q} c_{i_3,r} g_{p,q,r} \right) = \sum_{p=1}^P a_{i_1,p} f_{p,i_2,i_3}. \quad (4.29)$$

Equation (4.29) is the scalar form of the Tucker-1 decomposition, where  $b_{i_2,q}$ ,  $c_{i_3,r}$ , and  $g_{p,q,r}$  form the equivalent core tensor  $f_{p,i_2,i_3}$ .

Generalizing to an arbitrary  $N^{\text{th}}$ -order tensor  $\mathcal{X} \in \mathbb{C}^{I_1 \times I_2 \times \dots \times I_N}$ , the  $N^{\text{th}}$ -order Tucker decomposition of this tensor is given by:

$$x_{i_1,i_2,\dots,i_N} = \sum_{r_1=1}^{R_1} \sum_{r_2=1}^{R_2} \dots \sum_{r_N=1}^{R_N} a_{i_1,r_1}^{(1)} a_{i_2,r_2}^{(2)} \dots a_{i_N,r_N}^{(N)} g_{r_1,r_2,\dots,r_N}, \quad (4.30)$$

where  $a_{i_n,r_n}$  is the scalar component of the matrix  $\mathbf{A}^{I_n \times R_n}$  and  $g_{r_1,r_2,\dots,r_N}$  is a scalar component of the  $N^{\text{th}}$ -order core tensor  $\mathcal{G} \in \mathbb{C}^{R_1 \times R_2 \times \dots \times R_N}$ .

A Tucker-based model was proposed in [36], called nested Tucker decomposition. This tensor factorization writes a fourth-order tensor  $\mathcal{X} \in \mathbb{C}^{I_1 \times I_2 \times I_3 \times I_4}$  in scalar form as:

$$x_{i_1,i_2,i_3,i_4} = \sum_{r_1=1}^{R_1} \sum_{r_2=1}^{R_2} \sum_{r_3=1}^{R_3} \sum_{r_4=1}^{R_4} a_{i_1,r_1} c_{r_1,i_2,r_2}^{(1)} r_{r_2,r_3} c_{r_3,i_3,r_4}^{(2)} b_{i_4,r_4}, \quad (4.31)$$

where  $a_{i_1,r_1}$ ,  $c_{r_1,i_2,r_2}^{(1)}$ ,  $r_{r_2,r_3}$ ,  $c_{r_3,i_3,r_4}^{(2)}$ , and  $b_{i_4,r_4}$  are the scalar components of  $\mathbf{A} \in \mathbb{C}^{I_1 \times R_1}$ ,  $\mathcal{C}^{(1)} \in \mathbb{C}^{R_1 \times I_2 \times R_2}$ ,  $\mathbf{R} \in \mathbb{C}^{R_2 \times R_3}$ ,  $\mathcal{C}^{(2)} \in \mathbb{C}^{R_3 \times I_3 \times R_4}$ , and  $\mathbf{B} \in \mathbb{C}^{I_4 \times R_4}$ , respectively.

Generalizing this decomposition for an arbitrary  $N^{\text{th}}$ -order tensor  $\mathcal{X} \in \mathbb{C}^{I_1 \times I_2 \times \dots \times I_N}$ , one can write its scalar form as:

$$x_{i_1,i_2,\dots,i_N} = \sum_{r_1=1}^{R_1} \sum_{r_2=1}^{R_2} \dots \sum_{r_N=1}^{R_N} a_{i_1,r_1}^{(1)} c_{r_1,i_2,r_2}^{(1)} a_{r_2,r_3}^{(2)} c_{r_3,i_3,r_4}^{(2)} \dots c_{r_{2N-5},i_{N-1},r_{2N-4}}^{(N-2)} a_{i_N,r_{2N-4}}^{(N-1)}, \quad (4.32)$$

where  $a_{i_1,r_1}^{(1)}$ ,  $a_{i_N,r_{2N-4}}^{(N-1)}$ ,  $a_{r_{2n},r_{2n+1}}^{(n+1)}$ , and  $c_{r_{2n-1},i_{n+1},r_{2n}}^{(n)}$  are the scalar components of  $\mathbf{A}^{(1)} \in \mathbb{C}^{I_1 \times R_1}$ ,  $\mathbf{A}^{(N-1)} \in \mathbb{C}^{I_N \times R_{2N-4}}$ ,  $\mathbf{A}^{(n+1)} \in \mathbb{C}^{R_{2n} \times R_{2n+1}}$ , and  $\mathcal{C}^{(n)} \in \mathbb{C}^{R_{2n-1} \times I_{n+1} \times R_{2n}}$ , respectively.

The Tucker decomposition has applications in research fields such as neuroscience [79], chemometrics [97], and others.

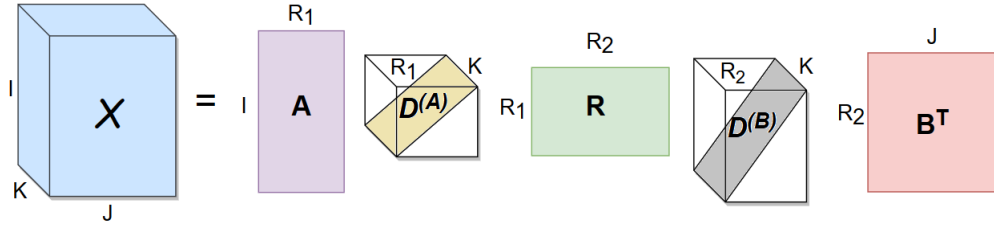


Figure 4.5: PARATUCK-2 decomposition of a third-order tensor.

### 4.3.3 PARATUCK decomposition

Once the PARAFAC and Tucker models have been presented, it is now presented a tensor model that shares some features of both models, i.e., this decomposition can be considered as a combination of PARAFAC and TUCKER-2 [58]. This tensor model called PARATUCK was proposed in 1996 by Richard A. Harshman & Margaret E. Lundy [46]. Consider an arbitrary third-order tensor  $\mathbf{X} \in \mathbb{C}^{I \times J \times K}$ , its PARATUCK-2 decomposition can be written in scalar form as:

$$x_{i,j,k} = \sum_{r_2=1}^{R_2} \sum_{r_1=1}^{R_1} a_{i,r_1} d_{k,r_1}^{(a)} r_{r_1,r_2} d_{k,r_2}^{(b)} b_{r_2,j}, \quad (4.33)$$

where  $a_{i,r_1}$ ,  $d_{k,r_1}^{(a)}$ ,  $r_{r_1,r_2}$ ,  $d_{k,r_2}^{(b)}$ , and  $b_{r_2,j}$  are the scalar components of the matrices  $\mathbf{A} \in \mathbb{C}^{I \times R_1}$ ,  $\mathbf{D}^{(A)} \in \mathbb{C}^{K \times R_1}$ ,  $\mathbf{R} \in \mathbb{C}^{R_1 \times R_2}$ ,  $\mathbf{D}^{(B)} \in \mathbb{C}^{K \times R_2}$ , and  $\mathbf{B}^T \in \mathbb{C}^{R_2 \times J}$ . This tensor decomposition is illustrated in Figure 4.5. We can also express the PARATUCK-2 decomposition in matrix slices terms as:

$$\mathbf{X}_{..k} = \mathbf{A} D_k(\mathbf{D}^{(A)}) \mathbf{R} D_k(\mathbf{D}^{(B)}) \mathbf{B}^T. \quad (4.34)$$

Generalizing, we can write the PARATUCK- $N$  decomposition of the same arbitrary third-order tensor in matrix slices terms as:

$$\mathbf{X}_{..k} = \mathbf{A}^{(N+1)} D_k(\mathbf{D}^{(N)}) \mathbf{A}^{(N)} \dots D_k(\mathbf{D}^{(2)}) \mathbf{A}^{(2)} D_k(\mathbf{D}^{(1)}) \mathbf{A}^{(1)T}. \quad (4.35)$$

In [22] it was shown that the PARATUCK- $N$  decompositon can alternatively be represented as a PARATUCK-2 model, with different sets of sufficient uniqueness conditions. Furthermore, in [46] it was proved the uniqueness for the general PARATUCK-2 model, considering  $\mathbf{D}^{(A)} = \mathbf{D}^{(B)}$ , and under the conditions that  $R_1 = R_2$  and  $\mathbf{R}$  has no zeros. In this case, [46] supposes that there is an alternative representation of  $\mathbf{X}_{..k}$  given by:

$$\mathbf{X}_{..k} = \tilde{\mathbf{A}} D_k(\tilde{\mathbf{D}}^{(A)}) \tilde{\mathbf{R}} D_k(\tilde{\mathbf{D}}^{(B)}) \tilde{\mathbf{B}}^T. \quad (4.36)$$

where  $\tilde{\mathbf{A}}$ ,  $\tilde{\mathbf{D}}^{(A)}$ ,  $\tilde{\mathbf{R}}$ ,  $\tilde{\mathbf{D}}^{(B)}$ , and  $\tilde{\mathbf{B}}^T$  have the same size and structural forms as their equivalent terms in (4.34).

The representations in (4.34) and (4.36) are related as

$$\tilde{\mathbf{A}}(\boldsymbol{\Pi}_A \boldsymbol{\Delta}_A) = \mathbf{A} \quad (4.37)$$

$$\tilde{\mathbf{B}}(\boldsymbol{\Pi}_B \boldsymbol{\Delta}_B) = \mathbf{B} \quad (4.38)$$

$$(\bar{\boldsymbol{\Delta}}_A \boldsymbol{\Delta}_A^{-1} \boldsymbol{\Pi}_A^T) \tilde{\mathbf{R}} (\boldsymbol{\Pi}_B \boldsymbol{\Delta}_B^{-1} \bar{\boldsymbol{\Delta}}_B) = \mathbf{R}, \quad (4.39)$$

and for any  $\mathbf{X}_{..k} \neq 0$ :

$$(z_k \boldsymbol{\Pi}_A^T) D_k(\tilde{\mathbf{D}}^{(A)}) (\boldsymbol{\Pi}_A \bar{\boldsymbol{\Delta}}_A^{-1}) = D_k(\mathbf{D}^{(A)}) \quad (4.40)$$

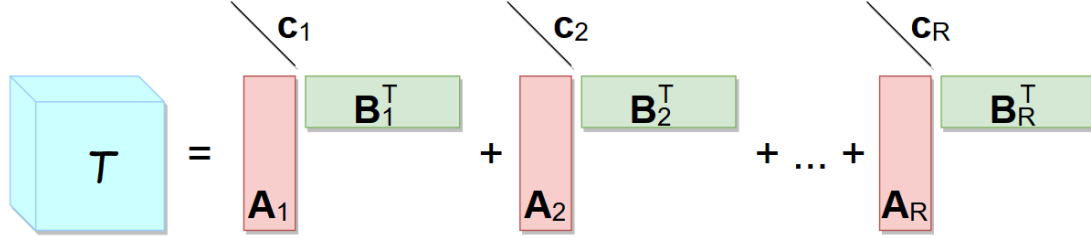


Figure 4.6: Visual representation of the block term decomposition of an arbitrary third-order tensor.

$$(z_k^{-1} \boldsymbol{\Pi}_B^T) D_k(\tilde{\mathbf{D}}^{(B)}) (\boldsymbol{\Pi}_B \bar{\Delta}_B^{-1}) = D_k(\mathbf{D}^{(B)}), \quad (4.41)$$

where  $\bar{\Delta}_A$ ,  $\bar{\Delta}_B$ ,  $\Delta_A$  and  $\Delta_B$  are diagonal matrices,  $\boldsymbol{\Pi}_A$  and  $\boldsymbol{\Pi}_B$  are permutation matrices, and  $z_k$  are nonzero scalars.

The PARATUCK decomposition is mainly applied in signal processing for communication systems [22], [32].

## 4.4 Block term decomposition

The block term decomposition (BTD) was introduced in [64] and factorizes an arbitrary third-order tensor  $\mathcal{T} \in \mathbb{R}^{I_1 \times I_2 \times I_3}$  in the form of:

$$\mathcal{T} = \sum_{r=1}^R \mathbf{E}_r \circ \mathbf{c}_r, \quad (4.42)$$

where  $\mathbf{c}_r \in \mathbb{R}^{I_3}$  is a nonzero vector and  $\mathbf{E}_r \in \mathbb{R}^{I_1 \times I_2}$  is a matrix that has rank  $L_r$  and therefore admits a factorization  $\mathbf{E}_r = \mathbf{A}_r \mathbf{B}_r^T$ , where  $\mathbf{A}_r \in \mathbb{R}^{I_1 \times L_r}$  and  $\mathbf{B}_r \in \mathbb{R}^{I_2 \times L_r}$  have full column rank  $L_r$ . Equation (4.42) may then be rewritten as:

$$\mathcal{T} = \sum_{r=1}^R (\mathbf{A}_r \mathbf{B}_r^T) \circ \mathbf{c}_r. \quad (4.43)$$

The visual representation of BTD as a sum of the outer product of its matrix and vector factors is shown in Figure 4.6. One can see that the BTD is a decomposition of  $\mathcal{T}$  in multilinear rank- $(L_r, L_r, 1)$  terms. The structure of matrices  $\mathbf{E}_r$  is the same as that of the mode-3 matrix slices of tensor  $\mathcal{T}$  and may vary depending on the nature of the signal to be decomposed. In the present doctoral thesis, two well-known structures are explored: the Hankel structure, that focus on separating exponential functions, and the Löwner structure, focusing on the separation of rational functions.

Several conditions that guarantee the essential uniqueness of this decomposition are presented in [64], and further results were provided in [65]. For example, in [65, Theorem 2.2], it is shown that the BTD is essentially unique if the following sufficient conditions are satisfied:

1. The matrix factors  $\mathbf{A} = [\mathbf{A}_1 \ \mathbf{A}_2 \ \dots \ \mathbf{A}_R] \in \mathbb{R}^{I_1 \times \sum_{r=1}^R L_r}$  and  $\mathbf{B} = [\mathbf{B}_1 \ \mathbf{B}_2 \ \dots \ \mathbf{B}_R] \in \mathbb{R}^{I_2 \times \sum_{r=1}^R L_r}$  are full-column rank. This condition requires that  $\sum_{r=1}^R L_r \leq I_1, I_2$ .
2. Matrix  $\mathbf{C} = [\mathbf{c}_1 \ \mathbf{c}_2 \ \dots \ \mathbf{c}_R] \in \mathbb{R}^{I_3 \times R}$  does not contain proportional columns.

Essential uniqueness means that the decomposition is subject only to the following indeterminacies [64]:

1. The different multilinear rank- $(L_r, L_r, 1)$  terms can be arbitrarily permuted.
2.  $\mathbf{A}_r$  can be postmultiplied by any nonsingular matrix, given that  $\mathbf{B}_r$  is premultiplied by the inverse of that nonsingular matrix.
3. As long as the resulting product remains the same, the factors of the same multilinear rank- $(L_r, L_r, 1)$  term can be arbitrarily scaled.

Considering the matrix factors  $\mathbf{A}$ ,  $\mathbf{B}$  and  $\mathbf{C}$ , previously defined, one can write the matrix unfoldings of  $\mathcal{T}$  as:

$$\mathbf{T}_1 = (\mathbf{B} \odot \mathbf{C})\mathbf{A}^T \in \mathbb{C}^{I_2 I_3 \times I_1} \quad (4.44)$$

$$\mathbf{T}_2 = (\mathbf{C} \odot \mathbf{A})\mathbf{B}^T \in \mathbb{C}^{I_3 I_1 \times I_2} \quad (4.45)$$

$$\mathbf{T}_3 = [(\mathbf{A}_1 \diamond \mathbf{B}_1)\mathbf{1}_{L_1} \dots (\mathbf{A}_R \diamond \mathbf{B}_R)\mathbf{1}_{L_R}] \mathbf{C}^T \in \mathbb{C}^{I_1 I_2 \times I_3}. \quad (4.46)$$

Expressions for the matrix slices of  $\mathcal{T}$  can be given by:

$$\mathbf{T}_{i1..} = \text{Bbdiag}([(A_1)_{i11} \dots (A_1)_{i1L_1}]^T, \dots, [(A_R)_{i11} \dots (A_R)_{i1L_R}]^T) \mathbf{C}^T \in \mathbb{C}^{I_2 \times I_3} \quad (4.47)$$

$$\mathbf{T}_{.i2..} = \text{Cbdig}([(B_1)_{i21} \dots (B_1)_{i2L_1}], \dots, [(B_R)_{i21} \dots (B_R)_{i2L_R}]) \mathbf{A}^T \in \mathbb{C}^{I_3 \times I_1} \quad (4.48)$$

$$\mathbf{T}_{..i3} = \text{Abdiag}(c_{i31}\mathbf{I}_{L_1}, \dots, c_{i3R}\mathbf{I}_{L_R}) \mathbf{B}^T \in \mathbb{C}^{I_1 \times I_2}. \quad (4.49)$$

## 4.5 Coupled block term decomposition

Considering a set of BTD tensors  $\mathcal{T}^{(n)} \in \mathbb{R}^{I_n \times J_n \times K}$ , for  $n = 1, \dots, N$ , with matrix factors  $\mathbf{A}_{r,n} \mathbf{B}_{r,n}^T$  that have rank  $L_{r,n}$  and a common vector factor  $\mathbf{c}_r$ , the coupled BTDs of  $\mathcal{T}^{(n)}$ , can be written in the following form [98]:

$$\mathcal{T}^{(n)} = \sum_{r=1}^R (\mathbf{A}_{r,n} \mathbf{B}_{r,n}^T) \circ \mathbf{c}_r. \quad (4.50)$$

Considering mode-1 matrix unfoldings, a matrix representation of the overall coupled BTD can be given by:

$$\mathbf{T} = [(\mathbf{T}_1^{(1)})^T, \dots, (\mathbf{T}_1^{(N)})^T]^T = \mathbf{F} \mathbf{C}^T \in \mathbb{R}^{(\sum_{n=1}^N I_n J_n) \times K} \quad (4.51)$$

where  $\mathbf{T}_1^{(n)}$  is the mode-1 matrix unfolding of  $\mathcal{T}^{(n)}$ , for  $n = 1, \dots, N$ ,  $\mathbf{C} = [\mathbf{c}_1, \dots, \mathbf{c}_R] \in \mathbb{R}^{K \times R}$ , and  $\mathbf{F} \in \mathbb{R}^{(\sum_{n=1}^N I_n J_n) \times R}$  is given by:

$$\mathbf{F} = \begin{bmatrix} \text{vec}(\mathbf{B}_{1,1} \mathbf{A}_{1,1}^T) & \dots & \text{vec}(\mathbf{B}_{R,1} \mathbf{A}_{R,1}^T) \\ \vdots & \ddots & \vdots \\ \text{vec}(\mathbf{B}_{1,N} \mathbf{A}_{1,N}^T) & \dots & \text{vec}(\mathbf{B}_{R,N} \mathbf{A}_{R,N}^T) \end{bmatrix}. \quad (4.52)$$

The coupled BTDs in (4.50) are illustrated in Figure 4.7 and can be arbitrarily permuted. Also, the matrix and vector factors of the same coupled multilinear rank- $(L_{r,n}, L_{r,n}, 1)$  tensor can be arbitrarily scaled, as long as the overall coupled multilinear rank- $(L_{r,n}, L_{r,n}, 1)$  term remains the same [98]. Uniqueness conditions for the overall coupled BTD tensor with  $\mathbf{c}_r$  as a common factor are presented in [98]. For example, consider  $\hat{\mathbf{A}}_{r,n}$ ,  $\hat{\mathbf{B}}_{r,n}^T$  and  $\hat{\mathbf{c}}_r$  the matrix and vector factors that form an alternative coupled

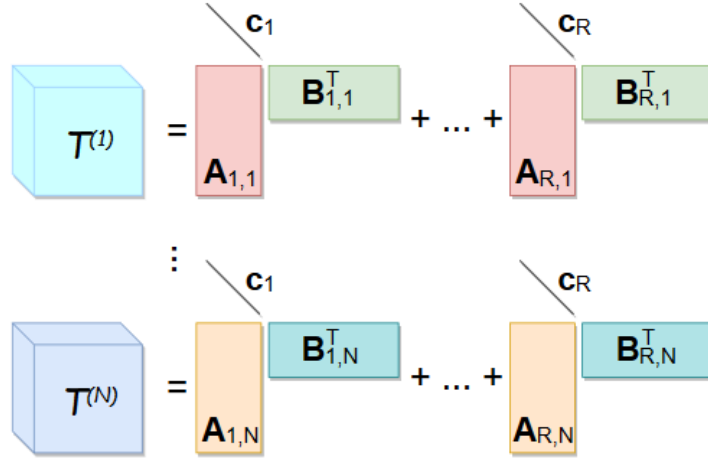


Figure 4.7: Visual representation of coupled BTDs of arbitrary third-order tensors with common factor  $\mathbf{c}_r$ , for  $r = 1, 2, \dots, R$ .

BTD of the tensors  $\mathcal{T}^{(n)}$  in Equation (4.50). The coupled BTD of tensors  $\mathcal{T}^{(n)}$  is unique up to a permutation of the coupled multilinear rank- $(L_{r,n}, L_{r,n}, 1)$  terms and up to the following indeterminacies in each term:

$$\begin{aligned}\hat{\mathbf{A}}_{r,n} &= \alpha_{r,n} \mathbf{A}_{r,n} \mathbf{H}_{r,n} \\ \hat{\mathbf{B}}_{r,n} &= \beta_{r,n} \mathbf{B}_{r,n} \mathbf{H}_{r,n}^{-1} \\ \hat{\mathbf{c}}_r &= \gamma_r \mathbf{c}_r ,\end{aligned}$$

where  $\mathbf{H}_{r,n}$  are nonsingular matrices and  $\alpha_{r,n}$ ,  $\beta_{r,n}$  and  $\gamma_r$  are scalar factors with unitary product, i.e.,  $\alpha_{r,n} \beta_{r,n} \gamma_r = 1$ .

Also, from Equation (4.51), one can see that two necessary conditions for the uniqueness of the coupled BTD of (4.50) are:

1.  $\text{krank}(\mathbf{C}) \geq 2$ , where  $\mathbf{C} = [\mathbf{c}_1, \dots, \mathbf{c}_R]$ .
2. Matrix  $\mathbf{F}$  has full column rank.

## 4.6 Hankel-BTD as an AA extraction tool

In [65], the Hankel-BTD is proposed as a solution of a BSS problem like (3.19). The idea to obtain a tensor from  $\mathbf{Y}$  is to map each of its  $k^{\text{th}}$  row onto a Hankel matrix  $\mathbf{H}_{\mathbf{Y}}^{(k)} \in \mathbb{R}^{I \times J}$ , where  $I = J = \frac{N+1}{2}$  if  $N$  is odd or  $I = \frac{N}{2}$  and  $J = \frac{N}{2} + 1$  if  $N$  is even, with:

$$[\mathbf{H}_{\mathbf{Y}}^{(k)}]_{i,j} \triangleq y_{k,i+j-1} , \quad (4.53)$$

where  $i = 1, \dots, I$ ,  $j = 1, \dots, J$ , and  $k = 1, \dots, K$ . This process is called hankelization. Next, the tensor is built by stacking each Hankel matrix along the third-mode (as frontal slices) of a third-order tensor  $\mathcal{Y} \in \mathbb{R}^{I \times J \times K}$ , that is:

$$\mathbf{Y}_{..k} = \mathbf{H}_{\mathbf{Y}}^{(k)} . \quad (4.54)$$

In scalar form, the third-order tensor  $\mathcal{Y}$  can be written as:

$$y_{i,j,k} = \sum_{r=1}^R m_{k,r} s_{r,i+j-1} . \quad (4.55)$$

The  $k^{\text{th}}$  matrix slice of this tensor can be represented as:

$$\mathbf{Y}_{..k} = \sum_{r=1}^R m_{k,r} \mathbf{H}_{\mathbf{S}}^{(r)}, \quad (4.56)$$

where  $\mathbf{H}_{\mathbf{S}}^{(r)} \in \mathbb{R}^{I \times J}$  is a Hankel matrix built from the  $r^{\text{th}}$  row of  $\mathbf{S}$ . One can see that for each  $r$ , the outer product between matrix  $\mathbf{H}_{\mathbf{S}}^{(r)}$  and the  $r^{\text{th}}$  column of  $\mathbf{M}$ , i.e.,  $\mathbf{m}_{.r}$ , is being performed to obtain the contribution of each source to the observed tensor. This way, the third-order tensor  $\mathcal{Y}$  can be written as

$$\mathcal{Y} = \sum_{r=1}^R \mathbf{H}_{\mathbf{S}}^{(r)} \circ \mathbf{m}_{.r}. \quad (4.57)$$

Considering  $\mathbf{Y}$  as an ECG data matrix, where each row represents a lead, and comparing Equations (4.42) and (4.57), it can be concluded that the ECG data tensor obtained by hankelization follows a BTD tensor model with the following correspondence:

$$(\mathcal{T}) \iff (\mathcal{Y}) \quad (4.58)$$

$$(\mathbf{E}_r, \mathbf{c}_r) \iff (\mathbf{H}_{\mathbf{S}}^{(r)}, \mathbf{m}_{.r}) \quad (4.59)$$

$$(I_1, I_2, I_3, R) \iff (I, J, K, R). \quad (4.60)$$

Recalling the two sufficient uniqueness conditions for BTD in Section 4.4, for ECG signal processing, sufficiently long segments directly imply that  $I, J \approx \frac{N+1}{2} \geq \sum_{r=1}^R L_r$ . Also, matrix  $\mathbf{C}$  corresponds to the mixing matrix  $\mathbf{M}$ , whose columns represent the contribution of each source to the ECG leads, which are not proportional.

The Hankel-BTD suits the characteristics of AA in AF episodes, since atrial signals can be approximated by all-pole (or exponential) models and mapped onto Hankel matrices with rank equal to the number of poles [110]. Indeed, due to the quasi-periodic nature of AF signals, atrial sources can be represented by the all-pole (exponential) model:

$$s_{r,n} = \sum_{\ell=1}^{L_r} \lambda_{\ell,r} z_{\ell,r}^{n-1}, \quad (4.61)$$

where  $n = 1, \dots, N$  represents the discrete-time index,  $r = 1, \dots, R$ ,  $L_r$  is the number of exponential terms,  $z_{\ell,r}$  is the  $\ell^{\text{th}}$  pole of the  $r^{\text{th}}$  source, and  $\lambda_{\ell,r}$  is the scaling coefficient. This way, their associated Hankel matrices accept the Vandermonde decomposition [5]:

$$\mathbf{H}_{\mathbf{S}}^{(r)} = \mathbf{V}_r \text{diag}(\lambda_{1,r}, \lambda_{2,r}, \dots, \lambda_{L_r,r}) \hat{\mathbf{V}}_r^T, \quad (4.62)$$

with

$$\mathbf{V}_r = \begin{bmatrix} 1 & 1 & \dots & 1 \\ z_{1,r} & z_{2,r} & \dots & z_{L_r,r} \\ \vdots & \vdots & \ddots & \vdots \\ z_{1,r}^{I-1} & z_{2,r}^{I-1} & \dots & z_{L_r,r}^{I-1} \end{bmatrix} \in \mathbb{R}^{I \times L_r} \quad (4.63)$$

and

$$\hat{\mathbf{V}}_r = \begin{bmatrix} 1 & 1 & \dots & 1 \\ z_{1,r} & z_{2,r} & \dots & z_{L_r,r} \\ \vdots & \vdots & \ddots & \vdots \\ z_{1,r}^{J-1} & z_{2,r}^{J-1} & \dots & z_{L_r,r}^{J-1} \end{bmatrix} \in \mathbb{R}^{J \times L_r}. \quad (4.64)$$

In the case of different poles, the Vandermonde matrix with  $L_r \leq I, J$  will have full-column rank  $L_r$ , so if  $\mathbf{M}$  does not have proportional columns, the BTD in (4.57) will be essentially unique. In the case of equal poles, milder conditions can assure the uniqueness of (4.57) [65].

The Hankel-BTD was introduced as an AA extraction tool from AF ECGs in [87], outperforming the BSS matrix-based approaches regarding AA extraction in fixed short AF ECG recordings of a single patient suffering from persistent AF. However, no major conclusions can be drawn, as the performance analysis carried out in [87] is rather limited, where experiments were performed only in synthetic signals and in a single patient.

In order to overcome this limitation, the first goal of this doctoral thesis is to validate the Hankel-BTD in a population of patients and in a whole ECG recording, by performing more thorough experimental analysis. As mentioned earlier in Chapter 1, other challenging issues are also addressed in this doctoral thesis, such as the problem of AA source classification and quantification, alternative tensor models to perform AA extraction in difficult AF ECG recordings, the impact of BTD initialization and model parameters on AA extraction performance, the use of improved algorithms for BTD computation, etc.

## 4.7 Summary

This chapter summarized the tensor algebra fundamentals, necessary to understand the mathematical part of this doctoral thesis. First, basic concepts of multilinear algebra were introduced, followed by the main tensor decompositions and their applications. Among the existing tensor decompositions, the Hankel-BTD was identified as particularly suitable for noninvasive AA extraction in AF episodes, although some limitations were remarked that this work aims to overcome. The next part of this manuscript contains the contributions of the present doctoral thesis.



## Part II

# Contributions



## CHAPTER 5

# Quantification of AA Content and Source Classification

---

## Contents

---

<b>5.1</b>	<b>Introduction</b>	<b>47</b>
<b>5.2</b>	<b>Indices for AA quantification</b>	<b>48</b>
<b>5.3</b>	<b>Automated methods for source classification</b>	<b>50</b>
5.3.1	Classical method	50
5.3.2	Proposed method 1	50
5.3.3	Proposed method 2	51
5.3.4	Experimental data and setup	51
5.3.5	Source analysis and classification	52
<b>5.4</b>	<b>Machine learning approach for source classification</b>	<b>53</b>
5.4.1	Methods	54
5.4.2	Experimental data and setup	55
5.4.3	Classification	55
<b>5.5</b>	<b>Neural networks approach for source classification</b>	<b>57</b>
5.5.1	Data augmentation	58
5.5.2	Convolutional neural networks	58
5.5.3	Architecture optimization	59
5.5.4	Model training and evaluation	59
5.5.5	Experimental results	59
<b>5.6</b>	<b>Summary</b>	<b>60</b>

---

## 5.1 Introduction

This chapter is an important previous step before presenting the experimental evaluation of the BSS techniques studied in this doctoral thesis, as it presents the proposed AA quantification indices used in the following chapters. The contributions presented next start with the proposition of new indices to quantify the quality of the AA extraction after performing BSS. Later, the problem of automatically detecting the AA source among the other estimated sources is dealt with automated methods and two artificial intelligence approaches: machine learning and neural networks. This chapter provided the following publications:

- I. N. Lira, P. M. R. de Oliveira, W. Freitas Jr and V. Zarzoso, “Automated atrial fibrillation source detection using shallow convolutional neural networks”, to appear in Proc. *CinC-2020, Computing in Cardiology 2020*, Rimini, Italy, Sep. 13-16, 2020.

- P. M. R. de Oliveira, V. Zarzoso and C. A. R. Fernandes, “Source classification in atrial fibrillation using a machine learning approach”, in *Proc. CinC-2019, Computing in Cardiology 2019*, Biopolis, Singapore, Sep. 8-11, pp. 1-4, 2019.
- P. M. R. de Oliveira and V. Zarzoso, “Source analysis and selection using block term decomposition in atrial fibrillation”, in *Proc. LVA/ICA-2018, 14th International Conference on Latent Variable Analysis and Signal Separation*, Guildford, United Kingdom, Jul. 2-6, pp. 46-56, 2018.

## 5.2 Indices for AA quantification

Signal processing techniques used to solve BSS problems separate the observed signal in several sources. In AF ECGs, typically at least one of these sources contains the AA. It is still unknown if the AA is concentrated only in a single source. However, in the present doctoral thesis, as in previous works, it is considered that the AA is concentrated only in one source, and the source with the most significant AA content is called the atrial source.

Measuring the quality of the estimation or the AA content of real signals is a challenging task. Since there is no ground truth for comparison, one needs to take advantage of some features present in AA during AF. For example, in the frequency domain, the AA during AF has a peak between 3 and 9 Hz, as illustrated in Figures 5.3, 5.4 and 5.5. The position of this peak is called dominant frequency (DF). As in [24], it is defined as *potential atrial source* any source with DF in such an interval. However, a spectral peak in this interval may not be necessarily associated with an atrial component. A well-known index for AA content measurement is the spectral concentration (SC), that is, the relative amount of energy around the DF. The SC is computed as in [10]:

$$SC = \frac{\sum_{f_i=0.82f_p}^{1.17f_p} P_S(f_i)}{\sum_{f_i=0}^{F_s/2} P_S(f_i)} \quad (5.1)$$

where  $f_p$  is the value of the DF,  $F_s$  is the sampling frequency,  $f_i$  is the frequency value and  $P_S$  is the power spectrum of the source signal computed using Welch’s method as in [10]. The Welch’s method basically consists in splitting the signal into overlapping segments and windowing them before applying the discrete Fourier transform (DFT). Then, the average of the periodograms is computed, resulting in a smoother signal in the frequency domain [107].

However, one can see in (5.1) that the SC depends on the DF and the definition of a suitable interval for interpretation. Aiming to overcome this dependency, the kurtosis, denoted  $\kappa$ , of the signal in the frequency domain acquired by a 4096-point fast Fourier transform (FFT) is proposed as an AA quality index for AF [24]. As in [112], the general expression of kurtosis valid for non-circular complex data is used, given by:

$$\kappa = \frac{E[|S_r|^4] - 2E[|S_r|^2]^2 - |E[|S_r|^2]|^2}{E[|S_r|^2]^2} \quad (5.2)$$

where  $S_r$  is the FFT of the  $r^{\text{th}}$  source. It is known that AA in AF is typically a quasi-harmonic signal, characterized by a sparse frequency spectrum with few values significantly different from zero. Also, kurtosis is a measure of peakedness and sparsity of a distribution and, when computed in the frequency domain, it naturally provides a quantitative measure of harmonicity of the signal. A high kurtosis in the frequency domain

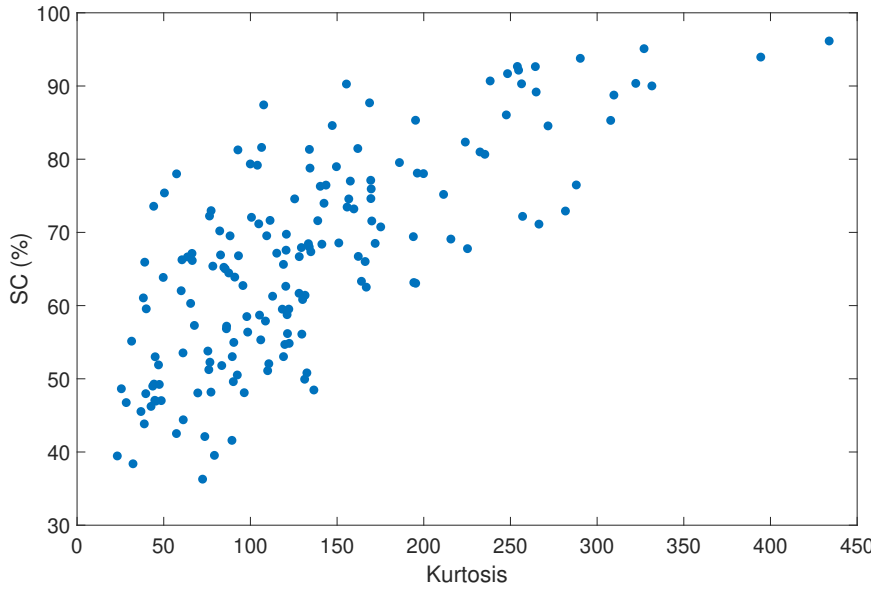


Figure 5.1: Scatter plot showing the correlation between kurtosis and SC of the selected atrial source by the Hankel-based BTD, for an observed population of 20 AF patients. A positive correlation can be seen.

means that the power spectral density is sparse, which is suggestive of a quasi-harmonic signal like AA in AF. In addition, kurtosis is parameter free, not depending on the DF and the definition of a suitable interval for interpretation [26].

In Figure 5.1 it can be seen how kurtosis and SC of the estimated atrial sources, by the Hankel-based BTD, are correlated across an observed population of 20 AF patients [26]. It is observed that these parameters are positively correlated, since in general, as long as the values of kurtosis increase, the values of SC also increase. Moreover, it is valid to point that, in the observed population, for high values of kurtosis we will always have high values of SC. However, for some patients it is observed a high value of SC but a low value of kurtosis, as shown in Figure 5.1.

A second index is put forward, to discard sources with irrelevant content that can be mistaken as the atrial source. The power contribution to lead V1, denoted  $P(r)$ , is given by [24]:

$$P(r) = \frac{1}{N} \|m_r^{(V1)} s_r\|^2 \quad (5.3)$$

in  $\text{mV}^2$ , where  $m_r^{(V1)}$  is the contribution of the  $r^{\text{th}}$  source to lead V1 (given by the corresponding element of the estimated mixing matrix) and  $s_r$  is the  $r^{\text{th}}$  source in time domain, corresponding to the  $r^{\text{th}}$  row of the source matrix  $\mathbf{S}$  in (3.19). The power contribution to lead V1 by an AA source is expected to be relatively strong ( $> 10^{-4} \text{ mV}^2$ , based on previous experiments), since this lead is the one that typically best reflects AA in AF ECGs. Indeed, lead V1 strongly correlates with the AA from the right atrium and moderately correlates with the AA from the left atrium [86].

Finally, taking advantage of the TQ segment in AF ECGs, where only the AA is observed, an additional AA estimation quality index is proposed: the normalized mean square error (NMSE) between the TQ segment of the original AF ECG recording and

the estimated source. This index is denoted NMSE-TQ and is given by [28]:

$$\text{NMSE-TQ} = \left[ \frac{\|m_r^{(V1)} \mathbf{s}_r - \mathbf{y}^{(V1)}\|_F^2}{\|\mathbf{y}^{(V1)}\|_F^2} \right]_{TQ} \quad (5.4)$$

where  $m_r^{(V1)}$  is the contribution of the  $r$ th source estimate to lead V1,  $\mathbf{s}_r$  is the  $r$ th source estimate and  $\mathbf{y}^{(V1)}$  is the original recording on lead V1. Note that lead V1 is also chosen as reference for this parameter, for the same reason previously explained.

## 5.3 Automated methods for source classification

### 5.3.1 Classical method

To select the estimated source with the most significant AA activity, the classical method considers two parameters: DF and SC. It makes the assumption that the atrial source is concentrated in a single source only. This method consists of the following steps [110], [111], [39]:

1. Select all the estimated sources with DF between 3 and 9 Hz, these signals are referred as potential atrial sources.
2. Select the potential atrial source with the highest SC.

### 5.3.2 Proposed method 1

In the literature, the classical automated method described above has been used to detect the atrial source among the other estimated sources. However, in some cases, this method may not precisely select the atrial source, as will be illustrated later in this work. In Figures 5.4 and 5.5, for example, the atrial source does not correspond to the potential source with the highest SC, despite the fact that they have close values of SC at very close DF positions.

Aiming at a higher accuracy in the selection of the AA signal, it is proposed to eliminate the weak sources that can be mistaken as the atrial source. Using the power contribution to the lead V1 as a new parameter, the classical method becomes:

1. Select all the estimated sources with DF between 3 and 9 Hz (potential atrial sources).
2. Select all the potential atrial sources with power contribution higher than  $10^{-4}$  mV<sup>2</sup>. We refer to this subset of sources as *likely atrial sources*.
3. Select the likely atrial source with the highest SC.

Selecting the sources with power contribution higher than  $10^{-4}$  mV<sup>2</sup> is needed in order to eliminate all sources that may present AA-like signature but are actually too weak to represent meaningful AA components. This threshold is chosen based on initial experiments that showed that sources with power contribution lower than  $10^{-4}$  mV<sup>2</sup> do not present any significant contribution to the original signal.

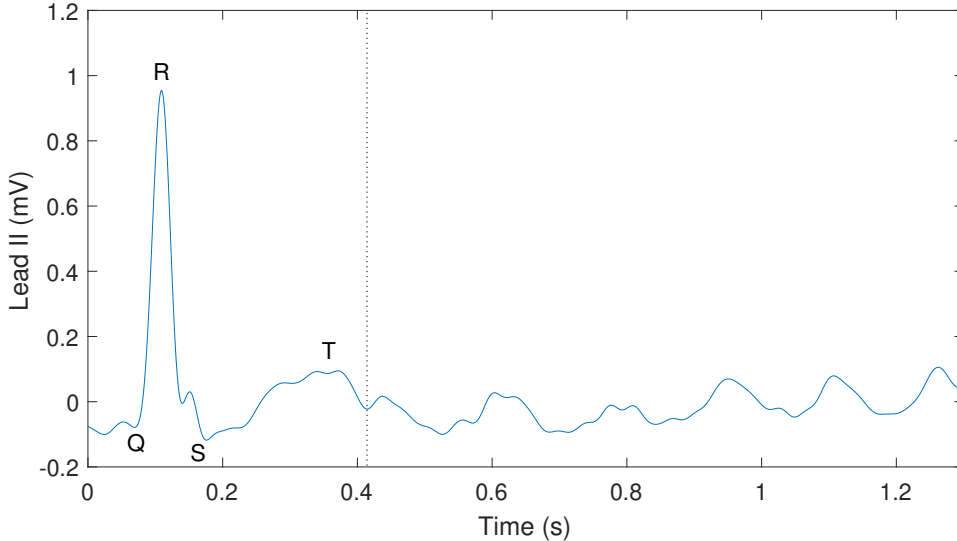


Figure 5.2: A single-beat segment of an AF ECG recording of one patient in lead II. The vertical line marks the location of the T-wave offset.

### 5.3.3 Proposed method 2

In order to better select the source with the most significant AA content among the other estimated sources, a new automated method is now proposed. The first two steps of this method are the same as those of the proposed method previously introduced. The third and last step of this new method is to select the source with the highest value of kurtosis in the frequency domain [24].

In the experiments below, it will be shown that selecting the source with the highest kurtosis provides a better performance than selecting the source with the highest SC. A possible explanation is that kurtosis is computed from the whole signal and does not require the estimation of the DF, while SC is only computed around the DF and require the prior estimation of this parameter.

### 5.3.4 Experimental data and setup

The reported experiments are divided in two parts: (i) potential atrial source detection and (ii) atrial source identification. The recordings used in those experiments belong to the PERSIST database, described in Section 1.3. To analyze the potential atrial sources, we consider a randomly selected heartbeat (QRST complex + TQ segment) of a standard 12-lead ECG recording from a single persistent AF patient. A single-beat segment of this patient is shown in Figure 5.2, where we can see the TQ interval just after the QRST complex in bipolar limb lead II. The beat from this patient used to analyze the potential atrial sources is chosen randomly and has 1300 samples.

To assess the atrial selection methods, a population of 10 patients suffering from persistent AF is used in the same way previously described. Similarly, one beat from each of the ten patients is chosen randomly to evaluate atrial source selection performance. The lengths of the chosen beats is between 1000 and 1400 samples (1.02 and 1.43 seconds, respectively). The physiological characteristics of the observed 10-patient population are described on Table 5.1. It must be reported that there are missing data values for one patient regarding AF history and LA diameter and such values were replaced by the average.

Table 5.1: Overall physiological characteristics of the 10-patient population.

Patient characteristics	$\mu \pm \sigma$	Min	Max
Age (years)	$65.4 \pm 8$	47	76
Height (cm)	$174.2 \pm 4.7$	169	185
Weight (kg)	$80.8 \pm 11.1$	64	103
AF History (months)	$85.8 \pm 67.8$	8	228
LA Diameter (mm)	$49 \pm 5.9$	36	56

The Hankel-BTD is implemented using the non-linear least squares (NLS) approach with the Gauss-Newton method available in Tensorlab MATLAB toolbox [105] choosing  $R = 12$  and  $L_r = 95$ , for  $r = 1, 2, \dots, 12$ . This choice is made based on the work [110], which showed that these values provided good results for the heartbeat with the largest TQ segment of one of the patients in the present observed population. The tolerance threshold for convergence is set to  $10^{-9}$  and the maximum number of iterations is set to 1000. The NLS method is known to be dependent on a suitable initialization of its factors. The experiments reported in this section evaluate the influence of Hankel-BTD factors initialization on source estimation performance and atrial source selection. Ten Monte Carlo runs, with normalized Gaussian random initialization for the matrix and vector factors at each run, are used to analyze the potential atrial sources found by Hankel-BTD and compare them with the ones found by the matrix-based methods PCA (Section 3.7.1) and RobustICA-f (Section 3.7.2). All the beats are downsampled by a factor of two, since the third-order tensor built from the original 12-lead ECG beat poses some computational difficulties to be processed by the Gauss-Newton algorithm for BTD computation.

### 5.3.5 Source analysis and classification

For the observed patient used to analyze the potential atrial sources, PCA found 6 potential sources, RobustICA-f found 5 potential sources and Hankel-BTD found a mean of 7.2 potential sources. In 7 out of the 10 independent runs, the Hankel-BTD found more potential sources than the matrix-based methods, reflecting the ability of the tensor technique to perform underdetermined source separation. Finding several potential atrial sources is interesting, since it increases the possibility of finding some features that, although weakly contributing to the AA, may provide useful physiological and clinical information about the arrhythmia. In this work, however, we assume as in the previous literature of this topic, that all AA can be represented by a single source. For the sake of clarity, only two potential atrial sources for PCA, RobustICA-f and Hankel-BTD are shown in Figures 5.3 – 5.5. The other sources were disregarded for presenting a very weak power contribution.

Looking at Figure 5.3, we can see that the atrial source estimated by PCA (located in the second row) has SC equal to 62.5%, while looking at Figure 5.4, the estimated atrial source by RobustICA-f (located in the second row) has SC equal to 68.3%. For Hankel-BTD, 8 out of the 10 independent runs estimated an atrial source with higher SC than PCA and 6 with higher SC than both matrix-based methods, giving an average SC over the 10 runs equal to 67.8%. Figure 5.5 shows the results for a particular initialization of Hankel-BTD, where the estimated atrial source (located in the second row) has SC equal to 76.5%. The DF position of both PCA and RobustICA-f are located at 5.96 Hz, while in Hankel-BTD it lies between 5.72 and 5.96 Hz. For comparison, the DF position

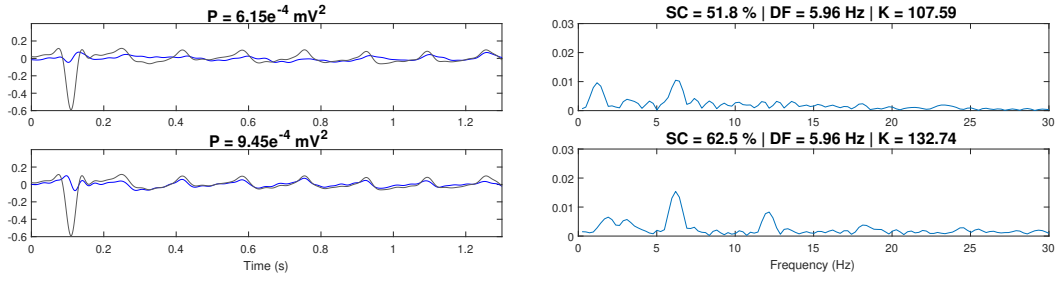


Figure 5.3: Potential atrial sources contribution to lead V1 estimated by PCA. Left: time domain (in mV). Right: frequency domain (in  $\text{mV}/\sqrt{\text{Hz}}$ ).

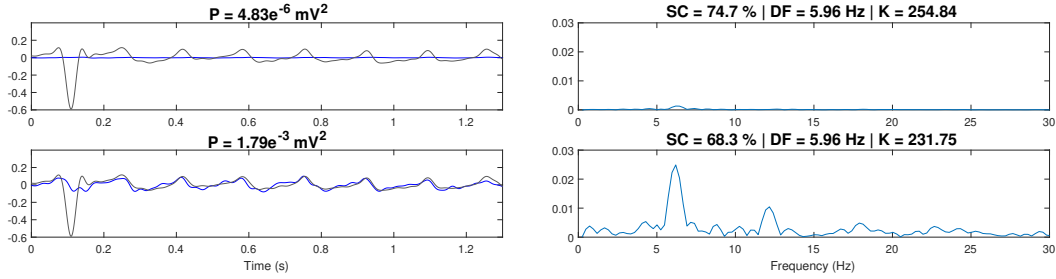


Figure 5.4: Potential atrial sources contribution to lead V1 estimated by RobustICA-f. Left: time domain (in mV). Right: frequency domain (in  $\text{mV}/\sqrt{\text{Hz}}$ ).

obtained from an electrogram simultaneously acquired by a catheter located in the left atrial appendage of the same patient, is 4.77 Hz.

As ground truth, the sources are visually analyzed in time and frequency domain with guidance of the indices previously described. The source with the strongest representation of AA content is taken as the atrial source.

The classical method and the two proposed methods of atrial source selection are assessed in 10 segments of 10 different patients, as previously explained. From a total of 120 runs for the 10 patients (100 for Hankel-BTD, 10 for PCA and 10 for RobustICA-f) the classical method succeeds only in 45.8% of runs. Applying the first proposed method (Section 5.3.2), the index of success increases to 75%, while the second proposed technique (Section 5.3.3) succeeds in 83.7% of the trials. It should be mentioned that in 35.8% of the trials, both the classical and the second proposed method are able to select the source with the strongest AA content. Also, in 12.5% of trials none of the methods are able to select the AA signal. This means that the existing methods are suboptimal regarding the AA source selection. However, from the reported experiments, it is believed that a balanced combination between power contribution and kurtosis may lead to an optimal or at least a better method.

## 5.4 Machine learning approach for source classification

Searching for a higher accuracy in classifying the AA source among the other estimated sources after BSS, this section presents a machine learning approach to perform this challenging task.

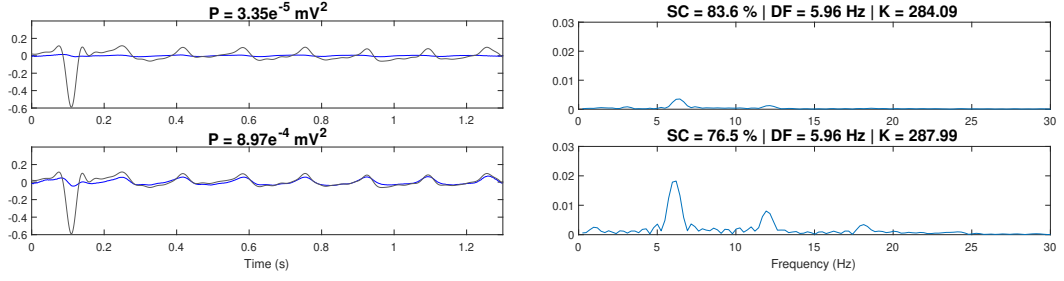


Figure 5.5: Potential atrial sources contribution to lead V1 estimated by Hankel-BTD for a single run. Left: time domain (in mV). Right: frequency domain (in  $\text{mV}/\sqrt{\text{Hz}}$ ).

#### 5.4.1 Methods

In these experiments, three different BSS methods are applied in different segments of ECG recordings from 30 different patients suffering from persistent AF, in order to compute an estimate of the sources that compose the original AF ECG: PCA, RobustICA-f and Hankel-BTD.

Classifiers are machine learning algorithms that operate on labeled data, predicting in which class (or category) the data belong to. Such algorithms are also defined as supervised learning models, as they need labeled data (training set) to learn and perform the classification of new data points (test set). Three well-known classifiers are used in these experiments to classify the source estimates provided by the BSS techniques, introduced in the previous section, into AA and non-AA sources: linear discriminant analysis (LDA) [37], quadratic discriminant analysis (QDA) [37], and support vector machine (SVM) [6]:

- **LDA:** commonly used for data classification and dimensionality reduction, LDA guarantees maximal separability with a linear decision region between the classes by computing discriminant scores for each observation obtained by a linear combination of the training data (orthogonal projection on the direction defining the hyperplane that separates the classes). LDA assumes that the data are normally distributed and all classes identically distributed.
- **QDA:** unlike LDA, this method separates the given classes with a quadratic decision region. In this method, the discriminant scores for each observation are obtained by a non-linear combination of the training data. Since QDA has more degrees of freedom, it tends to perform better than LDA. However, if the database is too small, LDA may provide a better performance.
- **SVM:** this popular classifier aims to separate the classes by creating a linear (or non-linear) decision hyperplane. An optimal separating hyperplane can be found by minimizing the distance between misclassified data points and the decision margin. These misclassified observations are called support vectors, as they determine how SVM discriminates between classes, supporting the classification. In the present work, a Gaussian kernel is used.

Three parameters are extracted and used as features for classification: spectral concentration (SC) in %, kurtosis of the signal in frequency domain and the NMSE-TQ [28].

### 5.4.2 Experimental data and setup

All ECG recordings belong to the PERSIST database and are preprocessed as described in Section 1.3. Experiments are performed on different segments of ECG recordings from 30 different patients suffering from persistent AF, processing all the 12 leads. The physiological characteristics of the patients used in the present experiments are detailed on Table 5.2. It must be reported that, there are missing values of Weight and Height for one patient, AF history for two patients, and LA diameter for three patients. As before, these values were replaced by the average.

Table 5.2: Overall physiological characteristics of the 30-patient population.

Patient characteristics	$\mu \pm \sigma$	Min	Max
Age (years)	$60.6 \pm 10.3$	38	76
Height (cm)	$175.8 \pm 7.2$	156	195
Weight (kg)	$84 \pm 12.6$	54	105
AF History (months)	$74.5 \pm 102.7$	3.5	576
LA Diameter (mm)	$46.9 \pm 8.2$	33	64.1

The Hankel-based BTD is implemented using the NLS approach with the Gauss-Newton method available in Tensorlab MATLAB toolbox [105] choosing  $R = 6$  and  $L_r = L$ , for  $r = 1, 2, \dots, R$ , with  $L$  taking values in the set  $\{17, 48, 95\}$ . The choice of  $R$  is based on the SVD of the observed data matrix, taking into account the most significant singular values. The choice of  $L_r$  is based on the work [110], that shows that such values provide good results for the heartbeat with the largest TQ segment of one of the patients considered in the present experiments. Also, in [25] it is shown that  $L_r = 48$  provides satisfactory results for consecutive segments of the whole ECG recording of the same patient.

The randomly chosen recordings are of 0.82 to 1.75 seconds in length and are down-sampled by a factor of two, since the third-order tensors built from the original sample rate pose some computational difficulties to be processed by the NLS method used to compute the Hankel-BTD. For the matrix-based techniques PCA and RobustICA-f, no downsampling is needed. Monte Carlo runs with Gaussian random initialization for the spatial and temporal factors of Hankel-BTD at each run are used. Monte Carlo runs are needed since the performance of the NLS method depends strongly on the initialization of its factors. These three BSS methods are applied to short ECG recordings from the observed AF patient database, generating 1283 sources that are visually labeled as 551 AA sources and 732 non-AA sources.

### 5.4.3 Classification

After performing BSS using the techniques previously mentioned, the three features (SC, kurtosis and NMSE-TQ) are extracted from the estimated sources. Using these three features, LDA, QDA and SVM are applied to classify the database in AA sources and non-AA sources. Figure 5.6 illustrates these two classes for one of the patients, where it can be seen the original recording in gray and some sources estimates by the Hankel-BTD. The AA source is shown in blue, followed by non-AA sources. In this case the VA source estimate and noise of different amplitudes can be seen.

From the 1283 generated source estimates, 1046 are used for training the classifiers, while 237 are used for testing. A cross-validation with equally sized 5 partitions, i.e.,

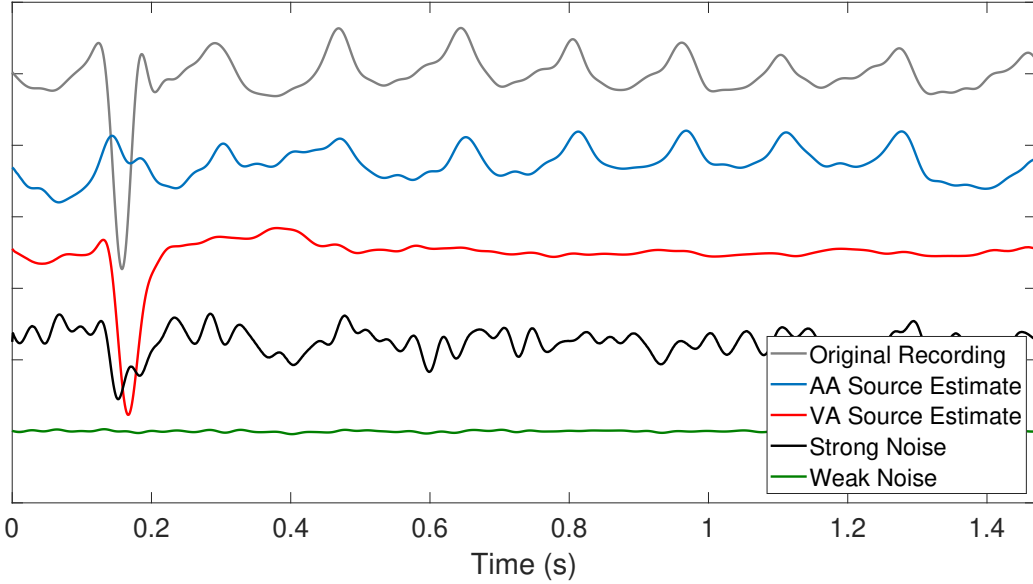


Figure 5.6: Original ECG recording, AA source estimate and non-AA source estimates (VA and noises) on lead V1. The signals are vertically shifted for clarity.

5-fold cross-validation, is performed in all classifiers. This strategy consists in training the model using 4 partitions and testing it in the remaining partition of the data. The performance measure is then the average of the values computed in this loop. Figure 5.7 illustrates the accuracy performance of all the methods compared in this work. The classical method provides an accuracy of 49.90%, being outperformed by the two techniques PM1 and PM2 previously described [24] (Sections 5.3.2 and 5.3.3), which provide 65.66% and 74.53%, respectively. The proposed parameter NMSE-TQ on its own provides 73.07% of accuracy (the signal with the lowest NMSE-TQ is chosen as AA source), almost the same performance as PM2, while the LDA, QDA and SVM classifiers provide 84.39%, 87.34% and 91.98% of accuracy, respectively. As expected, QDA performs better than LDA, as it uses a non-linear region to separate the classes, which seems to suit better the AA source classification problem in AF.

It should be emphasized that if the AA is represented by more than one source in a particular ECG recording, the classifiers are able to discriminate all of them from the non-AA sources. This is not possible with the other techniques here compared, since they are based on the assumption that the AA is represented by a single source.

Table 5.3 shows the confusion matrix of the three classifiers. It can be seen that LDA misclassifies the largest number of sources, with 37 misclassified sources (26 AA and 11 non-AA sources). QDA correctly classifies all the AA sources, but misclassifies more non-AA sources than LDA (30 non-AA sources). SVM, the classifier that provides the highest accuracy, misclassifies the shortest number of sources, with 19 misclassified sources (9 AA and 10 non-AA sources).

It is also observed that the mean and standard deviation ( $\mu \pm \sigma$ ) of SC, kurtosis and NMSE-TQ for the AA sources is  $61.8 \pm 15.1$ ,  $141.3 \pm 65.4$  and  $1.6 \pm 3.0$ , while for the non-AA sources is  $37.8 \pm 14.5$ ,  $41.7 \pm 29.1$  and  $34.9 \pm 111.0$ , respectively. It can be seen that AA sources have very small NMSE-TQ values concentrated in a short range, while non-AA sources have large NMSE-TQ values varying in a long range. This shows that the proposed parameter discriminates very well these signals, which explains why it

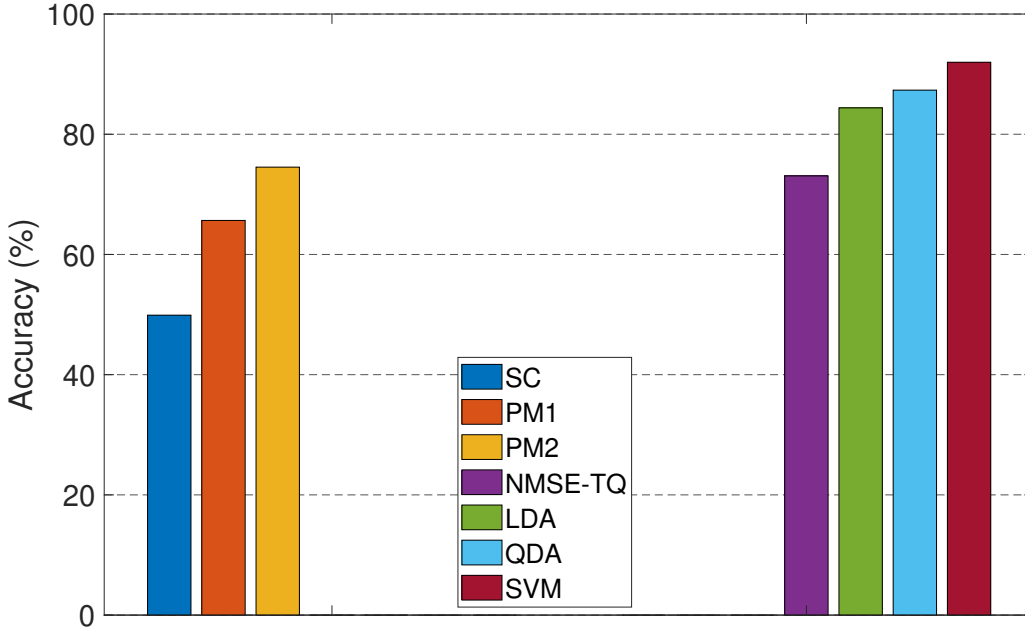


Figure 5.7: AA source selection accuracy by different techniques. Left: SC proposed in [10]; PM1 and PM2 [24] (Sections 5.3.2 and 5.3.3). Right: NMSE-TQ; and the three classifiers: LDA, QDA and SVM.

Table 5.3: Confusion matrix of LDA, QDA and SVM. AcA: actual AA sources, AcN: actual non-AA sources, PrA: predicted AA sources and PrN: predicted non-AA sources.

<b>N = 237</b>	<b>LDA</b>		<b>QDA</b>		<b>SVM</b>	
	<b>PrA</b>	<b>PrN</b>	<b>PrA</b>	<b>PrN</b>	<b>PrA</b>	<b>PrN</b>
<b>AcA</b>	82	26	108	0	99	9
<b>AcN</b>	11	118	30	99	10	119

provides a satisfactory performance when used alone for classification in this challenging application.

## 5.5 Neural networks approach for source classification

Aiming to improve even more the results reported in the previous section, preliminary experiments using a convolutional neural network (CNN) are now briefly reported. Recently, deep learning architectures like the CNN have gained attention mainly by their power of automatically extract complex features from signals and classifying them.

In this scenario, preliminary experiments have trained a shallow CNN model to automatically detect AA sources without the need of hands-on feature extraction steps [72]. The proposed model requires fewer parameters than the well established CNN architectures and also less data in the training phase. Consequently the training time is considerably lower. A tensor-based BSS technique called constrained alternating group lasso (CAGL), that will be introduced later in this thesis, is applied to 116 random segments of 58 12-lead ECG recordings from 58 persistent AF patients of the PERSIST database (Section 1.3), generating 509 sources that are visually labeled as AA, VA and

unknown sources. These segments have around 1 second of duration and a binary classification problem is set to classify AA sources and non-AA sources. The physiological characteristics of the patients used in the present experiments are detailed on Table 5.4. It must be reported that, there are missing values of Weight and Height for six patients, AF history for four patients, and LA diameter for five patients. As before, these values were replaced by the average.

Table 5.4: Overall physiological characteristics of the 58-patient population.

Patient characteristics	$\mu \pm \sigma$	Min	Max
Age (years)	$61.8 \pm 10.2$	38	78
Height (cm)	$174.5 \pm 7.4$	154	195
Weight (kg)	$83.7 \pm 13.1$	54	125
AF History (months)	$69.9 \pm 84.1$	3.5	576
LA Diameter (mm)	$46.9 \pm 7.2$	33	64.1

### 5.5.1 Data augmentation

Due to the low number of segments available, the training of deep learning models can suffer from overfitting. To overcome this problem, a window slicing (WS) based method is applied to augment the data and consequently provides more samples to the training process. This method was first introduced in [17] also in the context of time series classification using CNN and it has proved useful to increase model performance. It affects the training as well as the prediction phase.

For a given ECG segment and its class  $(\underline{\mathbf{x}}_i, y_i)$ , a window with size  $W < |\underline{\mathbf{x}}_i|$  is applied to extract a subsignal  $\underline{\mathbf{x}}_{i,j}$ . The window is moved by  $S \leq W$  samples to obtain a new signal  $\underline{\mathbf{x}}_{i,j+1}$  and the process is repeated until the original segment is completely split.

By applying the WS strategy during the training step, each signal  $\underline{\mathbf{x}}_i$  generates a set of subsignals  $X_i = \{(\underline{\mathbf{x}}_{i,0}, y_i), \dots, (\underline{\mathbf{x}}_{i,N}, y_i)\}$ , all of them sharing the same label  $y_i$ . For the prediction phase, we propose to estimate the value of the class probability  $\tilde{y}_i$  by averaging the model scores of the subsignals, as described in Equation (5.5).

$$\tilde{y}_i = \frac{1}{N} \sum_{j=0}^N \tilde{y}_{i,j} \quad (5.5)$$

where  $N$  is the number of the generated subsignals from  $\underline{\mathbf{x}}_i$  and  $\tilde{y}_{i,j}$  is the model prediction for  $\underline{\mathbf{x}}_{i,j}$ . Just after the data augmentation process, a random oversampling step is applied over the minority class (AA source) in order to balance the training data.

### 5.5.2 Convolutional neural networks

The CNN is a deep learning model initially designed for multi-dimensional data like images. The main components of a CNN are the convolutional layers, the pooling layers and fully connected layers. During the convolutional operation, a bank of filters is applied over the whole input signal using the same weights and it generates activations for each receptive field that are combined to form a feature map [52]. Each set of weights are optimized by a gradient algorithm to detect specific type of features along the input signal.

Along with the convolutional operation, the pooling layers perform a reduction in the feature space and combine similar features [67]. For example, the max-pooling kernel slides the feature space getting the maximum value from small regions.

### 5.5.3 Architecture optimization

To find a suitable CNN configuration for the task of AA source detection, a Bayesian algorithm is applied using BoTorch [3], a framework used for optimization tasks. Different shallow CNN architectures are compared changing the following parameters: number of hidden nodes, training epochs, convolutional/pooling layers, kernel size, kernel stride and batch size.

The maximal number of convolutional layers is set to 3 which keeps the CNN model simpler and much shallower than the common CNN models found in the literature. This reduces the number of trainable weights, thus avoiding overfitting. Along with the model architecture parameters, the augmentation settings (window size and stride) are also optimized. Furthermore, the upper bound value for the window size is limited by the length of the shortest extracted ECG source.

Let  $L$  be the number of convolutional layers and  $k_{i,l}$  the size of the convolutional kernel  $i$  in the layer  $l$ . The constraint  $k_{i,l} \leq k_{i,l+1}$  is imposed on each layer  $l \in \{1, \dots, L-1\}$ . Another constraint requires all kernels from layer  $l$  to have the same size  $K_l$ . Similarly, the stride  $S_l$  for the kernels have to follow the inequality  $S_l \leq S_{l+1}$ . By doing that, it is produced an increasing reduction in the feature space.

A final constraint is defined to have an increasing number of channels in consecutive layers which allows the model to capture more complex features from the signals.

### 5.5.4 Model training and evaluation

The weights for the shallow CNN models are optimized using the Adam optimizer with a learning rate being selected by the Bayesian algorithm. Their values are within the range  $[10^{-4}, 10^{-3}]$ . Each model is evaluated on the validation set with respect to the Area Under the ROC Curve (AUC) aiming to find the model that provides the maximum possible score.

In this work, we consider the AA sources as being the positive class, and the non-AA sources as the negative one. The sensitivity and specificity metrics are used to measure the model performance for each class individually. The sensitivity is defined as:

$$\text{SEN} = \frac{TP}{TP + FN} \quad (5.6)$$

where  $TP$  are the true positive samples and  $FN$  the False Negatives. Similarly, the specificity is computed by (5.7) using the  $TN$  as the number of true negative samples and  $FP$  the quantity of false positive samples:

$$\text{SPE} = \frac{TN}{TN + FP}. \quad (5.7)$$

Finally, the accuracy is computed to measure the overall model precision.

### 5.5.5 Experimental results

After running 100 trials, the best architecture is chosen with an AUC validation score of 97.5%. The best parameters for the CNN are in the Table 5.5. The most appropriate

batch size shown is 124 samples, and for the augmentation window size the best value is 472 with a stride percentage of 21% resulting in an absolute stride of 99 samples.

Table 5.5: Optimized parameters for the shallow CNN architecture.

Layer	Kernel Size	Strides	Output Size
ECG Signal	-	-	$1 \times 472$
Batch Normalization	-	-	$1 \times 472$
Convolution	$1 \times 4$	3	$19 \times 157$
ReLU	-	-	$19 \times 157$
MaxPool	$1 \times 2$	1	$19 \times 156$
Convolution	$1 \times 8$	3	$29 \times 50$
ReLU	-	-	$29 \times 50$
MaxPool	$1 \times 10$	3	$29 \times 14$
Dropout	-	-	$29 \times 14$
Linear	-	-	$1 \times 762$
Dropout	-	-	$1 \times 762$
Linear	-	-	$1 \times 2$
Softmax	-	-	$1 \times 2$

The model evaluation is performed applying a 10-fold cross validation (CV) to compute accuracy (called here ACC, for simplicity) and AUC. Not all data are used in the evaluation; instead, the CV folds are computed only over the training data, since the CNN architecture is selected on the validation set. The average AUC and ACC achieved are 96.3% and 93.6%, respectively and the results across the CV folds are plotted in a boxplot in Figure 5.8.

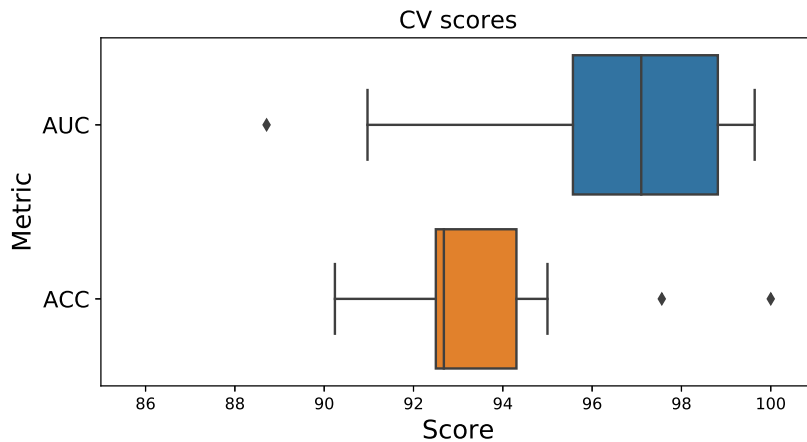


Figure 5.8: Boxplot of the AUC and ACC metrics over CV.

Additionally the model performance is represented in a confusion matrix in Figure 5.9 whose values are based on the CV folds. From the matrix, the obtained sensitivity and specificity metrics are 91.75% and 94.19%, respectively.

## 5.6 Summary

This chapter introduced new indices to quantify the AA content of a cardiac source, after performing BSS, fundamental to understand the analysis that will be carried out in the following chapters. Also, the problem of AA source classification was dealt with using

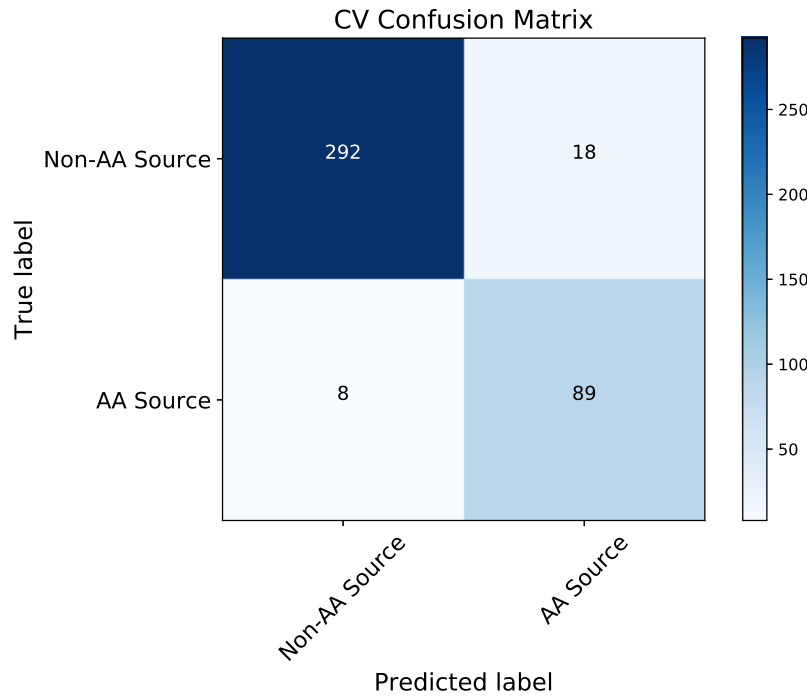


Figure 5.9: CV confusion matrix.

automated and machine learning approaches. The chapter finishes with preliminary, but promising, results from experiments using a shallow CNN architecture in a larger database of AF patients. The next chapter will use the indices introduced in this chapter to assess the Hankel-BTD in a population of AF patients and also through a whole ECG recording.



# Hankel-BTD Performance Evaluation on a Patient Database

---

## Contents

<b>6.1</b>	<b>Introduction</b>	<b>63</b>
<b>6.2</b>	<b>Intra-patient variability: window position</b>	<b>64</b>
6.2.1	Experimental data and setup	64
6.2.2	Experimental results	65
<b>6.3</b>	<b>Intra-patient variability: window size</b>	<b>67</b>
6.3.1	Experimental data and setup	67
6.3.2	Experimental results	68
<b>6.4</b>	<b>Inter-patient variability</b>	<b>70</b>
6.4.1	Experimental data and setup	70
6.4.2	Experimental results	71
<b>6.5</b>	<b>Summary</b>	<b>73</b>

---

## 6.1 Introduction

To date, the Hankel-BTD has only been assessed in fixed ECG segments of a single patient suffering from persistent AF. Aiming to further exploit the performance and feasibility of this tensor-based method, this chapter reports more throughout experiments. First, the Hankel-BTD is assessed in consecutive segments of a whole ECG recording. Then, the observation window size of a processed segment is varied. These two experiments result in an outcome called here as intra-patient variability. Finally, the Hankel-BTD is assessed in short segments of a population of persistent AF patients, yielding an evaluation of inter-patient variability. The performance of all BSS methods that are used in this chapter are measured by means of the indices presented on Chapter 5. The results reported in this chapter provided the following publications:

- P. M. R. de Oliveira and V. Zarzoso, “Block term decomposition of ECG recordings for atrial fibrillation analysis: temporal and inter-patient variability”, *Journal of Communication and Information Systems*, vol. 34, no. 1, pp. 111-119, Apr. 2019.
- P. M. R. de Oliveira and V. Zarzoso, “Temporal stability of block term decomposition in noninvasive atrial fibrillation analysis”, in *Proc. Asilomar-2018, 52nd Annual Asilomar Conference on Signals, Systems, and Computers*, Pacific Grove, U.S.A, Oct. 28-31, pp. 816-820, 2018.

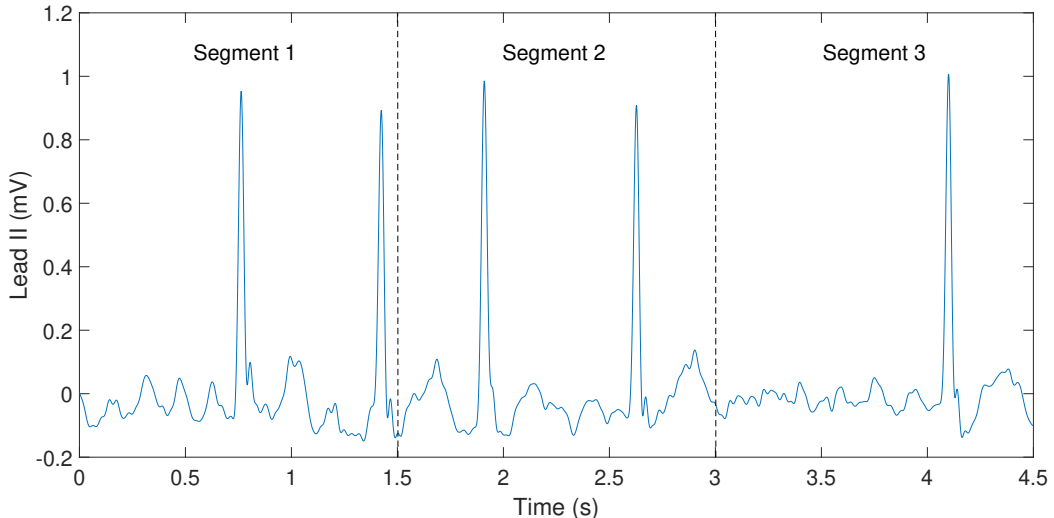


Figure 6.1: The first 3 segments of the AF ECG recording composed of 56 segments. Although all the 12 leads are processed, only limb lead II is shown for clarity.

- P. M. R. de Oliveira and V. Zarzoso, “Block term decomposition analysis in long segments of atrial fibrillation ECGs”, in *Proc. SBrT-2018, XXXVI Simpósio Brasileiro de Telecomunicações e Processamento de Sinais*, Campina Grande, Brazil, Sep. 16-19, pp. 578-582, 2018.

## 6.2 Intra-patient variability: window position

This section will assess the Hankel-BTD in consecutive segments of an AF ECG recording of a single patient. Performance is measured by means of SC, kurtosis and power contribution to lead V1, presented in Chapter 5.

### 6.2.1 Experimental data and setup

The reported experiments in this section consider 56 segments of a single standard 12-lead AF ECG recording from the PERSIST database (Section 1.3). The patient is chosen as the same as in the work [110], in order to take advantage of the model parameters estimated in that work. All 56 segments compose the whole ECG recording.

The first three segments in lead II from the observed patient are shown in Figure 6.1. All the segments have a fixed length of 1500 samples (about 1.53 seconds) and all the 12 leads are used in the experiments. The segments are downsampled by a factor of four, resulting in third-order tensors of dimensions  $188 \times 188 \times 12$ , since the originally built third-order tensors of dimensions  $750 \times 751 \times 12$  pose some computational difficulties to the NLS algorithm used to compute the Hankel-BTD.

The Hankel-BTD is implemented using the NLS approach with the Gauss-Newton method available in Tensorlab MATLAB toolbox [105] choosing  $R = 12$  and  $L_r = L$ , for  $r = 1, 2, \dots, R$ , with  $L$  taking values in the set  $\{17, 48, 95\}$ . This choice is chosen based on the work [110], as explained in Chapter 5. The tolerance threshold for Hankel-BTD convergence is set to  $10^{-9}$  and the maximum number of iterations is set to 1000. Monte Carlo runs with Gaussian random initialization for the spatial and temporal factors at each run are used to analyze the performance of Hankel-BTD in each segment regarding

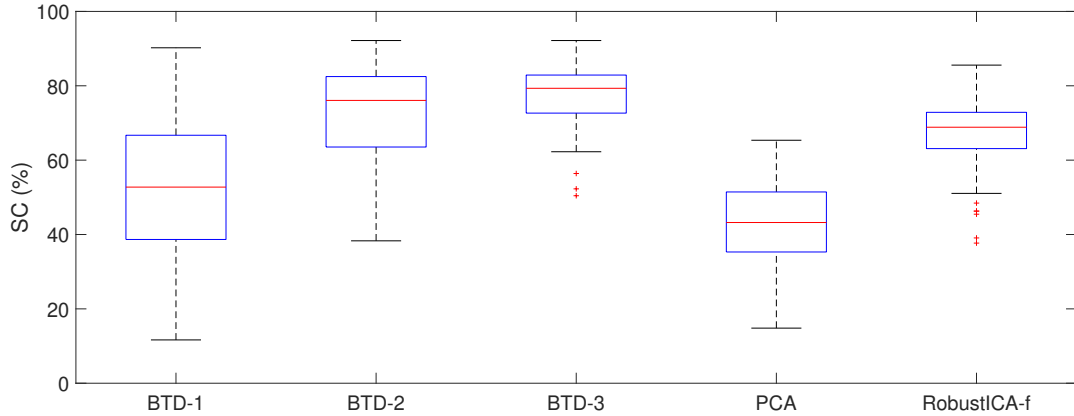


Figure 6.2: Distribution of SC values (%) for each version of Hankel-BTD, as well as PCA and RobustICA-f.

AA signal extraction. Monte Carlo runs are needed since the performance of the NLS method depends strongly on the initialization of its factors as explained in the previous chapter.

In order to adapt each ECG segment to a specific model parameter  $L_r$ , three experiments in the whole AF ECG recording are performed [25]:

- BTD-1: A single Monte Carlo run for each segment using  $L_r = 48$ .
- BTD-2: 10 Monte Carlo runs for each segment using  $L_r = 48$ , then the best performance out of the 10 independent runs is chosen, considering the quality of the estimation measured by the indices introduced in Chapter 5.
- BTD-3: For the segments with unsatisfactory AA extraction, i.e., with low values of SC and  $K$ , in the second experiment, 10 new Monte Carlo runs are performed changing the rank  $L_r$  to 17 or 95 (the one which performed best), then the best performance out of the 10 Monte Carlo runs is chosen, as in the second experiment.

### 6.2.2 Experimental results

In Figures 6.2 and 6.4, the blue box, the red line, the whiskers and the red dots represent the 25th and 75th percentiles, the median, the extreme values and the outliers, respectively, of the data.

Figure 6.2 shows how the SC of the atrial source is distributed over the 56 segments that compose the whole AF ECG for the three experiments performed with Hankel-BTD, as well as PCA and RobustICA-f. The improvement of BTD-2 over BTD-1 is expected and illustrates the dependence of the NLS method on the initialization of the matrix factors, since the model parameters are kept fixed and only more Monte Carlo runs are performed. The improvement of BTD-3 over the previous experiments illustrates the need for choosing the right model parameters in order to have satisfactory performance. This improvement is also expected, since this experiment tries to adapt the multilinear rank to each segment, using the same number of Monte Carlo runs as BTD-2. Figure 6.2 also shows that if the right initialization and model parameters are chosen, Hankel-BTD can clearly outperform PCA and RobustICA-f, two well-known matrix-based methods. These improvements are observed as the SC becomes more concentrated around high values, which means more stability in successful AA extractions.

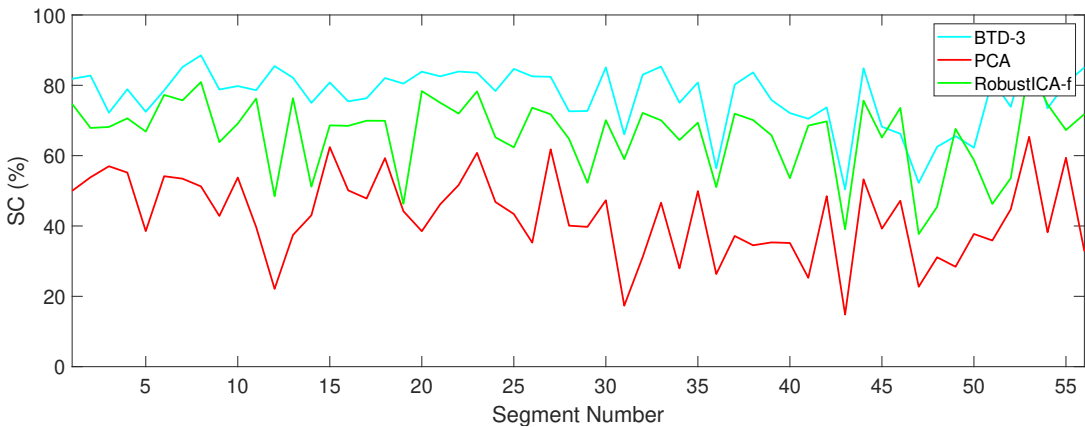


Figure 6.3: Variation of SC values (%) over the 56 segments for BTD-3, PCA and RobustICA-f.

Table 6.1: Mean values of SC (%) and  $K$  for the three versions of Hankel-BTD, as well as PCA and RobustICA-f.

	<b>SC</b>	<b>K</b>
<b>BTD-1</b>	53.02	151.33
<b>BTD-2</b>	71.80	242.35
<b>BTD-3</b>	76.95	260.41
<b>PCA</b>	42.75	95.72
<b>RobustICA-f</b>	66.10	216.06

In Figure 6.3, the temporal stability of Hankel-BTD can be seen from another perspective, showing how the SC values of the AA signal varies over the 56 segments. For the sake of clarity, only BTD-3, the tensor version that provided the best performance, is shown together with PCA and RobustICA-f. It can be seen that the matrix-based methods present considerable variations over the whole ECG, whereas BTD-3 provides a SC more concentrated in high values, showing that this technique can provide a satisfactory AA extraction performance stable over time.

The superiority of Hankel-BTD as an AA extraction tool over the matrix-based techniques is also shown in Table 6.1. It can be seen that as the initialization of the factors and the model parameters are adapted to each segment, the average AA extraction quality is improved, as measured by SC and  $K$ . In these experiments, the index  $P(r)$  is used only to eliminate weak sources and not to measure the quality of the AA extraction, thus it is not shown in Table 6.1.

Since AA signals in AF ECGs are non-stationary, it is expected that the DF slowly changes with time, i.e., over the segments of the same recording. Figure 6.4 shows that the DF of the estimated atrial source by BTD-2, BTD-3, PCA and RobustICA-f lies in the interval 5.24-6.67 Hz, despite the outliers. In BTD-1 the DF interval is expected to be greater, since for many of the segments this method did not provide a satisfactory AA extraction, as we used fixed parameters to compute the Hankel-BTD with a single initialization of its factors.

Indeed, BTD-1 provides an unsatisfactory AA extraction in 21 out of the 56 segments. For BTD-2 this number dropped to 5, while for BTD-3 no unsatisfactory AA extractions

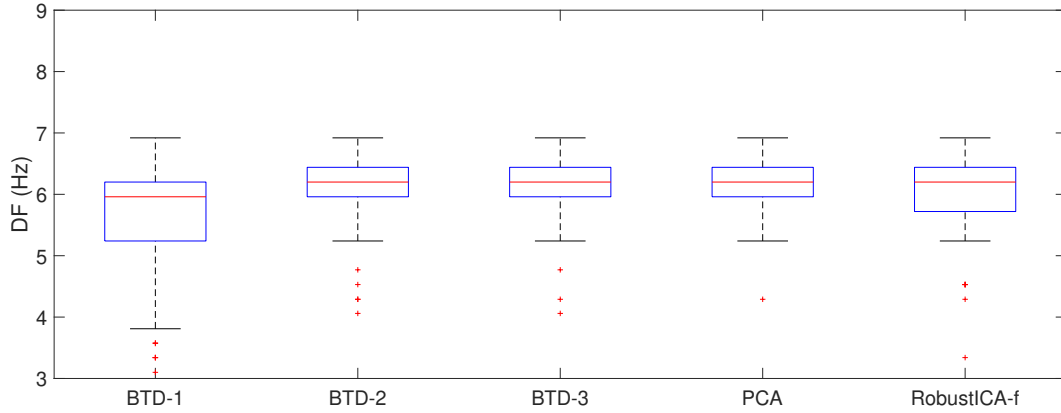


Figure 6.4: Variation of DF (Hz) for each version of Hankel-BTD, as well as PCA and RobustICA-f.

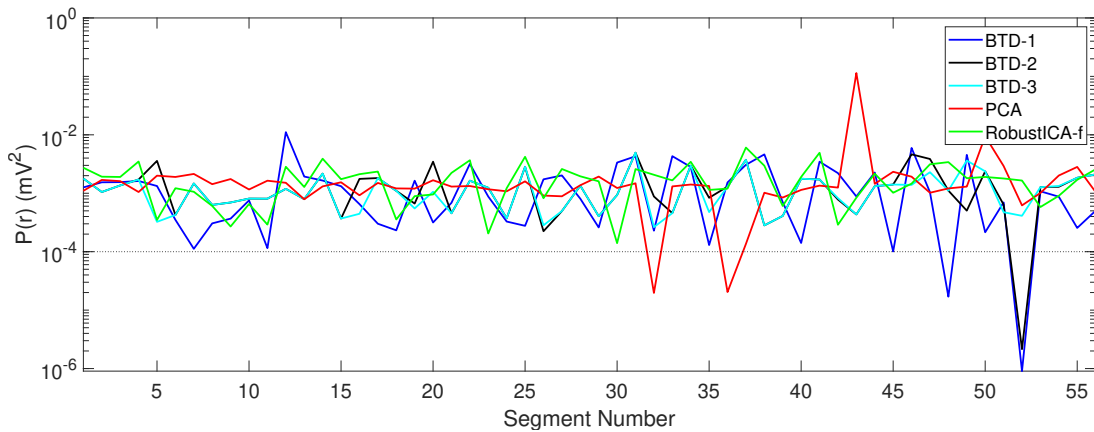


Figure 6.5: Power contribution to lead V1 values ( $\text{mV}^2$ ) for the selected atrial source over the 56 segments for each version of Hankel-BTD, as well as PCA and RobustICA-f.

are performed. It is fair to report that PCA performed 9 unsatisfactory AA extractions and RobustICA-f only 7. In Figure 6.5 it can be seen that some estimated atrial sources for PCA, BTD-1 and BTD-2 have a  $P(r)$  value under  $10^{-4}$   $\text{mV}^2$ . This is suggestive of an unsatisfactory AA extraction, since a source with power contribution to lead V1 under this threshold does not present significant AA content, as reported in [24] and in Chapter 5 of the present doctoral thesis.

## 6.3 Intra-patient variability: window size

Experiments reported in this section will analyze the impact of the observation window size of the processed ECG segment, by varying this parameter.

### 6.3.1 Experimental data and setup

To assess intra-patient variability, experiments are performed in 4 segments varying the observation window size of a standard 12-lead ECG recording from a single patient suffering from persistent AF of the PERSIST database. The recordings are preprocessed as described in Section 1.3. All 12 leads are considered. A 15-second segment in lead II from this patient is shown on Figure 6.6. The segments assessed for this patient have

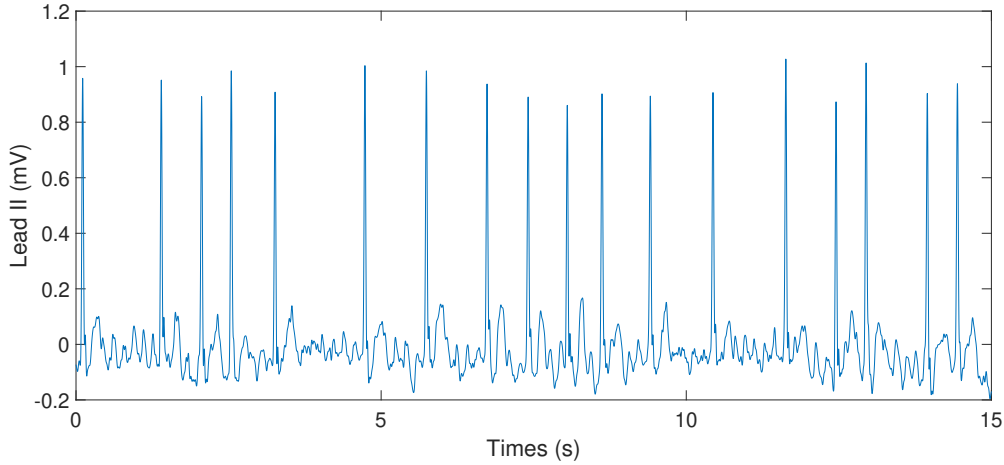


Figure 6.6: A 15-second segment of an AF ECG recording from the patient used for evaluate the time variability. For concision, only lead II is shown; all 12 leads are processed.

about 2.5, 5, 10 and 15 seconds and they all have the same starting sample. They are downsampled by a factor of 4, 8, 16 and 24, respectively, since the originally built third-order tensors pose some computational difficulties to the NLS method used. Down-sampling includes a low-pass filtering with cutoff frequency  $f_c = f'_s/2$ , where  $f'_s$  is the new sampling frequency. For the matrix-based techniques PCA and RobustICA-f, no downsampling is needed.

Hankel-BTD is implemented using the NLS approach with the Gauss-Newton method available in Tensorlab MATLAB toolbox [105] choosing  $R = 12$  and  $L_r = 95$ , for all  $r = 1, 2, \dots, R$ . This choice is made also based on the work [110]. The tolerance threshold for Hankel-BTD convergence is set to  $10^{-9}$  and the maximum number of iterations is set to 1000. Ten Monte Carlo runs, with Gaussian random initialization for the matrix and vector factors at each run, are used to analyze the performance of Hankel-BTD regarding AA signal extraction. This tensorial technique is compared to the matrix-based methods PCA and RobustICA-f, which have already proven their effectiveness in solving BSS problems for this particular application.

### 6.3.2 Experimental results

Table 6.2 shows the values of SC in % for PCA and RobustICA-f. The mean of the ten independent runs and the maximum value is shown for Hankel-BTD. It can be seen in Table 6.2 that the mean of the SC for Hankel-BTD is very close to the matrix-based techniques, outperforming PCA in all the observed segments and RobustICA-f in 3 out of the 4 segments with different lengths. Also, Hankel-BTD is superior for all observed segments in 5 to 8 out of the 10 independent runs, showing that it can easily have superior performance if the right model parameters ( $R, L_r$ ) and initialization are chosen. It can also be seen that the maximum SC presents a high value ( $\geq 75\%$ ) for all the observed segments, and in all cases, superior to that of matrix techniques, meaning that, with the right initialization, BTD outperforms the matrix-based techniques for the considered window lengths.

In the observed segments with different lengths, Hankel-BTD finds more potential atrial sources than PCA and RobustICA-f. Discovering more than one potential atrial sources may be an interesting outcome, since it increases the possibility of finding some

Table 6.2: Values of SC (%) for PCA and RobustICA-f. For Hankel-BTD, the maximum ( $BTD_{max}$ ) and the mean ( $BTD_{mean}$ ) values of SC (%) of ten independent runs are shown.

	<b><math>BTD_{max}</math></b>	<b><math>BTD_{mean}</math></b>	<b>PCA</b>	<b>RobustICA-f</b>
<b>2.5s</b>	94.04	74.03	55.29	69.08
<b>5s</b>	77.88	65.56	49.03	66.13
<b>10s</b>	90.93	73.49	56.40	72.22
<b>15s</b>	93.01	77.87	54.36	71.80

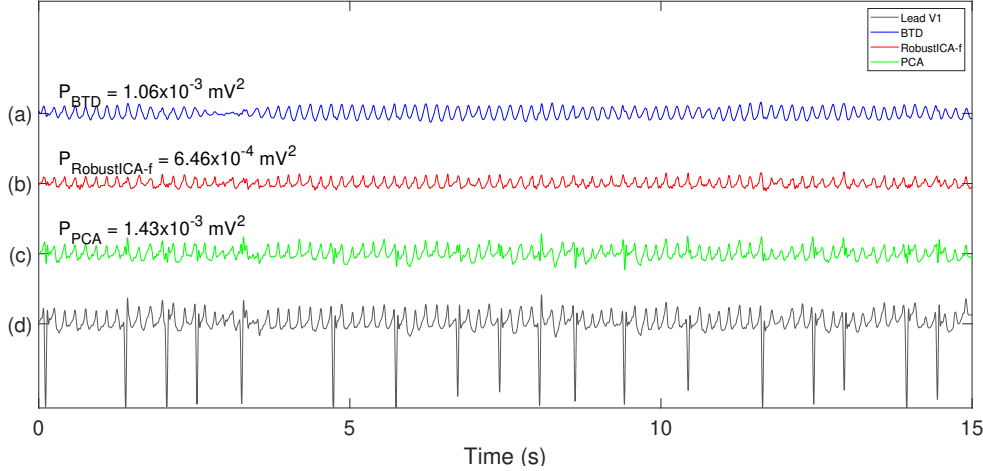


Figure 6.7: Atrial source contribution to lead V1 estimated by Hankel-BTD, RobustICA-f and PCA, for the 15-second segment, showed in the time domain (in mV). AA signal estimates are vertically shifted for clarity. The power contribution to lead V1 for each technique is also shown.

features that, although weakly contributing to the overall AA, may provide useful physiological and clinical information about the arrhythmia. This possibility, however, will not be explored in the present doctoral thesis.

Figures 6.7 and 6.8 illustrate the estimated atrial source by the three BSS techniques compared in this section, in the time and frequency domain, respectively, for the best performance of Hankel-BTD in the 15-second segment. These two figures show the satisfactory performance of Hankel-BTD in estimating the AA in long segments of an AF ECG, as well as its superiority compared to the matrix-based methods, as quantified by the higher SC and kurtosis values and illustrated by a cleaner frequency spectrum, less contaminated by noise and interference.

The observation window size used in the experiments extends from 2.5 to 15 seconds in order to analyze its influence on Hankel-BTD performance. Figures 6.9 and 6.10 show the variation of SC and kurtosis, respectively, over the 10 independent runs for the window observation sizes analyzed in these experiments. This variation is illustrated by box-and-whisker plots.

It can be seen that there exists a certain variation of SC and kurtosis over the runs, for each observation window size. This is expected, since the performance of the used Hankel-BTD computation method, the NLS algorithm, depends considerably on the initialization of its model factors. However, there is no clear trend in the computed parameters, which seems to indicate that the influence of the observation window size on

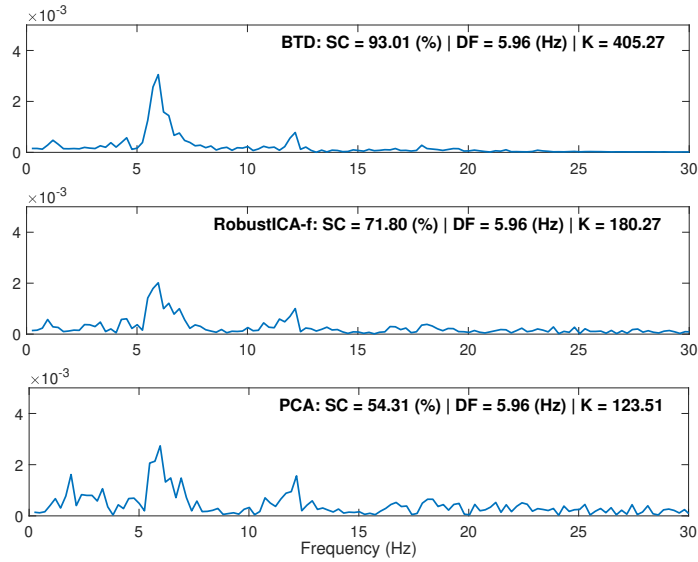


Figure 6.8: Atrial source contribution to lead V1 in the 15-second segment estimated by Hankel-BTD, RobustICA-f and PCA in the frequency domain (in  $\text{mV}/\sqrt{\text{Hz}}$ ).

the performance of Hankel-BTD is not very significant or critical [26].

The only drawback observed when processing long segments of ECG using BTD is the fact that the original segment must be downsampled by high factors, since the used Hankel-BTD computation algorithm has some difficulties in processing a tensor with large dimensions [23]. Downampling by a high factor could cause some loss of information in the signal, due to the frequency filter used to avoid spectral aliasing. However, previous experiments in short segments show that the impact of the downampling factor on the SC is negligible. Actually, it is observed that the downsampled segments provide a slightly lower SC compared to the original segment (without any downampling), which makes the results reported here a lower bound of Hankel-BTD performance in the considered scenario.

## 6.4 Inter-patient variability

The Hankel-BTD is now assessed in short ECG segments from a population of patients suffering from persistent AF, fixing the model parameters, in order to analyze the sensibility of this technique over signals with different physiological signature.

### 6.4.1 Experimental data and setup

To assess the inter-patient variability, experiments in a population of AF patients are performed, providing more relevant clinical results. Experiments consider a randomly selected heartbeat (QRST complex + TQ segment) of 20 real standard 12-lead AF ECG recordings from 20 different patients suffering from PERSIST database (Section 1.3). A single-beat segment in lead II from one of the patients in the 20-patient population is shown on Figure 6.11, where the TQ interval can be seen just after the QRST complex. All the beats (one per patient) have between 1000 and 1400 samples (1.02 and 1.43 seconds). They are downsampled by a factor of 2, for the same reason previously explained. The physiological characteristics of the observed 20-patient population are described on Table 6.3. It must be reported that there are missing data values for one

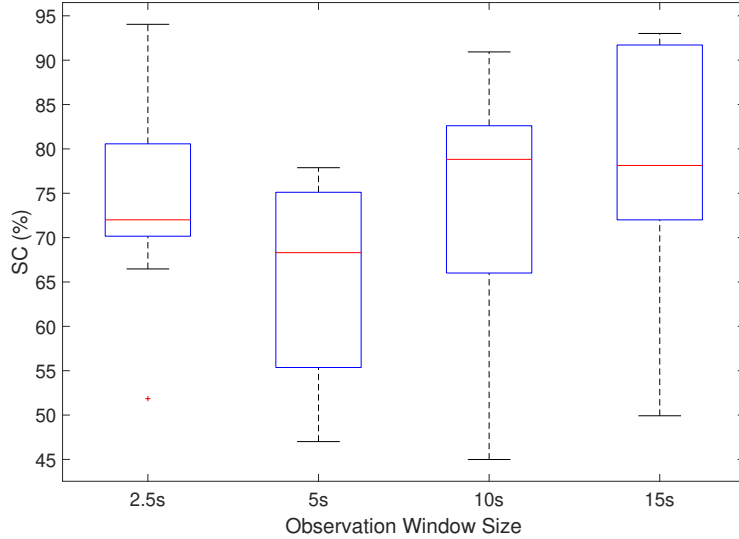


Figure 6.9: SC (%) of the AA signals estimated by Hankel-BTD from the observed AF ECG segments over ten independent runs. Runs that did not provide a successful AA extraction are not included.

patient regarding AF history and LA diameter and such values were replaced by the average.

Table 6.3: Overall physiological characteristics of the 20-patient population.

Patient characteristics	$\mu \pm \sigma$	Min	Max
Age (years)	$63.5 \pm 8.5$	42	76
Height (cm)	$176.8 \pm 6.5$	166	195
Weight (kg)	$86.1 \pm 11.8$	64	105
AF History (months)	$73.1 \pm 57.9$	8	228
LA Diameter (mm)	$47.2 \pm 7.5$	33	62

The setup of Hankel-BTD computation is the same used in the experiments of the previous section.

#### 6.4.2 Experimental results

Table 6.4 shows the values of SC in % for PCA and RobustICA-f in the 20-patient population. The mean of the ten independent runs and the maximum value is shown for Hankel-BTD. We can see in Table 6.4 that the mean of the SC for Hankel-BTD is very close to the matrix-based techniques, outperforming PCA in almost all the observed patients (except patients 8, 12 and 16) and RobustICA-f in 11 patients. Also, Hankel-BTD is superior for all patients in 3 to 7 out of the 10 independent runs, showing again that it can easily have superior performance if the right parameters ( $R$ ,  $L_r$ ) and the right initialization are chosen. We can also see that the maximum SC is satisfactory ( $\geq 65\%$ ) for all but three patient (P10, P11 and P19), and in all but two cases (P11 and P20), superior to that of matrix techniques, meaning that, with the right initialization, Hankel-BTD is superior in almost all cases of this experiment.

In the observed population of patients, Hankel-BTD found more potential atrial sources ( $DF \in [3, 9]$  Hz) than PCA and RobustICA-f. As previously explained, find-

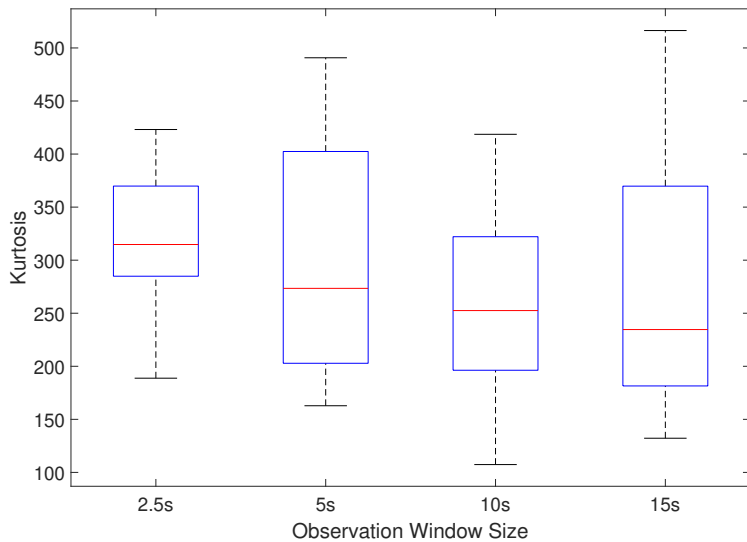


Figure 6.10: Kurtosis of the AA signals estimated by Hankel-BTD from the observed AF ECG segments over ten independent runs. Runs that did not provide a successful AA extraction are not included.

ing several potential atrial sources may be an interesting result, increasing the possibility of finding features that weakly contribute to the AA, while providing important physiological and clinical information about a complex arrhythmia like persistent AF.

As previously explained, this doctoral thesis assumes, as in previous works, that the AA is concentrated on a single source, which is selected as the source presenting the most significant AA content, measured by the indices previously presented. However, in the present experiments, in some runs of 5 out of the 20 patients, AA appears in more than one source estimated by Hankel-BTD. This can be seen in Figure 6.12(a), where two estimated sources by Hankel-BTD present significant AA content (signals 2 and 3). This could mean that Hankel-BTD is able to extract more information about the AA than the other methods compared here. To keep the focus on the subject of this work, a deep analysis of the cases where Hankel-BTD provided more than one source with significant AA is not discussed in this thesis.

Figure 6.12 shows the 3 most relevant potential atrial sources of one of the observed patients (Patient 6). For clarity, all the potential atrial sources with power contribution to lead V1 less than  $10^{-4}$  are not shown here, since they do not present significant features as they are very weak. In the time domain, shown in Figure 6.12(a), we can see that the two last sources have the atrial signature and present a high power contribution to lead V1, while looking at the frequency domain, in Figure 6.12(b), we can see that those sources present high kurtosis and SC, represented by indexes  $K$  and SC in the figure legend, respectively. The first source seems to contain mainly a ventricular residual.

Figure 6.13 shows how the SC of the atrial source is distributed over the 10 independent runs for the population of 20 observed AF patients. We can see that the median (red line) and the percentiles (blue box) present significant variations over Hankel-BTD initialization and over patients. A fixed tensor-model parameter choice and Gaussian random initializations for each run are used to compute the Hankel-BTD in 20 AF patients, providing generally satisfactory results. However, it can be observed that the chosen parameters work better in some patients than in others, recalling that Hankel-BTD performance depends strongly on its parameters and initialization, and opening the

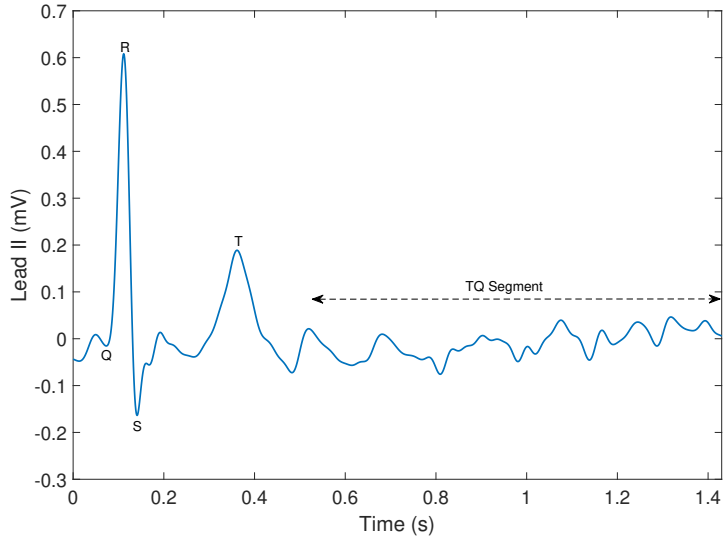


Figure 6.11: A single heartbeat segment of an AF ECG recording, shown in lead II, from one patient of the observed population. A heartbeat consists in the QRST complex, followed by the TQ segment, where only AA is observed.

challenge of finding the best fixed choice of tensor-model parameters for a particular patient. This challenge is faced with a novel algorithm that will be presented in Chapter 8 of this doctoral thesis.

It can be pointed out that in patients 9, 10, 15 and 17 the matrix-based methods could not successfully extract the AA signal from the considered segment, while the Hankel-BTD could easily extract it from the observed AF ECG segments. Despite its higher computational complexity, this outcome shows that Hankel-BTD is capable of extracting the AA signal from segments where the matrix-based techniques here compared could not, pointing out the superiority of Hankel-BTD as an AA extraction tool.

We can see in Figure 6.14 that the DF of the estimated atrial source by Hankel-BTD does not change considerably over the runs for a given patient (except for the first runs of Patient 12), which means that Hankel-BTD seems to be able to target the AA source consistently, although with varying accuracy depending on the algorithm convergence. Over the population of observed patients, the DF of the atrial sources estimated by Hankel-BTD are in the interval of 4.77 to 6.67 Hz, very close to the DF interval of the atrial sources estimated by PCA and RobustICA-f, which lie in 4.77 to 6.44 Hz.

## 6.5 Summary

This chapter reported several experiments in order to assess the performance and feasibility of the Hankel-BTD as an AA extraction tool. Experiments in consecutive segments of a single AF ECG recording have shown the strong dependency of this technique on its initialization and model parameters, being capable of providing stable performance if the best tensor-model parameters are chosen. Further experiments varying the observation window size did not show any significant variation of the AA extraction performance of this tensor-based technique. Finally, experiments over short ECG segments from a population of AF patients, fixing the tensor-model parameters, have shown the variability performance through different physiological signals.

Table 6.4: Values of SC (%) for PCA and RobustICA-f. For Hankel-BTD, the maximum ( $BTD_{max}$ ) and the mean ( $BTD_{mean}$ ) values of SC (%) of ten independent runs are shown.

	$BTD_{max}$	$BTD_{mean}$	PCA	RobustICA-f
<b>P1</b>	78.03	67.69	62.54	68.27
<b>P2</b>	96.15	80.08	65.14	81.25
<b>P3</b>	90.01	70.36	65.16	74.04
<b>P4</b>	92.67	85.88	68.38	69.76
<b>P5</b>	85.30	77.60	58.36	74.91
<b>P6</b>	85.32	69.16	45.57	61.76
<b>P7</b>	77.12	60.93	46.88	64.78
<b>P8</b>	93.78	70.60	74.47	79.33
<b>P9</b>	67.13	53.84	none	none
<b>P10</b>	53.01	45.46	none	none
<b>P11</b>	54.97	47.02	none	71.07
<b>P12</b>	65.02	48.23	48.73	60.25
<b>P13</b>	90.27	66.92	60.18	61.75
<b>P14</b>	90.36	70.15	none	53.35
<b>P15</b>	68.56	60.53	none	none
<b>P16</b>	81.46	58.44	68.43	77.69
<b>P17</b>	87.70	68.58	none	none
<b>P18</b>	78.78	73.08	none	70.06
<b>P19</b>	57.29	51.87	none	48.64
<b>P20</b>	72.97	64.77	48.18	84.61

Until now, only the BTD built from Hankel matrices has been considered and assessed. Also, only AF ECGs with long TQ segments and significant AA content were used. The next chapter will provide alternative tensor models of an AF ECG to perform the AA extraction in more challenging scenarios of persistent AF.

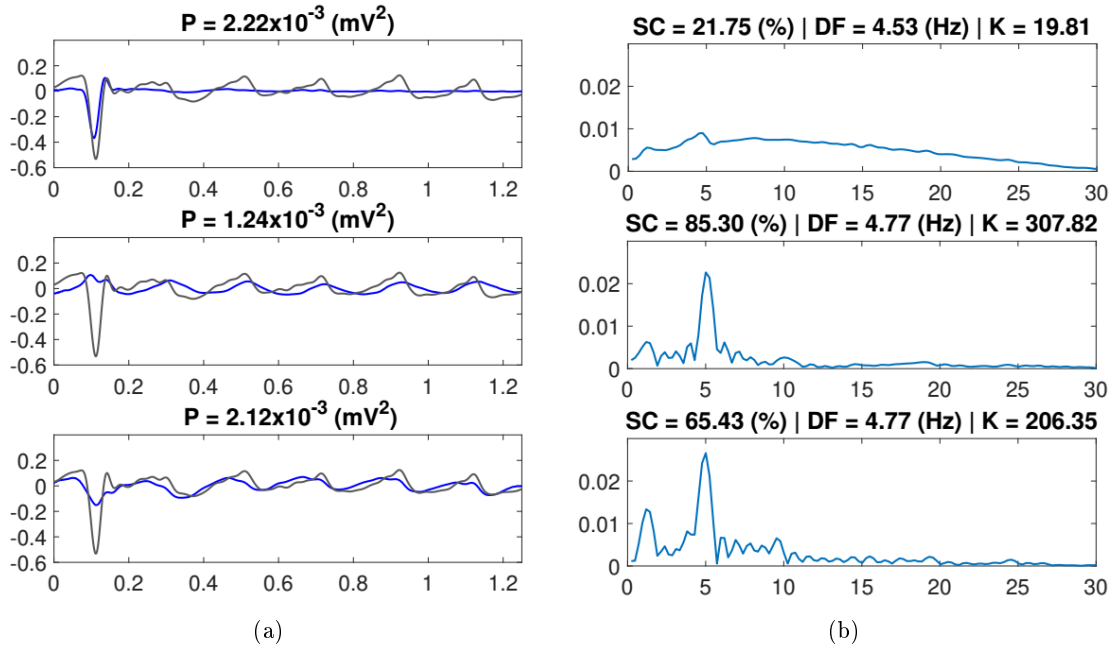


Figure 6.12: Potential atrial sources contribution to lead V1 estimated by Hankel-BTD for Patient 6. (a) In the time domain, measured in mV. (b) In the frequency domain, measured in  $\text{mV}/\sqrt{\text{Hz}}$ .

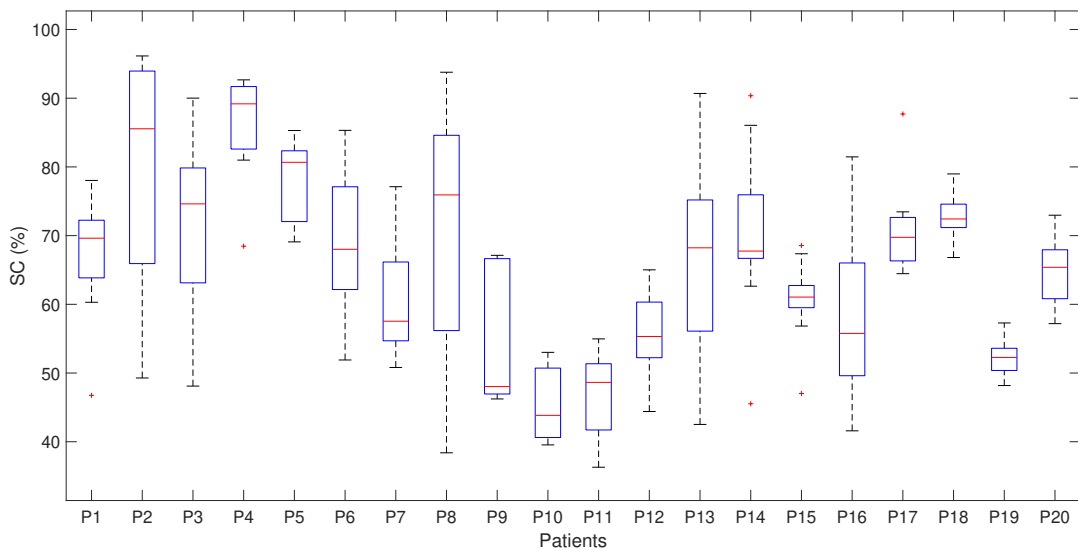


Figure 6.13: Variation of SC (%) of the atrial source estimated by Hankel-BTD over 10 tensor factor initializations for the observed population of AF patients. Runs that did not provide a successful AA extraction are not shown.

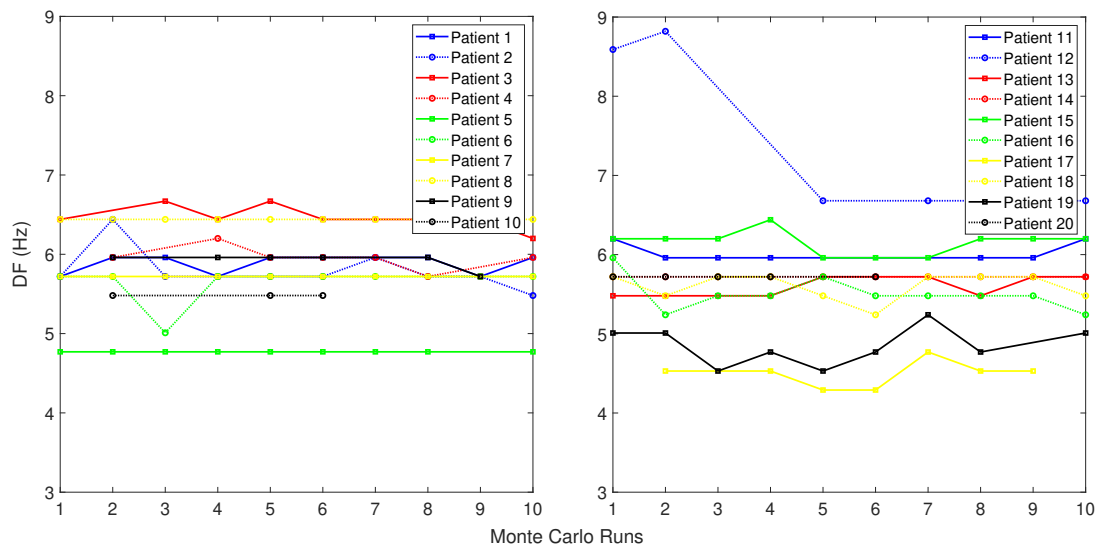


Figure 6.14: Variation of DF (Hz) of the atrial source estimated by Hankel-BTD over independent runs for the observed population of AF patients. Runs that did not provide a successful AA extraction are not shown.

# BTD Models for AF Analysis

---

## Contents

<b>7.1</b>	<b>Introduction</b>	<b>77</b>
<b>7.2</b>	<b>Löwner-based block term decomposition</b>	<b>77</b>
7.2.1	Model derivation	78
7.2.2	Experimental data and setup	79
7.2.3	Segments with short RR intervals	80
7.2.4	Segments with disorganized and/or weak AA	81
<b>7.3</b>	<b>Coupled block term decomposition</b>	<b>82</b>
7.3.1	Model derivation	83
7.3.2	Evaluation on synthetic data	84
7.3.3	Evaluation on real data	85
<b>7.4</b>	<b>Summary</b>	<b>87</b>

---

## 7.1 Introduction

In persistent AF ECGs, it is common the presence of short TQ segments, hampering the estimation of AA. Also, AA signals with very low amplitude are quite frequent in persistent forms of AF [82]. The Hankel-BTD fails to extract the AA signal from ECGs that present such characteristics. This motivates another tensor-based approach, presented in the first section of this chapter. This alternative approach is based on Löwner matrices. Later, assuming that consecutive ECG segments share the same spatial signature, a novel tensor model can be employed, reducing iteration cost of the computing algorithm and providing better AA extraction performance. The present chapter provided the following publications:

- P. M. R. de Oliveira, V. Zarzoso and C. A. R Fernandes, “Coupled tensor model of atrial fibrillation ECG”, to appear in Proc. *EUSIPCO-2020, 28th European Signal Processing Conference*, Amsterdam, Netherlands, Jan. 18-22, 2021.
- P. M. R. de Oliveira and V. Zarzoso, “Löwner-based tensor decomposition for blind source separation in atrial fibrillation ECGs”, in *Proc. EUSIPCO-2019, 27th European Signal Processing Conference*, A Coruña, Spain, Sep. 2-6, pp. 1-5, 2019.

## 7.2 Löwner-based block term decomposition

The Hankel-BTD has proven to be a useful and powerful AA extraction tool in AF analysis. However, a satisfactory performance is only achieved for segments with long RR intervals and with well defined AA, visible in most of the segment. However, recordings

with short RR intervals ( $< 0.75$  s) and weak AA (amplitude of the f waves lower than 0.1 mV) are quite common during persistent AF episodes. When assessed in these challenging cases, the Hankel-BTD as well as the matrix-based techniques do not provide satisfactory results [27]. Automatically selecting the AA signal among the estimated sources after performing BSS is also an issue, since no optimal method is reported in the literature for this application. The solutions presented in Chapter 5 can only be considered as sub-optimal.

In a bid to avoid such limitations in these common and challenging scenarios of persistent AF, it is proposed the BTD built from Löwner matrices as a solution for BSS of rational functions [30] to model the VA and separate it from the AA. This strategy suits the characteristics of VA in a ECG recording, since the QRS complex can be well approximated by rational functions [73], [38], and when mapped onto Löwner matrices, the degree of the rational function matches the rank of the Löwner matrix [30]. Modeling VA instead of AA is a reasonable strategy in these difficult cases (weak AA and/or short RR intervals) common in persistent AF episodes, as the AA signal becomes very difficult to model [27]. The VA estimated by the Löwner-BTD is then subtracted from the ECG signal, resulting in a signal that contains mainly AA content. Through this method, no technique for atrial source selection is needed, since the resulting signal is already the desired signal.

Since the QRST morphology is not significantly changed during AF, it is reasonable to focus on VA estimation, as, when subtracting the VA estimate from the ECG, the resulting signal will ideally contain the AA signal. Even if significant changes in QRST morphology are present, VA modeling can be performed in a beat-to-beat basis, relying on the power of tensor-based techniques to provide satisfactory performance on short data records. This ability has been illustrated in the experimental analysis of the Hankel-BTD approach in Chapter 6 of this doctoral thesis.

### 7.2.1 Model derivation

The idea is to map each row of the data matrix  $\mathbf{Y}$  into a Löwner matrix  $\mathbf{L}^{(k)} \in \mathbb{R}^{I \times J}$  as [30]:

$$\mathbf{L}^{(k)} = \begin{bmatrix} \frac{y_{k,x_1} - y_{k,z_1}}{x_1 - z_1} & \dots & \frac{y_{k,x_1} - y_{k,z_J}}{x_1 - z_J} \\ \vdots & \ddots & \vdots \\ \frac{y_{k,x_I} - y_{k,z_1}}{x_I - z_1} & \dots & \frac{y_{k,x_I} - y_{k,z_J}}{x_I - z_J} \end{bmatrix} \quad (7.1)$$

where  $I + J = N$  and  $y_{k,t_n}$  is the  $t_n^{\text{th}}$  time sample for the  $k^{\text{th}}$  row of  $\mathbf{Y}$ , sampled in the time set  $T = \{t_1, t_2, \dots, t_N\}$ , which is partitioned in two different non-overlapping time sets:  $X = \{x_1, x_2, \dots, x_I\}$  and  $Z = \{z_1, z_2, \dots, z_J\}$ .

Two simple partitioning methods are the interleaved partition, i.e.,  $X = \{t_1, t_3, t_5, \dots\}$ , and  $Z = \{t_2, t_4, t_6, \dots\}$ , and the block partition, i.e.,  $X = \{t_1, t_2, \dots, t_I\}$ , and  $Z = \{t_{I+1}, t_{I+2}, \dots, t_N\}$ . As stated in [30], both partitioning methods give similar performance.

Each element of  $\mathbf{L}^{(k)}$  is given by:

$$\ell_{i,j}^{(k)} = \frac{y_{k,x_i} - y_{k,z_j}}{x_i - z_j} \quad (7.2)$$

where  $i = 1, \dots, I$  and  $j = 1, \dots, J$ . Note that this construction is invariant to a vertical shift of the signal, i.e., the Löwner matrix built from signal  $\mathbf{y}_k$  is equal to the one built from  $\mathbf{y}'_k = \mathbf{y}_k + c$ , where  $c \in \mathbb{R}$  is a constant.

Next, the tensor is built by stacking each Löwner matrix along the third dimension (as frontal slices) of a third-order tensor  $\mathcal{Y}_L \in \mathbb{R}^{I \times J \times K}$ . Similarly to the Hankel counterpart, one can show that:

$$\mathbf{Y}_{..k} = \mathbf{L}^{(k)} = \sum_{r=1}^R m_{k,r} \mathbf{L}_{\mathbf{S}}^{(r)} \quad (7.3)$$

where  $\mathbf{L}_{\mathbf{S}}^{(r)} \in \mathbb{R}^{I \times J}$  is a Löwner matrix built from the  $r^{\text{th}}$  row of  $\mathbf{S}$ , similarly as in (7.1). One can see that the procedure for construction  $\mathbf{Y}_{..k}$  in (7.3) is a linear mapping and, for each  $r$ , the outer product between matrix  $\mathbf{L}_{\mathbf{S}}^{(r)}$  and the  $r^{\text{th}}$  column of  $\mathbf{M}$ , i.e.,  $\mathbf{m}_{..r}$ , is performed to build a third-order tensor containing the contribution of the  $r^{\text{th}}$  source to the ECG tensor. Putting together the contribution of all sources, the third-order tensor  $\mathcal{Y}_L$  admits a BTD tensor model and can be written as:

$$\mathcal{Y}_L = \sum_{r=1}^R \mathbf{L}_{\mathbf{S}}^{(r)} \circ \mathbf{m}_{..r} . \quad (7.4)$$

The Löwner-BTD suits the characteristics of VA in the ECG, since QRS complexes can be approximated by rational functions of low degree [30], [73], [38]:

$$s(t) = a(t) + \sum_{f=1}^F \sum_{d=1}^{D_f} \frac{c_{f,d}}{(t - p_f)^d} \quad (7.5)$$

where  $a(t)$  is a polynomial of degree  $A$ ,  $F$  is the number of  $p_f$  complex poles,  $D_f$  is the multiplicity,  $t$  is the continuous time, and  $c_{f,d} = 1/(u_f - v_d)$  are the scalar entries of a Cauchy matrix based on the vectors  $\mathbf{u} \in \mathbb{C}^F$  and  $\mathbf{v} \in \mathbb{C}^{D_f}$ , with  $u_f \neq v_d, \forall f, d$ . When mapped onto Löwner matrices, the degree of the rational function matches the rank of the matrix [30].

The experiments reported next assess the performance of the Löwner-BTD in two challenging scenarios typical of persistent AF.

### 7.2.2 Experimental data and setup

All the recordings belong to the PERSIST database and were preprocessed as described in Section 1.3. Experiments are performed in 10 different segments of ECG recordings from 10 different patients suffering from persistent AF, where 5 of these segments have a disorganized and/or weak AA, and the other 5 have very short RR intervals. In order to exploit all spatial diversity, while reducing the computational cost, only 8 independent leads are processed (I, II, V1-V6). The two type of segments used in the reported experiments are shown in lead II in Figure 7.1. The physiological characteristics of the observed 10-patient population are described on Table 7.1.

Table 7.1: Overall physiological characteristics of the 10-patient population.

Patient characteristics	$\mu \pm \sigma$	Min	Max
Age (years)	$61.1 \pm 11.1$	42	74
Height (cm)	$176.3 \pm 3.7$	170	184
Weight (kg)	$81.3 \pm 6.5$	68	92
AF History (months)	$86.5 \pm 66.6$	12	228
LA Diameter (mm)	$46 \pm 6.6$	36	56

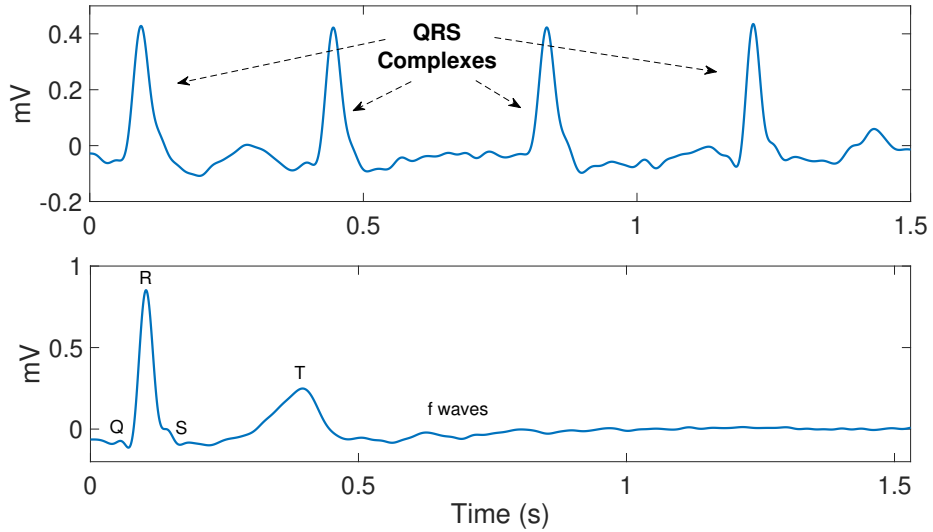


Figure 7.1: Top: A 1.5-second segment of an AF ECG recording with 4 QRS complexes from one patient (P2). The RR intervals are short and represented by the time difference between the peaks. Bottom: a single heartbeat segment of an AF ECG recording with a weak AA signal, from another observed patient (P6). Only bipolar limb lead II is shown for clarity, although the 8 independent leads (I, II, V1-V6) are processed in the experiments reported here.

The 5 segments with short RR intervals from 5 different patients (P1-P5) have 1.5 seconds of duration with at least 2 QRS complexes. The other 5 segments with disorganized and/or weak AA, from other 5 different patients (P6-P10), are composed by one heartbeat, i.e., the QRS complex followed by the T wave and the visible f waves, and have between 1.3-1.7 seconds. All the 10 segments are downsampled by a factor of 2, since the originally built third-order tensors pose some difficulties to be computed.

The BTD is implemented using the NLS approach with the Gauss-Newton method available in Tensorlab MATLAB toolbox [105]. For the Hankel-BTD, the choice  $R = 6$  and  $L_r = 48$ , for  $r = 1, 2, \dots, R$ , is made. The choice of  $R$  is based on the SVD of the observed data matrix, taking into account the most significant singular values. The choice of  $L_r$  is based on the work of [110] and [25], for the same reason previously explained.

For the Löwner-BTD, the choice  $R = \{2, 3\}$  and  $L_r = L$ , for  $r = 1, 2, \dots, R$ , with  $L$  taking values in the set  $\{3, 4, 5, 6\}$  is made. This choice is made based on previous experiments that aimed at estimating only the VA from the original recording, and then subtract it from the ECG, providing the signal with mainly AA content. Previous experiments show that the VA subspace is mainly present in the first 2 or 3 principal singular values of the ECG matrix, with low rank values.

For both techniques, the maximum number of iterations is set to 1000. Monte Carlo runs with Gaussian random initialization for the spatial and temporal factors ( $\mathbf{A}_r$ ,  $\mathbf{B}_r$  and  $\mathbf{c}_r$ , for  $r = 1, \dots, R$  in (4.43)) at each run are used to analyze the performance of BTD in each segment regarding the separation of VA from AA.

### 7.2.3 Segments with short RR intervals

Table 7.2 shows the values of SC in % of the estimated AA and the number of iterations until convergence of the NLS method for the Löwner- and Hankel-BTDs. The

Table 7.2: SC values (%) of the AA and the number of iterations (mean  $\pm$  standard deviation) of the NLS method for the Löwner-BTD (BTD-L) and the Hankel-BTD (BTD-H) in ten Monte Carlo runs.

Patients	BTD-L		BTD-H	
	SC (%)	Iterations	SC (%)	Iterations
P1	51.2	$60 \pm 18.1$	44.1	$185.7 \pm 47.2$
P2	54.6	$60.3 \pm 22.4$	33.8	$181 \pm 68.1$
P3	46.1	$46.7 \pm 15.4$	30.9	$164.9 \pm 58.1$
P4	63.5	$125.3 \pm 36.5$	61.9	$143.5 \pm 37.1$
P5	33.7	$44 \pm 16.9$	none	none
P6	60.1	$28.2 \pm 6.7$	none	none
P7	60.0	$29.9 \pm 11.5$	none	none
P8	52.9	$33.3 \pm 18.2$	none	none
P9	40.7	$35 \pm 12.8$	none	none
P10	56.9	$36.8 \pm 12.1$	none	none

best performance of the ten independent runs is shown. Patients P1-P5 correspond to the patients whose segments have short RR intervals. We can see in Table 7.2 that the SC of the AA, resulting from the subtraction of VA from the ECG, for the Löwner-BTD is always higher than the one estimated by the Hankel-BTD. Moreover, the mean of the number of iterations of the NLS method until convergence is always shorter, meaning that the proposed approach provides a better performance with less computational cost. In addition, the Löwner-BTD can separate the VA from AA in all the population of patients whose segments have a short RR intervals, while the Hankel-BTD cannot successfully separate them for patient P5. The DF of both tensor approaches lies in the interval  $5.48 - 7.15$  Hz, while the  $P(r)$  values of the Löwner-BTD lie in the interval  $7.2 \times 10^{-4} - 9.1 \times 10^{-3}$  mV<sup>2</sup>, which are consistently higher than the  $P(r)$  values of the Hankel one, in the interval  $5.7 \times 10^{-4} - 2.5 \times 10^{-3}$  mV<sup>2</sup>.

In Figure 7.2 we can see the observed segment of Patient P4, the only patient where the four signal processing techniques could successfully separate the sources. The proposed technique provides a signal with clearer AA content and a higher  $P(r)$  value than the other methods.

#### 7.2.4 Segments with disorganized and/or weak AA

For the patients whose segments are characterized by a very weak and/or disorganized AA contribution, the matrix-based methods and the Hankel-BTD could not clearly separate the sources. The AA signal was not identified due to its very weak content or, in some cases, significant VA residuals in the signal. For the Löwner-BTD, the AA signal was successfully separated from the VA with a relatively satisfactory performance, considering the nature of the recording.

In Table 7.2, patients P6-P10 correspond to the patients whose segments have disorganized and/or weak AA contribution. We can see that a relatively low number of iterations provide a satisfactory performance regarding the quality of AA content. The values of  $P(r)$  lie in the range of  $4.6 \times 10^{-4} - 1.7 \times 10^{-3}$  mV<sup>2</sup>, showing that each source has significant AA content, despite its weak contribution to the ECG recording.

In Figure 7.3 we can see the observed recording, as well as the estimated VA and AA of the processed segment of one of the patients in the observed population, for the

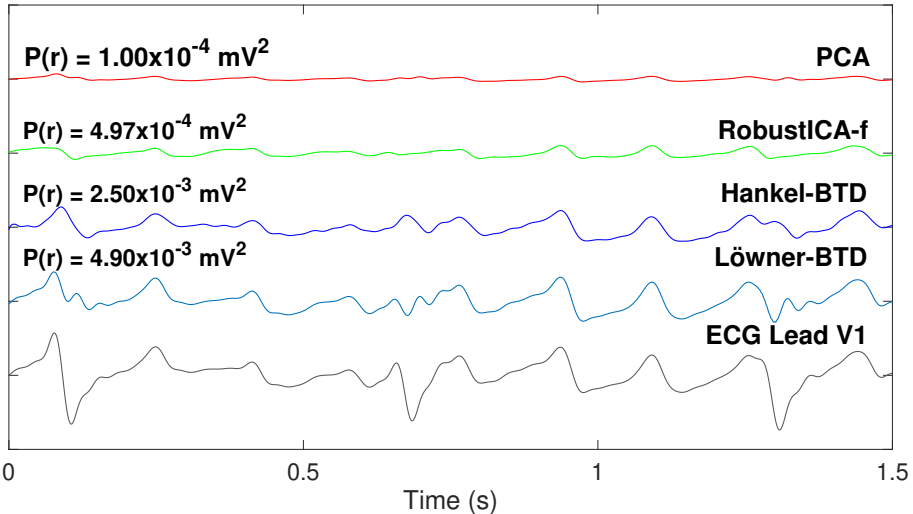


Figure 7.2: Estimated atrial sources contribution to lead V1 in a segment of short RR intervals of Patient P4 by Hankel- and Löwner-BTDs, RobustICA-f and PCA in the time domain. AA signal estimates are vertically shifted for clarity with their respective power contributions to lead V1.

best performance of ten Monte Carlo runs. The segments are shown in lead II for a better clarity of the estimated VA. It can be seen that even the T wave is estimated by the proposed method, that is, not only the ventricular depolarization, but also its repolarization are successfully modeled.

Regarding the performance of the matrix-based techniques, PCA could only successfully separate VA from AA in patient P4, with a SC of 55.4% and DF = 5.72 Hz, while RobustICA-f could only separate them in patients P1 and P4, with SCs and DFs equal to 40.7%/6.91 Hz and 60.8%/5.72 Hz, respectively. These outcomes demonstrate, once more, the superiority of tensor techniques over matrix approaches in AA extraction from AF ECGs.

### 7.3 Coupled block term decomposition

Coupled tensor decompositions have been gaining space in biomedical signal processing problems [49], [1]. Exploring the spatial and temporal diversity of ECG signals, the coupled BTD [98] built from Hankel matrices — called hereafter in this section coupled BTD — is now put forward as a novel noninvasive AA extraction method, modeling consecutive AF ECG segments, assuming that they share the same spatial signatures. To the best of the author’s knowledge, no coupled tensor approach has yet been applied to ECG signal processing. Also, this is the first time that the coupled BTD is used in a biomedical signal processing scenario. After presenting the coupled approach in Section 7.3.1, Coupled BTD is assessed in Section 7.3.2 in synthetic signals that simulate an AF ECG and validated in Section 7.3.3 in real ECG recordings from two patients suffering from persistent AF. In both scenarios, the coupled BTD is compared with the Hankel-BTD — called hereafter in this section just BTD — regarding the AA extraction performance and computational cost.

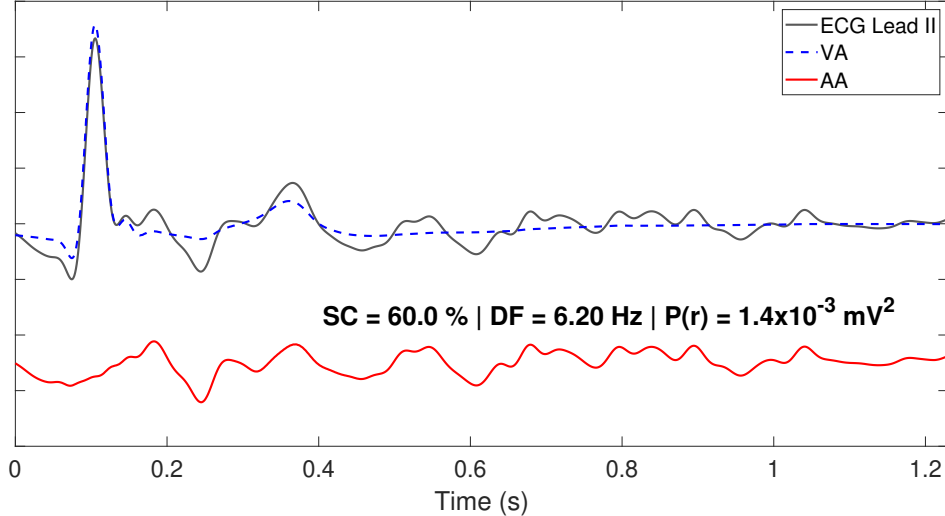


Figure 7.3: Original recording, VA and AA estimates in lead II by the Löwner-BTD of Patient P7. The AA signal is vertically shifted for clarity.

### 7.3.1 Model derivation

Recall that, for the particular case of AF ECGs, the third-order tensor  $\mathcal{Y}$  in (4.57) is the tensorization of the AF ECG data matrix  $\mathbf{Y}$  obtained by mapping each of its rows into a Hankel matrix and stacking them as frontal slices of  $\mathcal{T}$ . Matrices  $\mathbf{H}_S^{(r)}$  have a Hankel structure, built from each source of  $\mathbf{S}$ , and vectors  $\mathbf{c}_r$  represent each column of the mixing matrix  $\mathbf{M}$ .

Assuming that consecutive segments of an AF ECG recording from  $K$  leads composed by  $M$  time samples  $\mathbf{Y} \in \mathbb{R}^{K \times M}$  have the same spatial signature, i.e., the same mixing matrix (which implies the same number of sources), they can be modeled as coupled BTD tensors, sharing the same nonzero vectors  $\mathbf{c}_r$  [29]. So, dividing  $\mathbf{Y}$  in  $N$  consecutive segments of length  $M_n$ , where  $\sum_{n=1}^N M_n = M$ , the coupled BTDs can be given by:

$$\begin{aligned} \mathcal{Y}^{(1)} &= \sum_{r=1}^R (\mathbf{A}_{r,1} \mathbf{B}_{r,1}^T) \circ \mathbf{c}_r \\ &\vdots \\ \mathcal{Y}^{(N)} &= \sum_{r=1}^R (\mathbf{A}_{r,N} \mathbf{B}_{r,N}^T) \circ \mathbf{c}_r . \end{aligned} \quad (7.6)$$

Dividing an ECG recording in  $N$  consecutive segments divides the original tensor in  $N$  smaller tensors. For the case where the segments are of same length, the total number of scalar entries is reduced by a factor of  $\approx 1/N$ . Indeed, the number of scalar entries of the tensor build from the whole ECG recording is  $\approx (\frac{M}{2})^2 K$ , whereas each tensor with  $M_n = M/N$  samples has  $\approx (\frac{M}{2N})^2 K = \frac{1}{N^2} (\frac{M}{2})^2 K$  scalar entries. Since we have  $N$  smaller tensors, the total number of scalar entries to be processed is  $\frac{1}{N} (\frac{M}{2})^2 K$ .

Jointly processing the  $N$  third-order tensors is expected to reduce the computational cost, comparing as if they are processed separately. Also, the non-stationarity of AA signals during AF allows the exploitation of the temporal diversity, as the signals will be jointly estimated by the coupled tensor approach with different time signatures.

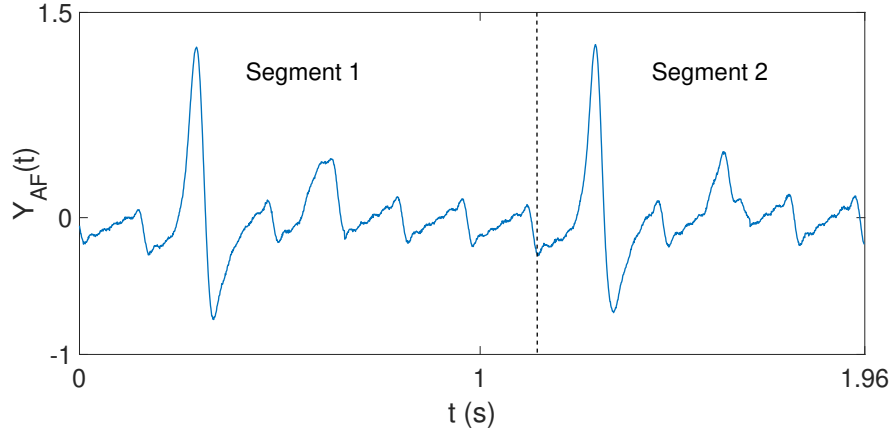


Figure 7.4: Generated synthetic signal modeling an ECG with AF patterns plotted in time domain, where  $t = m/F_s$  are the time values in seconds and  $Y_{AF}(t)$  is the amplitude.

For the particular case of ECGs, we have  $\mathbf{C} = \mathbf{M} \in \mathbb{R}^{K \times R}$ ,  $\mathbf{A}_{r,n} \in \mathbb{R}^{I_n \times L_{r,n}}$  and  $\mathbf{B}_{r,n} \in \mathbb{R}^{J_n \times L_{r,n}}$ , where  $I_n + J_n = (M_n + 1)$ . Hence, for the two necessary conditions presented in the end of Section 4.5, we have that:

1. A necessary condition for  $k_{\mathbf{C}} \geq 2$  to be satisfied is  $K \geq R \geq 2$ . This holds for the cases of AF ECGs, where, typically, the number of sources is smaller than the number of leads and greater than 2.
2. For matrix  $\mathbf{F}$  (4.52) to have full column rank it must fulfill  $\sum_{n=1}^N I_n J_n \geq R$ . We have that  $\sum_{n=1}^N I_n J_n \geq I_n J_n \geq M_n$ , for  $M_n \geq 2$ . Since for AF ECGs  $M_n \gg R > 2$ , the necessary condition holds.

In the next subsections, the coupled tensor approach is evaluated in synthetic and real data.

### 7.3.2 Evaluation on synthetic data

The performance of the coupled BTD for ECG source separation is now assessed in two consecutive synthetic AF segments by means of the NMSE between the estimated and original signals. The segments contain 3 sources: AA, VA, and a noise source.

To simulate the AA signal during AF, the model proposed in [101] presented in Section 1.3 is used. In order to simulate the VA signal, a synthetic T-wave modeled by a cosinus function [31] and three synthetic QRS complexes modeled by rational functions [4] were generated, as in Section 1.3. The noise signal that simulates the interference present in ECGs and the mixing matrix are also generated according to Section 1.3. The generated ECG data is divided in two consecutive segments as illustrated in Figure 7.4.

Coupled BTD is implemented using a straightforward strategy based on the NLS approach, which consists in computing the BTD for the first tensor and keeping the factor  $\mathbf{C}$  as known for the remaining tensors. BTD is implemented also using the NLS approach with the Gauss-Newton method, both available in Tensorlab MATLAB Toolbox [105], choosing  $R = 3$  and  $L_r = 17$ , for  $r = 1, 2, 3$ . The choice of  $R$  and  $L_r$  is based on previous experiments, guided by the work of [110]. The tolerance threshold for BTD convergence is set to  $10^{-9}$  and the maximum number of iterations is set to 1000. Ten Monte Carlo runs with Gaussian random initialization for the spatial and temporal factors at each run

Table 7.3: NMSE (dB) between the estimated and original AA sources for the coupled BTD and BTD.

Segments	Coupled BTD	BTD
1	-18.9	-15.4
2	-19.2	-13.5

are used to analyze the AA extraction performance of BTD and coupled BTD in each segment. The best out of the 10 independent initializations is chosen.

Table 7.3 shows the NMSE in dB between the estimated and original AA sources ( $\text{NMSE}_{\text{AA}}$ ) of segments 1 and 2, for coupled BTD and BTD. It can be seen that the AA sources of both segments are jointly estimated with a satisfactory performance for the coupled BTD, as confirmed by both NMSE values, which are lower than those provided by BTD. In addition, coupled BTD takes 281 iterations to converge to this solution, while BTD takes 283 and 150 iterations to provide a solution for segments 1 and 2, respectively, adding up to a total of 433 iterations. For the record, processing the BTD in the full segment with such configurations does not provide a satisfactory source separation, requiring the choice of higher  $L_r$  values. Still, the number of iterations to converge for the best solution out of ten Monte Carlo runs is 371.

### 7.3.3 Evaluation on real data

Now the evaluation of the coupled tensor approach in real AF ECG recordings is presented.

#### 7.3.3.1 Experimental data and setup

The real recordings belong to the PERSIST database (Section 1.3). Experiments are performed in 5 different segments of ECG recordings from 2 different patients suffering from persistent AF, where 3 of these segments belong to Patient 1, and the other 2 belong to Patient 2. In order to fully exploit the multi-lead diversity, the 12 leads are processed. For a better visualization of the AA, Figure 7.5 shows lead V1 of the two types of segments used in the reported experiments. The 3 consecutive segments from Patient 1 have 1.20, 0.75 and 0.97 seconds of duration, respectively. The other 2 consecutive segments from Patient 2 have both 1.13 seconds of duration. All the 5 segments are downsampled by a factor of 4 in order to reduce tensor dimensions and subsequent computational time, without increasing any loss of information.

Both tensor-based techniques are implemented with the same configuration as in the experiments with synthetic data reported in Subsection 7.3.2, just changing the value of the number of sources to  $R = 4$ , choice made based on preliminary experiments.

#### 7.3.3.2 Experimental results

Table 7.4 shows the values of SC in %,  $\kappa$ , and  $P(r)$  in mV<sup>2</sup> of the estimated AA signal by BTD and coupled BTD, for all the consecutive segments of both patients. The best performance out of the ten independent runs regarding AA estimation quality and source separation is shown.

We can see in Table 7.4 that for all the segments of both patients, coupled BTD provides a higher SC than BTD. For the parameters  $\kappa$  and  $P(r)$ , coupled BTD provides higher values than BTD in all but two segments. From this table one can conclude

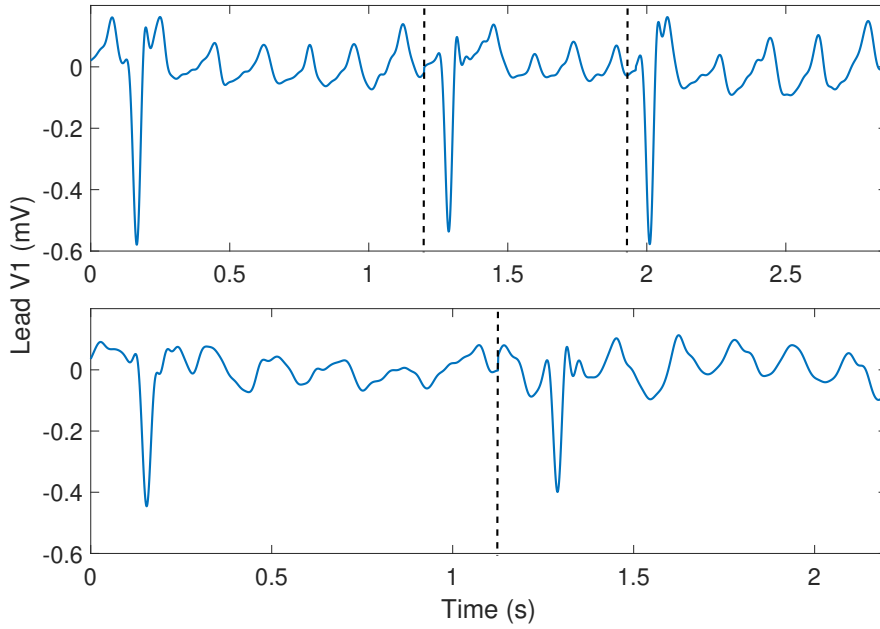


Figure 7.5: Top: the AF ECG recording of Patient 1 divided in three consecutive segments of different lengths. Bottom: the AF ECG recording of Patient 2 divided in two consecutive segments of same length. Only lead V1 is shown to ease visualization, although the 12 leads are processed in the experiments reported here.

that both coupled BTD and BTD provide satisfactory AA sources estimates, with a significant superiority of the coupled approach. However, the main advantage of the coupled approach is its ability to jointly estimate more than one segment with the same number of iterations as BTD takes to converge for a single segment, as it will be detailed later in this section.

In addition, when applying BTD to the whole recording, i.e., without dividing it into consecutive segments, the method cannot separate the sources with a low choice of  $L_r$  and the number of iterations until convergence easily exceeds 1000. This highlights even more the advantages of segmenting the recording, as the tensor approach can successfully extract the AA from short ECG recordings, whereas techniques based on QRST cancellation cannot. Indeed, such techniques presented in Chapter 3 require relative long recordings and are not operative in the short segments analyzed in this doctoral thesis. As an example, for ASVC, it is typically required a segment with duration longer than 30 s – 1 min [2].

Figure 7.6 illustrates the AA source estimates in the time and frequency domain for Patient 2. At the top it can be seen how the VA is well suppressed, as at the bottom the peak in a frequency between 3 and 9 Hz is clearly visible, typical of an AA source during AF. It is valid to state that the DF of the AA sources estimated by coupled BTD are exactly the same of the ones estimated by BTD, for all segments of both patients. This shows the consistency of the coupled approach, since BTD has already been validated as an AA extraction tool [26] (See Chapter 6 of this doctoral thesis).

Figure 7.7 compares the number of iterations to provide the best solution by both tensor-based techniques. Unlike coupled BTD, conventional BTD does not jointly estimate the source signals for all segments, so the sum of the number of iterations of

Table 7.4: Values of SC (%),  $\kappa$ , and  $P(r)$  in  $\text{mV}^2$  of the AA signal estimated by coupled BTD and BTD, for all the processed segments of both patients. The best solution out of ten Monte Carlo runs is chosen.

Coupled BTD	Patient 1			Patient 2	
	1	2	3	1	2
SC (%)	58.6	67.1	64.8	72.3	64.3
$\kappa$	138.8	94.3	143.8	138.6	207.8
$P(r) (\times 10^{-3})$	2.3	1.2	3.3	0.9	2.0
BTD	Patient 1			Patient 2	
	1	2	3	1	2
SC (%)	57.4	61.8	56.3	71.2	62.7
$\kappa$	94.4	95.4	98.4	155.7	196.7
$P(r) (\times 10^{-3})$	0.8	1.0	3.5	0.8	2.8

each segment is added to each other and shown in the graphs, which provides a number considerably higher, compared to the coupled approach. It is also observed that coupled BTD is less sensitive to initialization, as out of the 10 Monte Carlo runs, around 70% of solutions provided satisfactory source separation performance, whereas only around 50% of BTD solutions provided a satisfactory separation of the sources.

## 7.4 Summary

This chapter proposed two ECG tensor models to perform AA extraction for AF analysis. The first tensor model is based on the BTD built from Löwner matrices, focusing on the VA estimation for further cancellation from the ECG. This approach proves to be efficient in scenarios were the persistent AF patient presents short TQ segments and a weak/chaotic AA signal. The second tensor model assumes that consecutive segments share the same spatial signature, making it possible to jointly extract the AA signal from them. This approach provided a better performance than its non-coupled version, increased robustness to initialization of the computation algorithm and fewer iterations to converge for a satisfactory solution.

Existing algorithms require the prior knowledge of the tensor model structure ( $R, L_r$ ) in order to compute the BTD. Also, such algorithms are strongly dependent on the initialization and may not guarantee the structure of the matrix factors. Overcoming these limitations, a novel algorithm was recently proposed, being more robust to initialization and able to estimate the tensor model structure while searching for the matrix factors of BTD, with structured guaranteed by a linear projection. The next chapter will describe and assess this recently proposed algorithm for BTD computation in synthetic and real AF ECG recordings. Both Hankel and Löwner approaches are exploited.

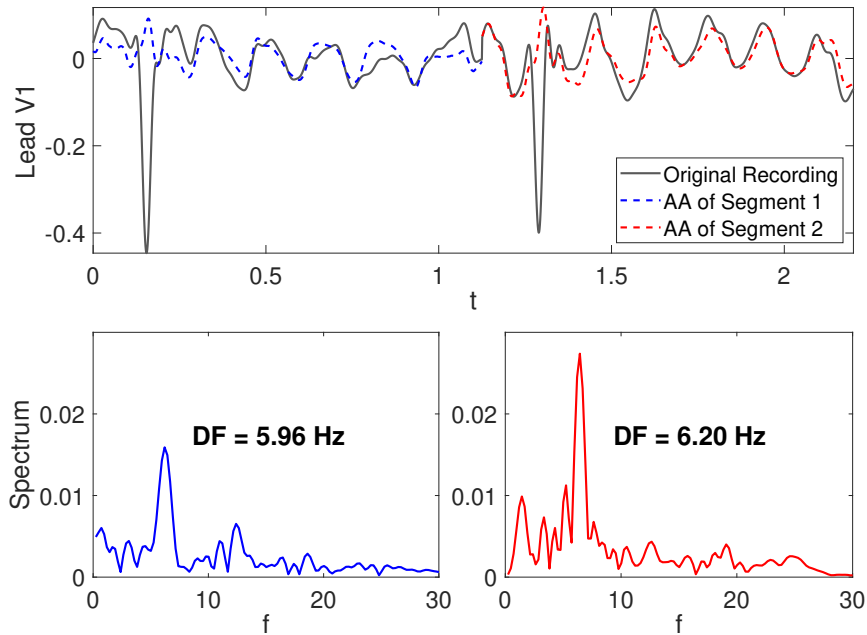


Figure 7.6: Estimated atrial sources in lead V1 on time (top plot) and frequency domain (bottom plots) of Patient 2 by coupled BTD.

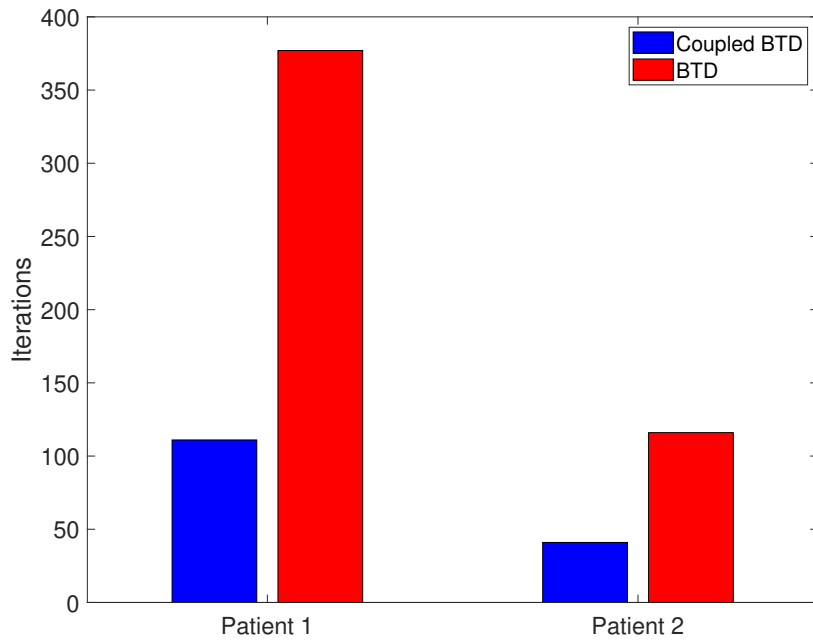


Figure 7.7: Number of iterations until convergence for both tensor-based methods.

## CHAPTER 8

# Improved Algorithms for BTD Computation

---

## Contents

<b>8.1</b>	<b>Introduction</b>	<b>89</b>
<b>8.2</b>	<b>Alternating group lasso and its constrained version</b>	<b>89</b>
8.2.1	Mathematical derivation	89
8.2.2	Experimental evaluation of CAGL as an AA extraction tool	91
<b>8.3</b>	<b>CAGL as an AF complexity measurement tool</b>	<b>97</b>
8.3.1	Database and experimental setup	98
8.3.2	Experimental Results	99
<b>8.4</b>	<b>Löwner-constrained alternating group lasso</b>	<b>100</b>
8.4.1	Mathematical derivation of LCAGL algorithm	101
8.4.2	Synthetic AF data	103
8.4.3	Real AF Database and Experimental Setup	103
<b>8.5</b>	<b>Summary</b>	<b>108</b>

---

## 8.1 Introduction

This chapter first introduces an improved algorithm, as compared to the state-of-the-art, to compute the BTD. Then, its Hankel- and Löwner-constrained versions are described and assessed as AA extraction tools. The Hankel-constrained version, in particular, is also proposed as a tool to measure AF complexity. The Löwner-constrained version is assured by an orthogonal projection detailed described in this doctoral thesis. This chapter yielded a journal publication and a submission under review:

- J. H. de M. Goulart, P. M. R. de Oliveira, R. C. Farias, V. Zarzoso, and P. Comon, “Alternating group lasso for block-term tensor decomposition and application to ECG source separation”, *IEEE Transactions on Signal Processing*, vol. 68, pp. 2682-2696, 2020.
- P. M. R. de Oliveira, J. H. de M. Goulart, C. A. R. Fernandes and V. Zarzoso, “Persistent atrial fibrillation analysis using a tensor decomposition with Löwner constraints”, submitted, 2020.

## 8.2 Alternating group lasso and its constrained version

### 8.2.1 Mathematical derivation

In general, an approximate BTD is computed by minimizing, in the least-squares sense, the distance between the observed data tensor  $\mathcal{Y} \in \mathbb{C}^{I \times J \times K}$  and a model of fixed

structure, defined by  $R$  and  $L_r$ , with respect to the model components, i.e.,

$$f(\mathbf{A}, \mathbf{B}, \mathbf{C}) \triangleq \left\| \mathcal{Y} - \sum_{r=1}^R (\mathbf{A}_r \mathbf{B}_r^T) \circ \mathbf{c}_r \right\|_F^2. \quad (8.1)$$

In the special case of AA extraction using Hankel-BTD,  $\mathbf{H}_r = \mathbf{A}_r \mathbf{B}_r^T$  must belong to the subspace of Hankel matrices with dimensions  $(I \times J)$ , denoted  $\mathcal{S}_H$ . The mode-3 slices  $\mathbf{Y}_{..k}$  of the observed tensor are Hankel by construction. However, a solution  $(\hat{\mathbf{A}}, \hat{\mathbf{B}}, \hat{\mathbf{C}})$  of (8.1) may not satisfy  $\hat{\mathbf{A}}_r \hat{\mathbf{B}}_r^T \in \mathcal{S}_H$ , due to noise and modeling imperfections. Note that even if the sum  $\sum_{r=1}^R (\hat{\mathbf{A}}_r \hat{\mathbf{B}}_r^T) \hat{\mathbf{c}}_{k,r}$  is Hankel, there is no guarantee that so are matrices  $\hat{\mathbf{A}}_r \hat{\mathbf{B}}_r^T$ . Also, most algorithms based on (8.1) are strongly dependent on the initialization of its matrix factors and do not estimate the model parameters, i.e., the number of blocks and their ranks.

In [42] the use of group sparsity for robust low-rank approximation of tensors is detailed studied, showing that the low rank decomposition problem can be solved without any knowledge of the true rank. More precisely, in [43] a novel robust method that imposes group sparsity is proposed to compute the CPD. Also, in [44], a functional promoting group sparsity of the decomposition factor columns was minimized to estimate appropriate structural parameters of an (unconstrained) BTD model, but not the model itself. Moreover, in [44] it is only considered the case where all  $L_r$  are equal.

Overcoming such limitations, instead of using a fixed BTD structure as (8.1), a technique called alternating group lasso (AGL) and its constrained version described for Hankel matrices called CAGL, are introduced in [20] and summarized next. This method includes penalization terms promoting low-rank blocks and controlling the number of blocks as:

$$F(\mathbf{A}, \mathbf{B}, \mathbf{C}) \triangleq f(\mathbf{A}, \mathbf{B}, \mathbf{C}) + \gamma g(\mathbf{A}, \mathbf{B}, \mathbf{C}) \quad (8.2)$$

where  $f(\cdot, \cdot, \cdot)$  is the same as in (8.1),  $\gamma > 0$  is a regularization parameter and  $g$  is a regularization function of the form:

$$g(\mathbf{A}, \mathbf{B}, \mathbf{C}) \triangleq \|\mathbf{A}\|_{2,1} + \|\mathbf{B}\|_{2,1} + \|\mathbf{C}\|_{2,1}. \quad (8.3)$$

Due to the geometric properties of the mixed  $\ell_{2,1}$ -norm, solutions where  $\mathbf{A}$ ,  $\mathbf{B}$  and  $\mathbf{C}$  have null columns (for sufficiently high  $\gamma$  values) will be induced, allowing us to automatically select the relevant low-rank blocks. This method is called group lasso and is a generalization of the lasso (least absolute shrinkage and selector operator) estimator principle [108].

Since problem (8.2) is nonconvex (and nonsmooth), but convex by blocks, a block coordinate descent (BCD) approach is employed [20]. BCD consists in partitioning the set of optimization variables and sequentially solving convex subproblems in each subset of variables, fixing the others.

Consider  $\hat{\mathbf{A}}^{(x-1)}$ ,  $\hat{\mathbf{B}}^{(x-1)}$  and  $\hat{\mathbf{C}}^{(x-1)}$  the estimates of  $\mathbf{A}$ ,  $\mathbf{B}$  and  $\mathbf{C}$ , respectively, obtained at iteration  $x-1$ . Fixing  $\mathbf{B} = \hat{\mathbf{B}}^{(x-1)}$  and  $\mathbf{C} = \hat{\mathbf{C}}^{(x-1)}$  in (8.2) the subproblem in  $\mathbf{A}$  of iteration  $(x)$  becomes [20]:

$$\min_{\mathbf{A}} \frac{1}{2} \|\mathcal{Y} - \mathcal{W}_{\mathbf{A}}^{(x)}(\mathbf{A})\|_F^2 + \gamma \|\mathbf{A}\|_{2,1} \quad (8.4)$$

where  $\mathcal{W}_{\mathbf{A}}^{(x)}$  is a linear map that depends on  $\hat{\mathbf{B}}^{(x-1)}$  and  $\hat{\mathbf{C}}^{(x-1)}$ .

Subproblem (8.4) is now convex, but it may not be strictly convex, since  $\mathcal{W}_{\mathbf{A}}^{(x)}$  may not be injective at some iterations. This can be solved by adding a proximal term, so the

Hessian of the LS term becomes positive definite [20]. Subproblem (8.4) can be written now as:

$$\min_{\mathbf{A}} \frac{1}{2} \|\mathcal{Y} - \mathcal{W}_{\mathbf{A}}^{(x)}(\mathbf{A})\|_F^2 + \gamma \|\mathbf{A}\|_{2,1} + \frac{\tau}{2} \|\mathbf{A} - \hat{\mathbf{A}}^{(x-1)}\|_F^2 \quad (8.5)$$

where  $\tau$  is positive.

Analogously, strictly convex subproblems can be derived for  $\mathbf{B}$  and  $\mathbf{C}$ . AGL solves these subproblems alternatively, through the updates of  $\hat{\mathbf{A}}^{(x)}$ ,  $\hat{\mathbf{B}}^{(x)}$  and  $\hat{\mathbf{C}}^{(x)}$ , in this order, at each iteration  $x$ . When all subsets are updated, one iteration of the algorithm is completed.

In order to ensure the Hankel structure of the matrix factors at the end of iterations, a structured low-rank approximation (SLRA) is applied at each iteration of AGL, yielding CAGL. For this purpose, the Cadzow's Algorithm [8] is used at the end of the iterations, which consists in performing alternating projections onto the Hankel subspace  $\mathcal{S}_H$ , so that  $\hat{\mathbf{H}}_r \approx \hat{\mathbf{A}}_r \hat{\mathbf{B}}_r^T \in \mathcal{S}_H$ .

Table 8.1: Pseudocode for CAGL algorithm [20].

<b>Inputs:</b>	Data tensor $\mathcal{Y}$ , penalty parameter $\gamma$ , proximal term weight $\tau$ , initial point $(\mathbf{A}^{(0)}, \mathbf{B}^{(0)}, \mathbf{C}^{(0)})$
<b>Outputs:</b>	Approximate BTD factors $(\mathbf{A}, \mathbf{B}, \mathbf{C})$
1:	$x \leftarrow 1$
2:	<b>while</b> stopping criteria not met <b>do</b>
3:	Solve group lasso subproblem (8.5) to obtain $\mathbf{C}^{(x)}$ from $\mathbf{A}^{(x-1)}$ , $\mathbf{B}^{(x-1)}$ and $\mathbf{C}^{(x-1)}$
4:	Solve group lasso subproblem in $\mathbf{B}$ analogous to (8.5) to obtain $\mathbf{B}^{(x)}$ from $\mathbf{A}^{(x)}$ , $\mathbf{B}^{(x-1)}$ and $\mathbf{C}^{(x-1)}$
5:	<b>for</b> $r = 1, \dots, R$ <b>do</b>
6:	$L_r^{(x)} \leftarrow \text{rank} \left( \mathbf{A}_r^{(x)} (\mathbf{B}^{(x)})_r^T \right)$
7:	$(\mathbf{A}_r^{(x)}, \mathbf{B}_r^{(x)}) \leftarrow \text{slra}(\mathbf{A}_r^{(x)} (\mathbf{B}^{(x)})_r^T, L_r^{(x)})$
8:	$(\mathbf{A}_r^{(x)}, \mathbf{B}_r^{(x)}) \leftarrow ([\mathbf{A}_r^{(x)} \mathbf{0}_{I \times L - L_r^{(x)}}], [\mathbf{B}_r^{(x)} \mathbf{0}_{I \times L - L_r^{(x)}}])$
9:	Solve group lasso subproblem in $\mathbf{C}$ analogous to (8.5) to obtain $\mathbf{C}^{(x)}$ from $\mathbf{A}^{(x)}$ , $\mathbf{B}^{(x)}$ and $\mathbf{C}^{(x-1)}$
10:	$x \leftarrow x + 1$

The CAGL algorithm is summarized in Table 8.1, where **slra** denotes the SLRA algorithm and symbol  $(\cdot)$  is removed from the computed estimates, for simplification and clarity. It should be noted that for the unconstrained AGL algorithm, lines 5-8 must be removed.

Note also that each application of **slra** re-estimates both  $\mathbf{A}_r$  and  $\mathbf{B}_r$ . Finally, one should note that, since  $\hat{\mathbf{A}}_r^{(x)}$  and  $\hat{\mathbf{B}}_r^{(x)}$  always have  $L$  columns, zeros must be added in those blocks after applying **slra** (line 8).

### 8.2.2 Experimental evaluation of CAGL as an AA extraction tool

The usefulness of CAGL for ECG source separation in AF episodes is now assessed through experiments with semi-synthetic AF data models and real AF ECGs.

#### 8.2.2.1 Semi-synthetic AF data

To simulate AA during AF, the model proposed in [101], which is described in Section 1.3, is used. It is first considered a scenario with one AA source, generated accord-

Table 8.2: Parameters of the synthetic AA signal model of (1.1).

Model	P	a	$\Delta a$	$f_a$	$F_s$	$f_0$	$\Delta f$	$F_f$
1	5	150	50	0.08	1000	6	0.2	0.10
2	3	60	18	0.50	1000	8	0.3	0.23

ing to (1.1) with the parameters of Model 1 in Table 8.2. This signal is illustrated in Fig. 8.1(a). A random spatial signature  $\mathbf{x} \in \mathbb{R}^{12}$  over the 12 ECG leads is generated for this source, having standard normal independent and identically distributed components. The VA source is taken from a real standard 12-lead ECG of a healthy subject, after P wave suppression as in [87]. This ECG, which belongs to the Physionet database [40], is acquired at a sampling rate of 1 kHz and is preprocessed by a zero-phase forward-backward type-II Chebyshev bandpass filter with cutoff frequencies of 0.5 and 30 Hz, in order to suppress high-frequency noise and baseline wandering. AWGN with variance  $\sigma^2$  is added to simulate some perturbations typically present in ECG signals. The overall semi-synthetic AF ECG model is given by:

$$\mathbf{Y} = \mathbf{V} + \alpha \mathbf{x}\mathbf{s}^T + \mathbf{N} \in \mathbb{R}^{12 \times N} \quad (8.6)$$

where  $\mathbf{V}$  represents the normalized VA signal,  $\mathbf{s} \in \mathbb{R}^N$  is the AA signal,  $\mathbf{N}$  represents the AWGN and  $\alpha = 2$  is a scaling factor chosen to obtain an average atrial-to-ventricular power ratio consistent with clinical observations. An observation window of around 1.2 seconds is used, yielding 1221 samples. The overall generated AF signal is illustrated in Fig. 8.1(b) (dashed line). Mapping each ECG lead into a Hankel matrix and stacking them alongside the third-mode, yields a tensor of dimensions  $611 \times 611 \times 12$ . Since an approximate BTD of a tensor of such dimensions demands a large computing time, the signals are downsampled by a factor of 10 before computing the decomposition, yielding a resulting tensor  $\mathcal{Y}$  with dimensions  $62 \times 62 \times 12$ .

CAGL is run from an initial random solution and using  $\gamma = \gamma_0$  as penalization factor in 8.2. The value of  $\gamma_0$  is chosen empirically. For the  $p = 1, \dots, P - 1$  solution, CAGL is run with  $\gamma = \gamma_p = (p + 1)\gamma_0$  using the solution obtained for  $p - 1$  as the initial point. In this scenario,  $\gamma$  takes 30 equispaced values in the interval  $[8 \times 10^{-4}, 0.33 \times 10^{-2}]$  and the last solution is kept. For  $\gamma_0$ , the algorithm starts from random blocks, with the initial guess of  $R = 6$  and  $L = 40$ . Among the estimated sources, the AA source is chosen as the one that maximizes (in absolute value) the correlation coefficient  $\rho$  with respect to the ground-truth AA source.

The NLS approach with the Gauss-Newton method from Tensorlab (BTD-NLS) is setup with  $R$  blocks of fixed rank  $L$ , for all combinations  $(R, L) \in \{4, 5, 6\} \times \{1, \dots, 40\}$ . For each rank  $L$ , the initial point is generated by filling the  $L$  columns of  $\mathbf{A}_r$  and  $\mathbf{B}_r$  with the first  $L$  columns used to initialize these variables in CAGL.

This procedure is repeated 30 times for each of 10 different realizations of  $(\mathbf{x}, \mathbf{N})$ . It is observed that CAGL is more robust to initialization, as it produces results with very similar estimates regardless of the chosen initial point. Particularly, for 95% of the runs, the final number of estimated blocks is 4. By contrast, the results obtained with BTD-NLS are much more sensitive to initialization. Specifically, the value of  $L$  that yields the best performance for a given run is not the same across different runs, as illustrated by the empirical cumulative distribution function (ECDF) in Fig. 8.2(a). For CAGL, the rank chosen for the AA source block is almost always 10 as also shown in Fig. 8.2(a).

Even though the most suitable choice for BTD-NLS seems to be  $R = 4$  and  $L \in \{10, \dots, 15\}$ , its performance is highly variable for this range of  $L$ . This is observed

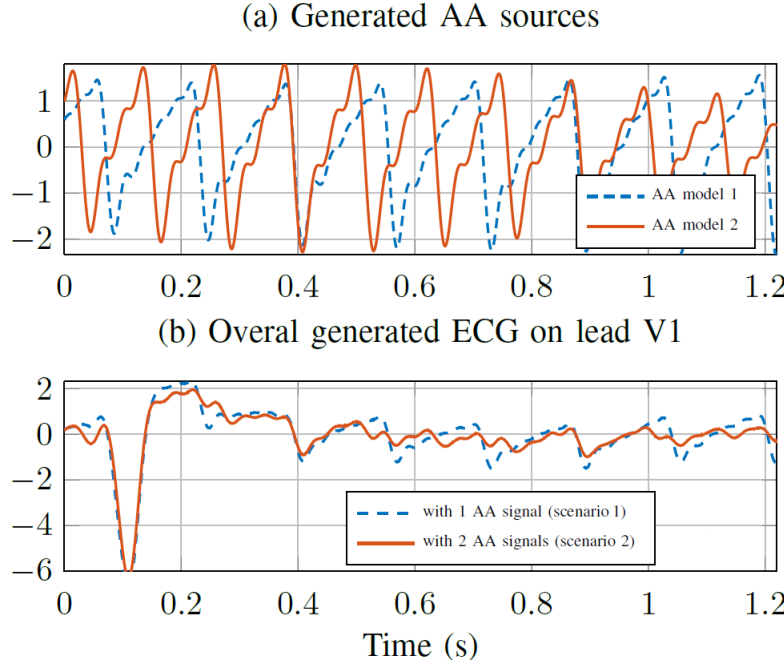


Figure 8.1: Examples of generated semi-synthetic models: (a) AA sources generated as (1.1) with the parameters shown in Table 8.2; (b) overall semi-synthetic ECG signals in lead V1.

in Fig. 8.3(a), which displays the histogram of the correlation coefficient  $\rho$  (in absolute value) between the estimated AA source and the ground-truth. All results produced by BTD-NLS for  $L \in \{10, \dots, 15\}$ , and all results produced by CAGL are included. One can see that the choice of  $R$  significantly affects performance, and a large proportion of results given by BTD-NLS achieves a poor  $\rho$  for every  $R$ . By contrast,  $\rho$  is very likely to be quite close to 1 for CAGL.

To sum up, BTD-NLS only produces good results with a suitable combination of its model parameters ( $R, L$ ) and initialization. By contrast, CAGL only requires the choice of a reasonable range for its penalization term ( $\gamma$ ) and behaves much more robustly with regard to initialization.

Now, it is considered a scenario with two AA sources. In this scenario, the VA source is still the same as in the previous scenario, but now two AA sources are generated, each one using the parameters of one row in Table 8.2. These AA signals are illustrated in Fig. 8.1(a). Accordingly, the model now is given by:

$$\mathbf{Y} = \mathbf{V} + \mathbf{X}\mathbf{S}^T + \mathbf{N} \in \mathbb{R}^{12 \times N} \quad (8.7)$$

where the columns of  $\mathbf{S} \in \mathbb{R}^{N \times 2}$  contain the AA signals and those of  $\mathbf{X} \in \mathbb{R}^{12 \times 2}$  contain their respective spatial signatures. All signals are again downsampled by a factor of 10, yielding data tensors with the same dimensions as before. Fig. 8.1(b) displays one example of the overall generated ECG signal (solid line).

CAGL and BTD-NLS are run following the same procedure as in the previous scenario (with one AA source). However, now the AA source estimates are extracted by choosing first the block with the highest correlation coefficient, in absolute value, with one of the ground-truth AA sources, and secondly the block maximizing the correlation with the remaining AA source.

The corresponding results are shown in Fig. 8.2(b) and Fig. 8.3(b). The conclusions are similar to the previous scenario, with three main differences in terms of model

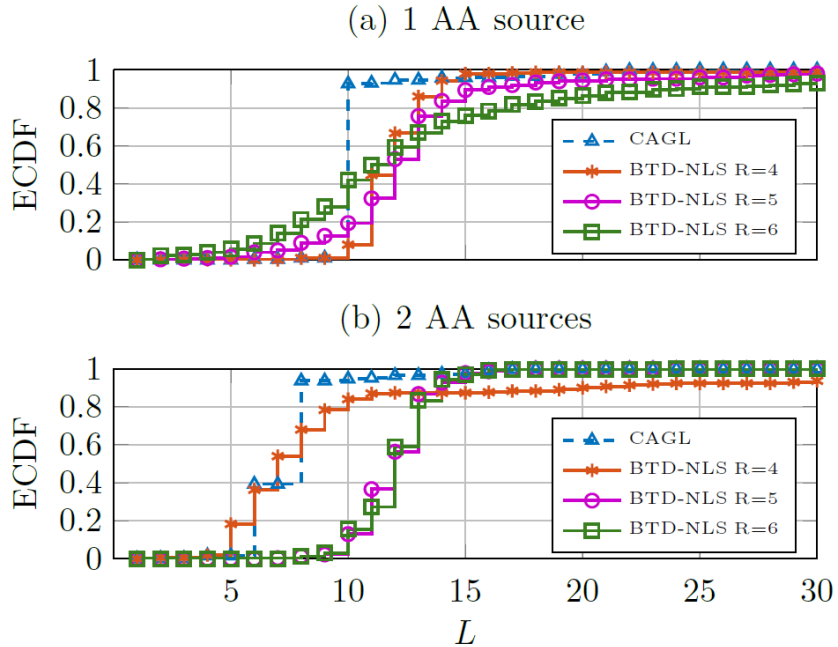


Figure 8.2: ECDF of rank chosen by CAGL for the AA source and of rank  $L$  yielding the best AA extraction for BTD-NLS with different numbers of blocks  $R$ . The curves are shown only up to  $L = 30$ , for clarity.

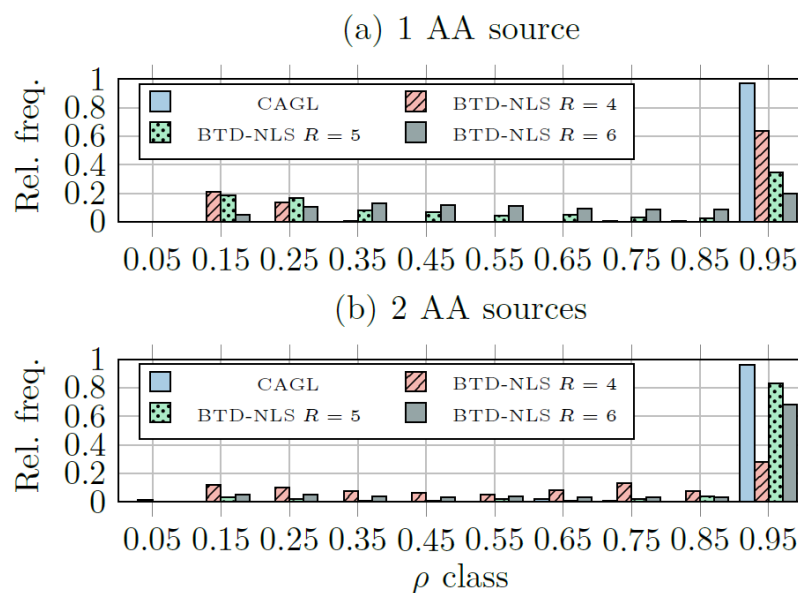


Figure 8.3: Histogram of computed correlation coefficient  $\rho$  (in absolute value) between ground-truth and estimated AA sources by both algorithms.

Table 8.3: Block ranks of the ECG sources extracted by CAGL and characteristics of the potential AA sources.

Patient	Non-AA source ranks	AA source	SC (%)	DF (Hz)	$\hat{\kappa}$	AA source rank
1	3, 9, 10, 16, 18	1	80.23	6.44	163.69	8
2	28, 32	1	59.36	6.20	116.77	29
		2	82.05	6.20	163.77	12
3	21, 27, 29	1	66.13	6.20	132.29	20
4	8, 16, 20	1	74.51	5.96	196.16	10
5	32, 38, 39	1	91.70	5.72	348.42	10
		2	78.63	5.01	166.95	21

structure recovery:

- BTD-NLS now performs best with  $R = 5$  instead of  $R = 4$ , which is expected since two atrial sources are now present, thus yielding richer AA content.
- For  $R = 5$ , BTD-NLS performance is closer to that of CAGL.
- Two choices of rank are most often made by CAGL (rather than one), namely  $L_r = 6$  and  $L_r = 8$ .

It is important to highlight that CAGL is run following exactly the same procedure as in the previous scenario. By contrast, BTD-NLS now yields best results with a different choice of  $R$ . This emphasize the fact that CAGL can effectively adapt to a given dataset, typically behaving more stably than the usual approach across different circumstances.

### 8.2.2.2 Real AF data

In order to validate CAGL as an AA extraction tool, experiments with real standard 12-lead ECG recordings from a population of five patients suffering from persistent AF are performed in this section. These recordings belong to the PERSIST database and are preprocessed as described in Section 1.3. For each patient, the heartbeat with the largest TQ segment is chosen for the experiment, making the recordings lengths range from about 1.08 to 1.40 seconds.

As in the previous experiments with semi-synthetic data, all signals are downsampled by a factor of 10, decreasing computing cost, with practically no information loss. After normalization of each signal tensor, CAGL is applied using the same  $\gamma$ -sweeping strategy as before. However, in this scenario with real data the final solution is chosen by inspection of the separated signals (i.e., from all solutions CAGL provided, the best is chosen), as the ground truth is unknown.

To assess AA estimation quality, two performance parameters described in Chapter 5 are employed: SC (in %) and kurtosis ( $\kappa$ ).

Table 8.3 shows a quantitative assessment of the potential AA sources extracted for each patient, while Fig. 8.4 illustrates the estimated overall and AA signals for each patient along with the observed signals. In all experiments, we have chosen the initial model parameters  $(R, L) = (6, 40)$ , which was sufficient to produce satisfying results. Note that, for Patients 2 and 5, two blocks were identified as potential AA sources; accordingly, the estimated AA signals in Fig. 8.4(b) and Fig. 8.4(e) are given by the linear combinations of these blocks multiplied by their corresponding spatial weights for

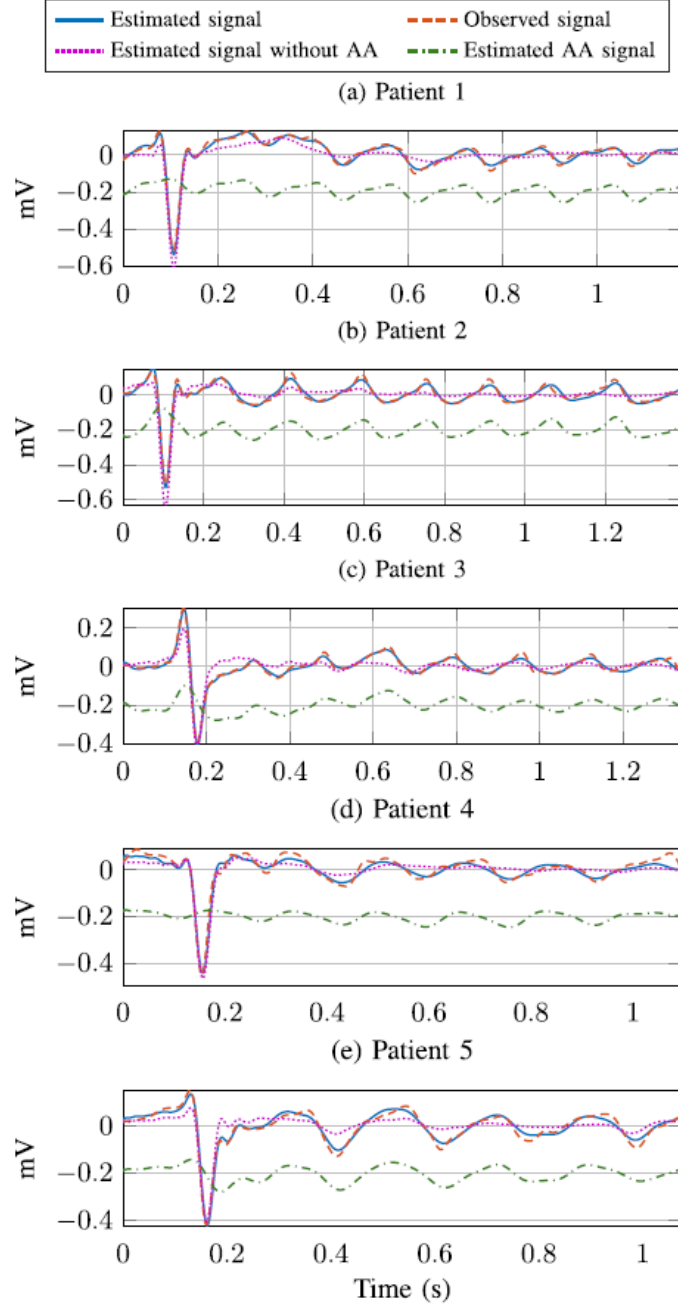


Figure 8.4: Results produced by CAGL with real ECGs: observed and estimated signals on lead V1. The estimated AA signals are vertically shifted by  $-0.2$  mV for clarity.

lead V1. These distinct potential AA sources for Patients 2 and 5 are shown in Fig. 8.5, along with their respective spatial weights (i.e., their associated columns in  $\mathbf{X}$ ). The shown signals are normalized as  $[\max_n |s_r(n)|]^{-1} s_r(n)$ , and the corresponding spatial weights are then rescaled so as to absorb the factor  $\max_n |s_r(n)|$ . Based on the results of Table 8.3 and Fig. 8.4, it is seen that a satisfying extraction is achieved, as the potential AA sources have typical f-wave features, relatively high SC and physiologically plausible DF between 5 and 6.5 Hz.

Regarding Patient 2, the values of SC and  $\hat{\kappa}$  for its AA source 1 are not so high due to the residual of the T-wave (ventricular repolarization), which can be seen around 0.3 seconds of Fig. 8.5(a). Furthermore, Fig. 8.5(b) shows that the contribution of AA source 2 decays along the path V1–V2–V3, which suggests that this source may reflect electrical activity mainly occurring in the right atrium, and is almost null on other leads. By contrast, AA source 1 gives significant contributions to most leads, which suggests that the associated electrical propagation pattern may be harbored in a region including both atria. In fact, these sources have very different spatial signatures: the cosine of the angle between their respective columns of  $\mathbf{X}$  is around  $-0.13$ , and so they are far from being collinear. Furthermore, despite having the same DF, their observed power spectra are considerably different. The lack of temporal synchronization between the estimated atrial sources, as manifested by the time lag between the maxima of the two signals plotted in Fig. 8.5(a), further supports the hypothesis that the associated activities may arise from different areas of atrial tissue.

Patient 5 provides another example in which two potential AA sources with considerably different spatial signatures are extracted: their respective columns in  $\mathbf{X}$  form an angle whose cosine is about 0.09. Moreover, the dominant frequencies computed for these sources also differ significantly: 5.72 for AA source 1 and 5.01 for AA source 2. Here, it is AA source 2 that exhibits significant contributions to most leads, while AA source 1 manifests itself mostly on lead V1 and thus may correspond to more localized electrical activity taking place in the right atrium.

While the possibility of extracting more than one atrial source presents great interest for the noninvasive analysis of AF, a thorough validation of this result would be required by means of ground truth data such as a full electroanatomical mapping of the atria performed, for instance, during catheter ablation interventions. Such a validation is out of the scope of the present doctoral thesis.

A final important observation is that for all but one patient, the sum of the estimated block ranks exceeds the dimension of the Hankel matrices ( $M \times M$ ): for Patient 1,  $\sum_r L_r = 64 > M = 63$ ; for Patient 2,  $\sum_r L_r = 101 > M = 74$ ; for Patient 3,  $\sum_r L_r = 97 > M = 71$ ; and for Patient 5,  $\sum_r L_r = 140 > M = 58$ . This corroborates the practical importance of the case where  $\sum_r L_r$  exceeds all tensor dimensions. Furthermore, for all patients the sum of block ranks far exceeds the number of leads, i.e.,  $\sum_r L_r > K$ , which showcases the benefit of using a tensor method, since a matrix decomposition approach could not possibly identify all the poles constituting each model.

### 8.3 CAGL as an AF complexity measurement tool

Step-wise catheter ablation (CA) is an effective therapy to treat persistent AF and restore sinus rhythm [57]. Hence, methods to measure AF complexity at each procedural step are relevant to improve clinical analysis and guide CA in real time. Furthermore, it would be desirable to clarify the impact on AF of each intervention step such as pulmonary vein isolation (PVI) and other widely used techniques [41], [92]. Due to the

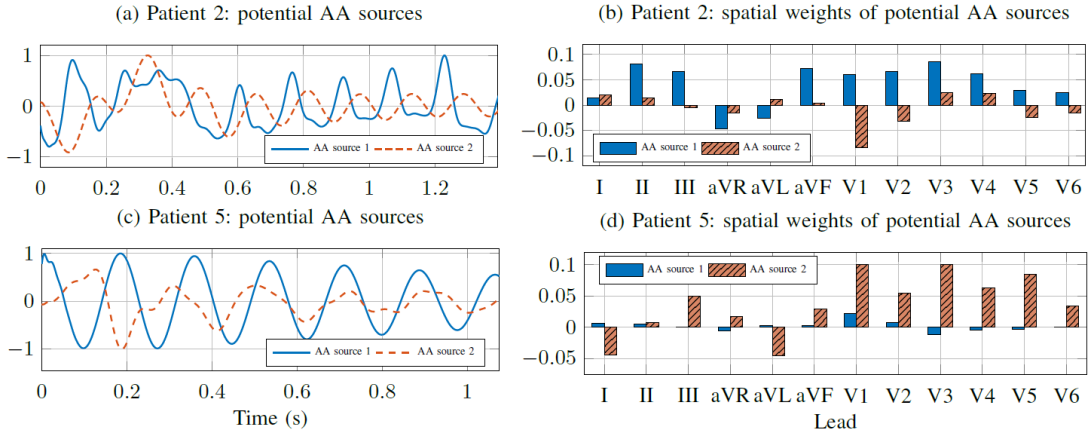


Figure 8.5: Estimated AA sources produced by CAGL with ECG data from Patients 2 and 5.

cost-efficiency of the ECG, the interest in noninvasive techniques to assess AF electrophysiological complexity is increasingly high. However, existing methods for noninvasive quantification of AF complexity are limited due to the fact that sufficiently long ECG recordings are required, hindering their use in clinical practice.

The complexity of a signal constructed from complex exponential sums is intrinsically related to the number of poles. Since the tensor block correlated with the AA signal presents a Hankel structure, the rank of its matrix factor  $L_r$  is equal to the number of poles [110]. Therefore, the proposed index is measured from the rank of the block that represents the atrial source, that allows a more global view of what goes on in the atria, while a catheter provides more local information. Since CAGL is able to estimate the rank  $L_r$  of each matrix factor, it is now proposed as a noninvasive tool to quantify AF complexity.

### 8.3.1 Database and experimental setup

Experiments with a database of 59 ECG recordings from 20 patients suffering from persistent AF (Section 1.3) show that CAGL is able to quantify AF complexity from very short ECG recordings. All the patients had undergone step-wise catheter ablation (CA) that ended in AF termination. The physiological characteristics of the observed 20-patient population are described on Table 8.4. It must be reported that there are missing data values for one patient regarding AF history and LA diameter and such values were replaced by the average.

Table 8.4: Overall physiological characteristics of the 20-patient population .

Patient characteristics	$\mu \pm \sigma$	Min	Max
Age (years)	$60.6 \pm 9.4$	42	76
Height (cm)	$177.8 \pm 6.2$	169	195
Weight (kg)	$85.6 \pm 12.7$	64	105
AF History (months)	$68.6 \pm 59.6$	3	228
AF Episode (months)	$16.3 \pm 25.2$	0.5	86
LA Diameter (mm)	$45.8 \pm 7.9$	33	62

The segment with the largest TQ segment is chosen for each patient, length ranging

from 0.72 to 1.42 seconds. A window with length 1.06 s, yields 1037 samples, a direct row-Hankelization of this matrix results in a tensor of dimensions  $519 \times 519 \times 12$ , whose approximate BTD demands a large computing time. Therefore, the signals are downsampled by a factor of 10 before applying the decomposition, in order to reduce its computing time, with practically negligible information loss. In this example, the resulting tensor  $\mathcal{Y}$  have dimensions  $52 \times 53 \times 12$ .

CAGL is applied to ECG recordings after each CA step, with a  $\gamma$ -sweeping procedure, inspired by solution-path techniques, by taking 50 equispaced values in the interval  $[8 \times 10^{-4}, 0.5 \times 10^{-2}]$  and keeping the last solution. The algorithm starts with  $R = 6$  random blocks and rank  $L_r = 40$  as initial guesses [20]. The task of measuring estimation quality is challenging since the ground truth is unknown. Nevertheless some AA characteristics during AF must be exploited to guide sources selection. The parameters used to evaluate AA extraction are spectral concentration (SC), dominant frequency (DF) and kurtosis as well as visual inspection, as detailed in [26], [24], [112].

### 8.3.2 Experimental Results

#### 8.3.2.1 AA complexity influence by PVI

The impact of CA at each step on AA complexity is assessed in terms of rank estimation by CAGL in the whole dataset. Before CA, ranks range from 12 to 33, whereas after all steps of the CA procedure, ranks range from 6 to 16, referred to, respectively, as ‘Initial’ and ‘Outcome’ in Figure 8.6. Initially, the population present a median rank 21.5, while at intermediaries steps is 15 and after CA it becomes 10.5, illustrating that the rank decreases at each step of the CA procedure as shown in Figure 8.6.

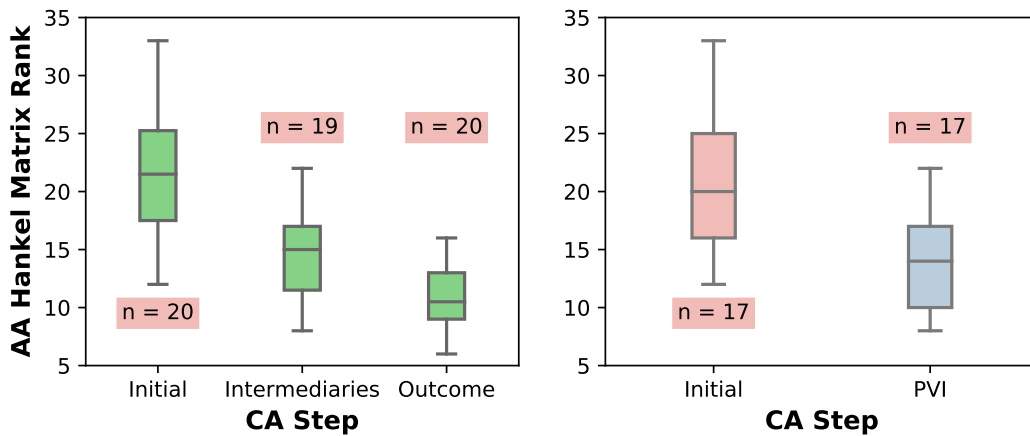


Figure 8.6: Right: Boxplot showing the rank estimated by CAGL for all patients at different CA steps: initial (before ablation); intermediaries (CA between the first and penultimate steps); outcome (after the last CA step). Left: Boxplot at the beginning of CA and after PVI for the group of 17 patients who underwent this CA step. Notation (n) indicates the number of ECG segments considered in each box.

In observed segments, the rank of extracted AA sources becomes less complex as the ablation is performed as one could intuitively expect. In addition, a separate assessment of the 17 patients undergoing PVI is also shown in Figure 8.6, presenting a drastic reduction of the proposed index after this CA step, from a median value of 20 to 14.

### 8.3.2.2 AF recurrence and complexity

To assess the relationship between population's features, Pearson correlation ( $r$ ) between the initial rank estimated by CAGL, *i.e.*, before any patient had undergone CA procedure, and AF recurrence, *i.e.*, the time that each patient remained in sinus rhythm before AF relapse is  $-0.63$ . A statistical relevant value of negative correlation well illustrated by its scatter plot and linear regression in Figure 8.7, seems to indicate an influence of initial rank on AF recurrence.

Finally, 2 patients registered ranks 12 and 18 but had no information about AF recurrence after the CA procedure, since they dropped out of the study. Hence, they were excluded from this assessment.

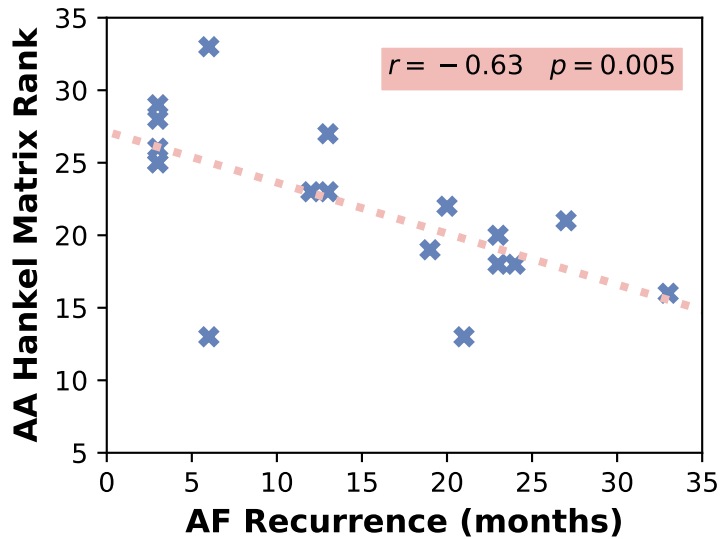


Figure 8.7: Scatter plot of the initial estimated rank (before CA) of the tensor block that provides the AA signal versus AF recurrence. A negative correlation can be observed.

## 8.4 Löwner-constrained alternating group lasso

It is now presented a Löwner-constrained version of AGL along with a significant extension of the previous results reported in Chapter 7. Indeed, an improved method to compute the Löwner-BTD is provided, together with more relevant results, by increasing the size of the AF patient database. This section formulates an orthogonal strategy for CAGL that deals with Löwner constraints, imposing a low-rank Löwner structure. The strategy is explicitly described as an orthogonal projection in the Löwner subspace, used to guarantee the specified structure in the matrix factors. The Löwner-constrained AGL (LCAGL) is compared to the Löwner-BTD computed with the NLS method (used in previous experiments reported in Chapter 7), as well as the recently proposed CAGL, dealing with Hankel constraints.

In order to ensure the Löwner structure of the matrix factors at the end of iterations, a formulation to deal with Löwner constraints in CAGL, called here LCAGL, is proposed. It should be noted that LCAGL follows the same principle of CAGL, which is to ensure a specified structure over the block matrices. However, instead of using a projection on the Hankel subspace as described in [20], LCAGL uses a linear projection on the Löwner subspace that will be detailed here.

The Löwner constraints can be enforced by solving a SLRA problem for each block matrix at each iteration of LCAGL. For this purpose, it is used the Cadzow's Algorithm at the end of each iteration. Cadzow's Algorithm perform alternate projections, where the one that leads to the set of matrices with rank up to  $L_r$  is performed by the truncated SVD, whereas the one that leads to the Löwner subspace is formulated in the following. It is important to highlight that, in practice, the rank of the matrices in the first projection is computed by counting the number of simultaneously nonzero columns of  $\mathbf{A}_r$  and  $\mathbf{B}_r$ .

#### 8.4.1 Mathematical derivation of LCAGL algorithm

It is considered here signals with an even number of samples, i.e.,  $I = J = N/2$ , and the interleaved partitioning method. This way, we can rewrite the matrix  $\mathbf{L}^{(k)} \in \mathbb{R}^{\frac{N}{2} \times \frac{N}{2}}$  of Equation (7.1) as:

$$\mathbf{L}^{(k)} = \begin{bmatrix} \frac{y_{k,t_1} - y_{k,t_2}}{t_1 - t_2} & \cdots & \frac{y_{k,t_1} - y_{k,t_N}}{t_1 - t_N} \\ \vdots & \ddots & \vdots \\ \frac{y_{k,t_{N-1}} - y_{k,t_2}}{t_{N-1} - t_2} & \cdots & \frac{y_{k,t_{N-1}} - y_{k,t_N}}{t_{N-1} - t_N} \end{bmatrix}. \quad (8.8)$$

Considering that the signals are regularly sampled with a sampling period  $\Delta = t_n - t_{n-1}$ , for  $n = 1, \dots, N$ , Equation (8.8) becomes:

$$\mathbf{L}^{(k)} = \begin{bmatrix} \frac{y_{k,t_1} - y_{k,t_2}}{-\Delta} & \cdots & \frac{y_{k,t_1} - y_{k,t_N}}{-(N-1)\Delta} \\ \vdots & \ddots & \vdots \\ \frac{y_{k,t_{N-1}} - y_{k,t_2}}{(N-3)\Delta} & \cdots & \frac{y_{k,t_{N-1}} - y_{k,t_N}}{-\Delta} \end{bmatrix} \quad (8.9)$$

where each element is given by:

$$\ell_{i,j}^{(k)} = \frac{y_{k,t_{2i-1}} - y_{k,t_{2j}}}{[2(i-j)-1]\Delta}. \quad (8.10)$$

Note that this formulation can be easily adapted to signals that are irregularly sampled. For this other scenario, the denominator  $[2(i-j)-1]\Delta$  in (8.10) is replaced by  $\Delta_{ij} = t_{2i-1} - t_{2j}$ . Since in general the signals are regularly sampled, the formulation of (8.10) will be kept.

For a given matrix  $\mathbf{E}^{(k)} \in \mathbb{R}^{I \times J}$ , with a probably non-Löwner structure, its projection onto the Löwner subspace can be obtained by minimizing the LS cost function given by [21]:

$$F(\mathbf{a}, \mathbf{b}) = \sum_{i=1}^{N/2} \sum_{j=1}^{N/2} \left[ e_{i,j}^{(k)} - \frac{a_i - b_j}{\Delta[2(i-j)-1]} \right]^2. \quad (8.11)$$

where  $a_i = \hat{y}_{k,t_{2i-1}}$  and  $b_j = \hat{y}_{k,t_{2j}}$ , for  $i, j = 1, \dots, N/2$ , with  $\hat{\mathbf{y}}_k$  being the estimation of  $\mathbf{y}_k$ .

Taking the derivative of  $F$  with respect to an arbitrary variable  $a_p$  we have:

$$\sum_{j=1}^{N/2} 2 \left[ e_{p,j}^{(k)} - \frac{a_p - b_j}{\Delta[2(p-j)-1]} \right] \left[ \frac{-1}{\Delta[2(p-j)-1]} \right] = 0. \quad (8.12)$$

Then,

$$\sum_{j=1}^{N/2} \left[ e_{p,j}^{(k)} + \frac{b_j}{\Delta[2(p-j)-1]} \right] \left[ \frac{-1}{\Delta[2(p-j)-1]} \right] = \sum_{j=1}^{N/2} \left[ \frac{-a_p}{(\Delta[2(p-j)-1])^2} \right]. \quad (8.13)$$

This way, the solution of  $a_p$ , for  $p = 1, \dots, N/2$ , can be given as:

$$\hat{a}_p = \frac{\sum_{j=1}^{N/2} \left[ e_{p,j}^{(k)} + \frac{b_j}{\Delta[2(p-j)-1]} \right] \left[ \frac{1}{\Delta[2(p-j)-1]} \right]}{\sum_{j=1}^{N/2} \left[ \frac{1}{(\Delta[2(p-j)-1])^2} \right]}. \quad (8.14)$$

Similarly, for  $b_p$  we have:

$$\hat{b}_p = \frac{\sum_{i=1}^{N/2} \left[ e_{i,p}^{(k)} - \frac{a_i}{\Delta[2(i-p)-1]} \right] \left[ \frac{1}{\Delta[2(i-p)-1]} \right]}{-\sum_{i=1}^{N/2} \left[ \frac{1}{(\Delta[2(i-p)-1])^2} \right]}. \quad (8.15)$$

The necessary conditions for optimality can be expressed as:

$$\begin{cases} \hat{a}_p - \alpha_p^{-1} \sum_{j=1}^{N/2} u_{p,j} b_j = z_p \\ \hat{b}_p + \beta_p^{-1} \sum_{i=1}^{N/2} v_{i,p} a_i = w_p \end{cases} \quad (8.16)$$

for  $p = 1, \dots, N/2$ , where:

$$\alpha_p = \sum_{j=1}^{N/2} u_{p,j}, \text{ with } u_{p,j} = 1/\{\Delta[2(p-j)-1]\}^2 \quad (8.17)$$

$$\beta_p = \sum_{i=1}^{N/2} v_{i,p}, \text{ with } v_{i,p} = -1/\{\Delta[2(i-p)-1]\}^2 \quad (8.18)$$

and

$$z_p = \left\{ \sum_{j=1}^{N/2} \frac{y_{p,j}}{\Delta[2(p-j)-1]} \right\} \alpha_p^{-1} \quad (8.19)$$

$$w_p = \left\{ \sum_{i=1}^{N/2} \frac{y_{i,p}}{\Delta[2(i-p)-1]} \right\} \beta_p^{-1}. \quad (8.20)$$

This way, a system of linear equations can be solved in order to estimate  $\hat{\mathbf{a}} = [\hat{a}_1, \dots, \hat{a}_{N/2}]$  and  $\hat{\mathbf{b}} = [\hat{b}_1, \dots, \hat{b}_{N/2}]$ :

$$\begin{bmatrix} \mathbf{I}_{N/2} & -\text{diag}(\boldsymbol{\alpha}^{-1})\mathbf{U} \\ \text{diag}(\boldsymbol{\beta}^{-1})\mathbf{V}^T & \mathbf{I}_{N/2} \end{bmatrix} \begin{bmatrix} \hat{\mathbf{a}} \\ \hat{\mathbf{b}} \end{bmatrix} = \begin{bmatrix} \mathbf{z} \\ \mathbf{w} \end{bmatrix} \quad (8.21)$$

where matrices  $\mathbf{U}$  and  $\mathbf{V}$ , and vectors  $\boldsymbol{\alpha}$ ,  $\boldsymbol{\beta}$ ,  $\mathbf{z}$  and  $\mathbf{w}$  are constructed from  $u_{p,j}$ ,  $v_{i,p}$ ,  $\alpha_p$ ,  $\beta_p$ ,  $z_p$  and  $w_p$  in (8.16), (8.17), (8.18), (8.19) and (8.20), respectively. Note that this linear system has an infinite number of solutions, because the block matrix of (8.21) has rank  $N - 1$ , as a consequence of the vertical shift invariance of the Löwner structure. However, without loss of generality, we can assume that the first sample is null, i.e.,  $a_1 = 0$ , this way the linear system has now  $(N - 1)$  variables, providing now a unique solution. A matrix with assured Löwner structure can be then reconstructed from  $\hat{\mathbf{a}}$  and  $\hat{\mathbf{b}}$  [21]. It is important here to highlight that the resulting matrix is the desired projection (that is, not only it has the desired structure, but is the closest one to the input matrix among all Löwner matrices).

Table 8.5: Parameters of the synthetic AA signal models

Model	P	x	$\Delta x$	$f_x$	$F_s$	$f_0$	$\Delta f$	$F_f$
<b>Top</b>	5	150	50	0.08	1000	6	0.2	0.10
<b>Bottom</b>	3	60	18	0.50	1000	8	0.3	0.23

### 8.4.2 Synthetic AF data

Having derived the LCAGL algorithm, it is now presented some numerical results with synthetic data, which are convenient for assessing its performance. This assessment is carried out using two different synthetic signals that simulate persistent AF recordings. Both signals contain 12 leads, generated by a Gaussian mixing matrix and 3 sources: AA, VA, and a noise source.

To simulate the VA signals, two synthetic QRS complexes modeled by rational functions are generated according to the model function proposed in [4], presented in Section 1.3. Two synthetic QRS models with parameters  $a = 0.8$ ,  $m = 2$ , and  $\theta = \{\pi/2, 0\}$  are generated. To simulate the AA signal during AF, the model proposed in [101] that mimics the f waves is used. Two synthetic f-wave models are generated with the parameters presented in Table 8.5

To simulate the interference typically present in an ECG, additive white Gaussian noise (AWGN) with zero-mean and variance  $\sigma^2$ , is introduced. Finally, the mixing matrix is also generated according to a Gaussian distribution, with scaling factors chosen to obtain an average power ratio between the signals consistent with clinical ECGs, as previously described in Section 1.3.

One generated ECG signal mimics the challenging scenario where the AA is weak, while the other synthetic signal mimics the scenario where the RR interval is short, as in the experiments of Chapter 7. Both synthetic AF ECG signals are illustrated in Figure 8.8.

The NMSE in dB between the estimated and original signals is computed to evaluate estimation quality. This performance index can be computed because the ground-truth is known in this experiment. As LCAGL is relatively robust to initialization, no Monte Carlo runs are performed and the value of  $\gamma$  that provided the best solution is chosen.

Figure 8.9 shows the VA estimates (blue dashed line) and the respective ground-truths (gray solid line) for the two synthetic signals along with the computed error described previously and the rank of the block. The low NMSE shows that a successful estimation is achieved while the Löwner structure of the block is guaranteed. Also, one can see that the rank of the block increases with the number of QRS complexes in the segment, as expected, since the signal has more transient components, needing more poles to be well modeled.

### 8.4.3 Real AF Database and Experimental Setup

All the recordings belong to the PERSIST database and are preprocessed as described in Section 1.3. Experiments are performed using 20 segments of ECG recordings from 20 different patients suffering from persistent AF, where 10 of these segments have a disorganized and/or weak AA, and the other 10 have very short RR intervals. To exploit all spatial diversity while reducing the computational cost, only 8 independent leads are processed (I, II, V1-V6) for all tensor-based techniques. The two types of segments used in these experiments are illustrated in lead V1 in Figure 8.10 (solid lines). Basically, two types of recordings: short RR intervals (top line) and disorganized/weak AA (bottom

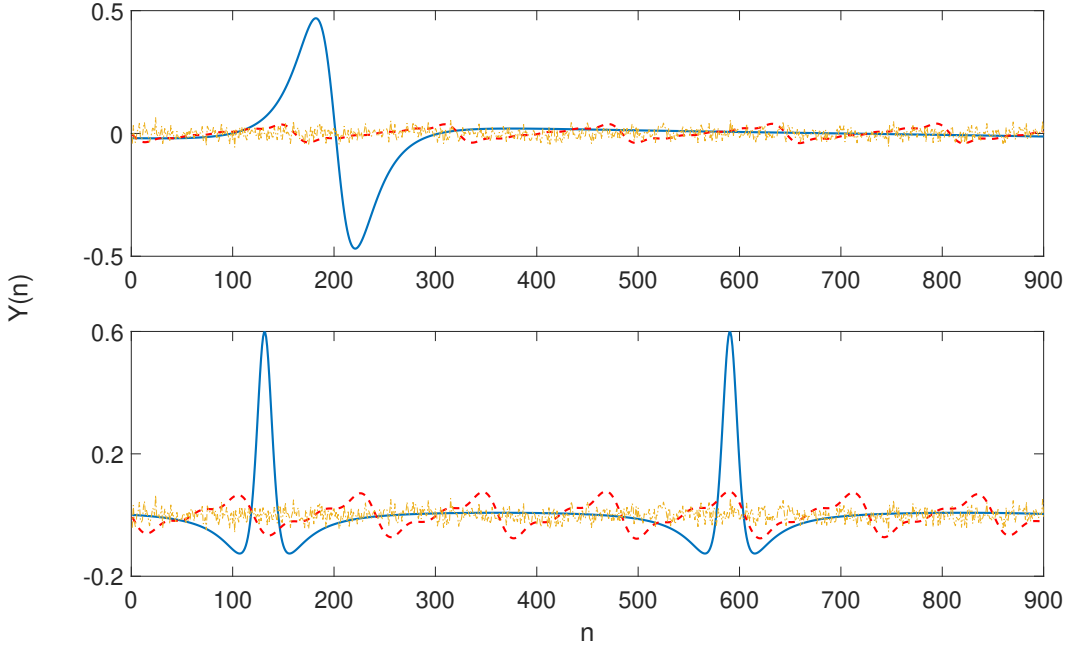


Figure 8.8: Synthetic AF ECG models simulating the challenging cases where the AA signal is weak (Top) and the RR intervals are short (Bottom). The blue, red and yellow lines represent the VA, AA and noise interference, respectively.

line), as when studying the Löwner-BTD method in Chapter 7. The physiological characteristics of the observed 20-patient population are described on Table 8.6. It must be reported that there are missing data values for one patient regarding AF history and for two patients regarding LA diameter. As before, such values were replaced by the average.

Table 8.6: Overall physiological characteristics of the 20-patient population used in the experiments with LCAGL.

Patient characteristics	$\mu \pm \sigma$	Min	Max
Age (years)	$60.8 \pm 11.5$	38	78
Height (cm)	$176.9 \pm 7.9$	154	193
Weight (kg)	$84.5 \pm 13.2$	64	120
AF History (months)	$73.9 \pm 57.8$	3.5	228
LA Diameter (mm)	$46.4 \pm 6.1$	36	58

The 10 segments with disorganized and/or weak AA, from patients P1 to P10 are composed by one heartbeat, i.e., the QRS complex followed by the T wave and the visible f waves, and have between 0.8 and 1.7 seconds. The other 10 segments with short RR intervals from patients P11 to P20 have 1.5 seconds of duration with at least 2 QRS complexes. All the 20 segments are downsampled by a factor of 10, since this significantly reduces the computing cost of processing them without any noticeable loss of quality, as the signals' energy is concentrated in lower frequencies [20].

The NLS approach with the Gauss-Newton method used in the experiments is available in Tensorlab MATLAB Toolbox [105] and is set up as in [27]. As this method is often very sensitive to initialization, 10 Monte Carlo runs are performed for each segment

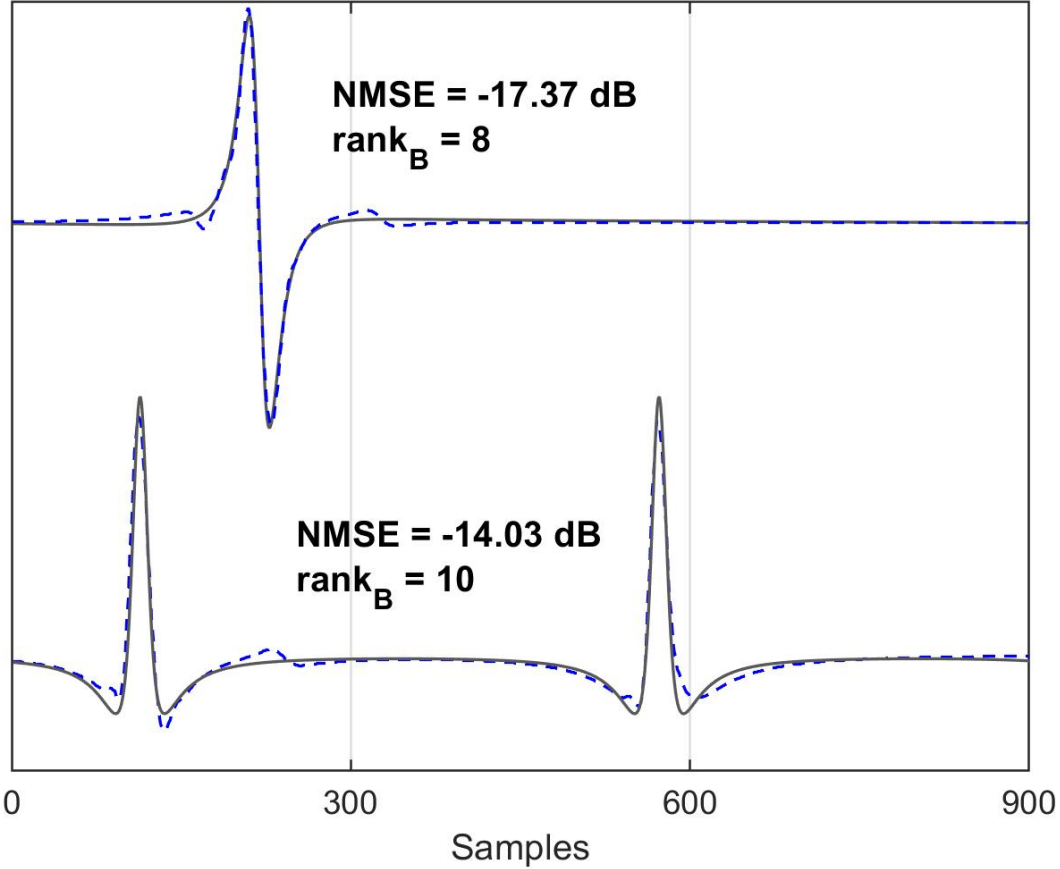


Figure 8.9: Original and estimated VA signals in blue dashed and gray solid lines, respectively, along with the NMSE (dB) between them and the rank of its block,  $\text{rank}_B$ .

and the best solution regarding the AA extraction is chosen. For CAGL and LCAGL, no Monte Carlo runs are needed and the value of  $\gamma$  that yields the best solution is chosen.

#### 8.4.3.1 Segments with disorganized and/or weak AA

In Figure 8.11, we can see the observed recording, the estimated VA and AA of the processed segment of Patient P2 by LCAGL, for a chosen value of  $\gamma$  that gave the best source separation. The segments are shown now in lead V1 for a better clarity of the estimated AA, shown in time domain on the left and in frequency domain on the right, with a DF equal to 6.67 Hz, typical of AA. It can be seen that the SC provided by LCAGL is 58.73% and  $P(r)$  value equal to  $2.02 \times 10^{-4} \text{ mV}^2$ , while the ones provided using the Löwner-BTD computed by the NLS method, choosing the best match  $(R, L_r)$ , are 5.36% and  $1.59 \times 10^{-4} \text{ mV}^2$ , respectively, for the same segment. It should be noted that the Hankel-BTD computed by CAGL was not able to extract the AA from this recording, nor from any other used recording characterized by a disorganized and/or weak AA. Indeed, Hankel-BTD attempts to model the AA present in the recording, which is a difficult task under these conditions. Due to the weak AA amplitude, its estimate is basically a straight line as shown in Figure 8.10 (Top).

Expanding the previous result for the population of 10 patients with segments pre-

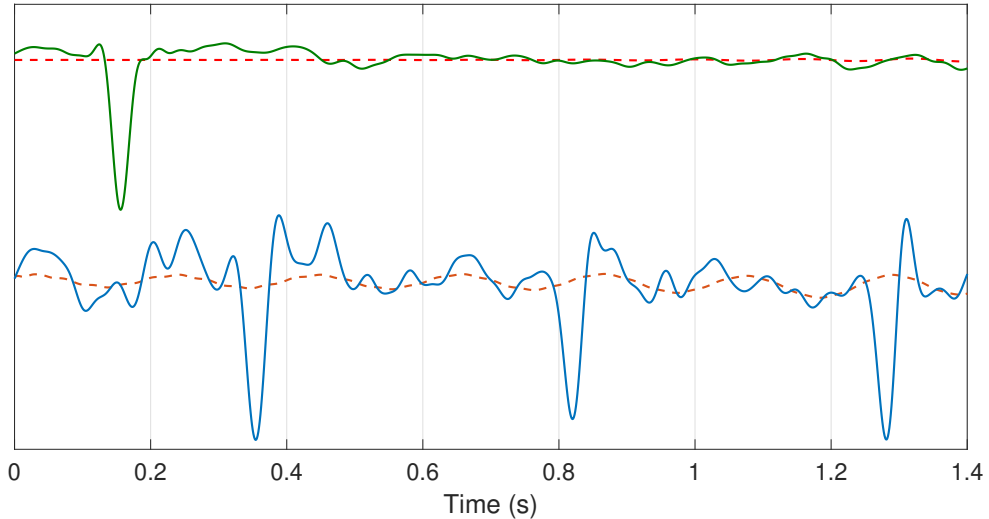


Figure 8.10: Top lines: an example of a single heartbeat segment of an AF ECG recording with a weak AA signal (solid green) and its respective AA signal estimate (dashed red) by the Hankel-BTD method CAGL. Bottom lines: an example of an AF ECG recording used in these experiments with 3 QRS complexes (solid blue) and its respective AA signal estimate (dashed orange), also by CAGL. It can be seen that the Hankel-based method fails to perform the AA extraction.

senting this particular characteristic, Figure 8.12 (Top) shows the SC values of the AA source estimated by the Löwner-BTD computed by the NLS method and LCAGL, for each patient. Regarding this AA quality index, LCAGL outperformed the NLS method in all but patient P4, where the SC of NLS is 1% higher than the one provided by LCAGL. In addition, the NLS method is not able to successfully extract the AA from patient P7, and CAGL could not successfully extract the AA from any of the 10 observed patients, as stated before. Also, the average of the SC over the 10 observed patients is 45.48% for LCAGL, whereas for the NLS method this value is 27.12%.

Figure 8.13 shows how the  $P(r)$  values vary through the population of patients for both Löwner-based methods. No significant difference between the methods can be observed. However, a considerable difference is observed between the two patient populations. The  $P(r)$  of the patients with a disorganized and/or weak AA signal is lower than the ones characterized by short RR intervals and varies in a shorter range.

#### 8.4.3.2 Segments with short RR intervals

Figure 8.12 (Bottom) shows the SC values of the AA source estimated by the Löwner-BTDs computed by the NLS method and LCAGL, for each patient whose segments are characterized by short RR intervals. In 6 out of the 10 patients of this population, LCAGL provided an AA estimate with considerably higher SC than NLS, while for the other 4 patients the SCs of both methods are practically the same. More precisely, for those 4 patients LCAGL produces a slightly higher SC value (around 1%). In addition, the mean SC over these 10 patients is 45.72% for the LCAGL, whereas for the NLS method it is 39.25%.

Figure 8.14 shows the VA and AA estimates of the processed segment in lead V1 of patient 20. One can see that the several QRS complexes are well estimated, resulting in a clear AA signal, when subtracted from the original ECG. The SC provided by LCAGL

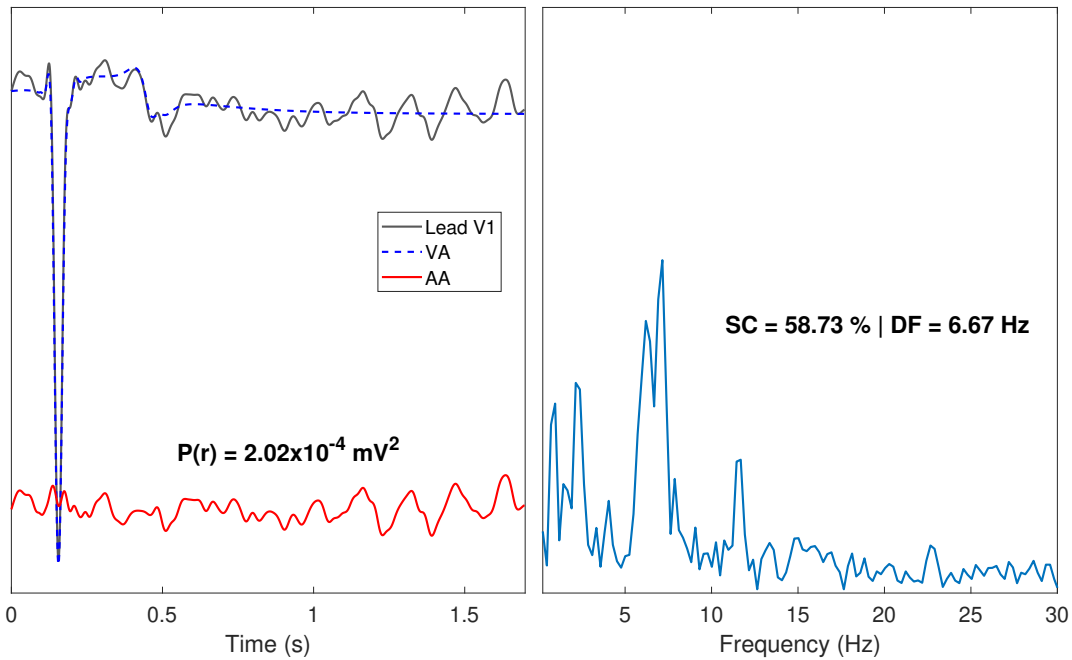


Figure 8.11: Left: Original recording, VA and AA estimates in lead V1 by LCAGL of Patient P2 in time domain. Right: Power spectrum of AA estimate. The AA signal is vertically shifted for clarity.

is 52.48%, practically equal to the one using the NLS method, choosing the best match  $(R, L_r)$ , that is 52.45%, for the same segment. LCAGL provides a slightly stronger  $P(r)$ , than the NLS method, which yields  $3.11 \times 10^{-3} \text{ mV}^2$  for this segment.

Figure 8.15 shows the observed segment of Patient P18 in lead V1 and compares AA source estimations by the tensor-based methods. The AA estimate by CAGL (blue line) is deformed, probably due to the presence of 2 QRS complexes and the shape of the AA that may not be well approximated by an all-pole model, hampering the AA extraction, which loses its typical physiological shape, as happens also in Figure 8.10 (Bottom). Although the AA source estimated by NLS is better than the one produced by imposing the Hankel structure, it contains some ventricular residuals, due to an inaccurate VA source estimation, and seems to be out of phase relative to the true AA present in the recording. Finally, it can be seen that for this segment, LCAGL is the method that provides the best VA cancellation from the original recording, yielding the most accurate AA estimate (green line).

It is valid to state that, for all but patients P8 and P17, both Löwner-based methods (NLS and LCAGL) provided the same DF for the AA source estimate.

Before concluding this chapter, it is important to highlight that other classical techniques that focus on estimating the VA and subtract it from the ECG to acquire the AA, as ABS and ASVC, do not work in these cases of short recording, as they need long-duration ones to perform an accurate VA estimation.

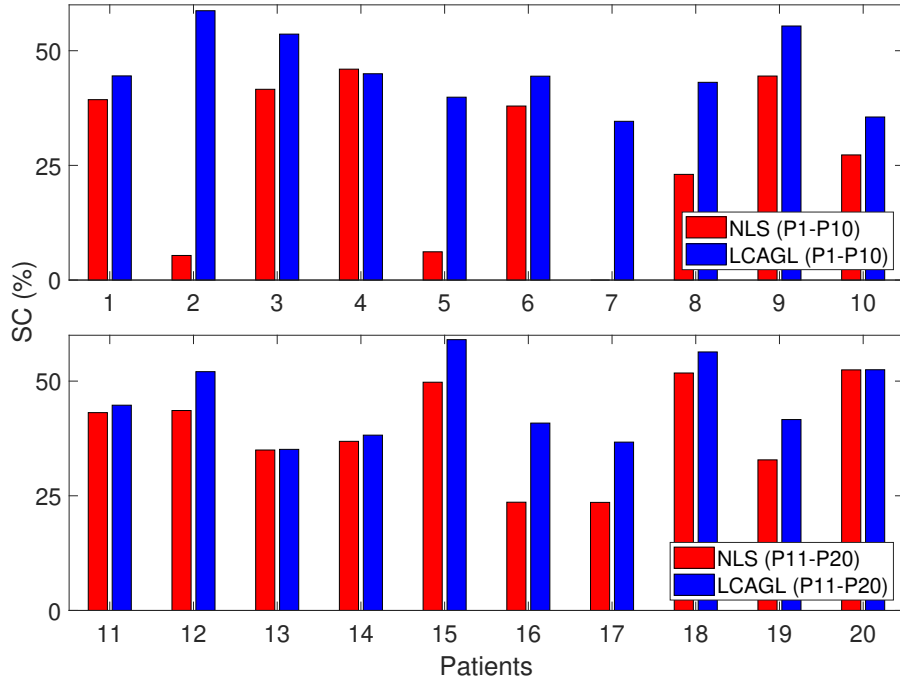


Figure 8.12: SC values (%) of the AA source estimated by NLS and LCAGL for each patient of the observed database. Top: patients P1-P10 with segments presenting disorganized and/or weak AA signals. Bottom: patients P11-P20 whose segments are characterized by short RR intervals.

## 8.5 Summary

This chapter presented an improved algorithm to compute the BTD, named AGL, and its Hankel-constrained version, named CAGL. The main advantage of AGL over the existing algorithms is the simultaneous estimation of the model factors and model structure of the BTD tensor, as well as more robustness to initialization. CAGL was first proven to be a successful AA extraction tool in synthetic and real AF ECG recordings, being able to ensure the Hankel structure of the matrix factors at the end of the computation. The estimated matrix factor rank associated with AA was also proposed as a novel index to measure AF complexity in short recordings, validated in complexity evolution in CA procedures. Later in this chapter, it was derived the Löwner-constrained version of AGL, named LCAGL, using an orthogonal projection to ensure the Löwner structure of the matrix factor of BTD. The LCAGL was assessed in synthetic and real AF ECGs of challenging scenarios, common in this arrhythmia, where the Hankel-BTD fails in extracting the AA.

The following chapter concludes the present doctoral thesis by summarizing all the contributions presented so far and describing the prospects of future works.

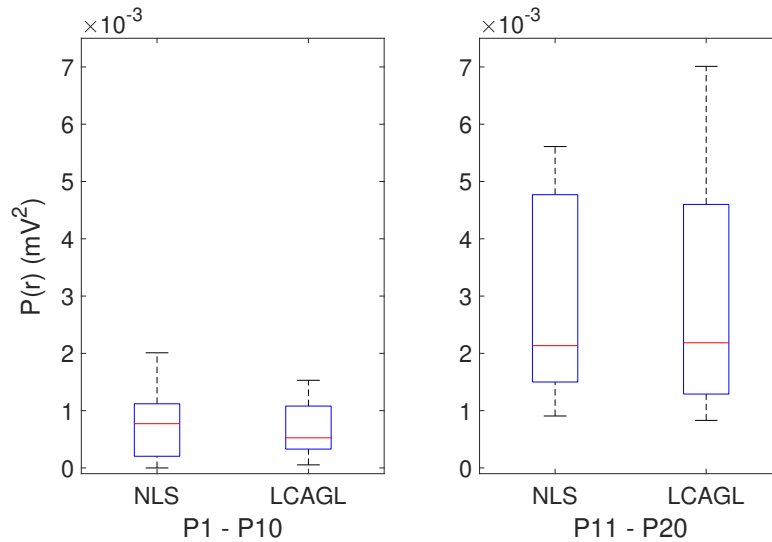


Figure 8.13: The power contribution to lead V1 in  $\text{mV}^2$  of the AA source estimated by NLS and LCAGL for each patient of the observed database. Left: patients P1-P10 with segments presenting disorganized and/or weak AA signals. Right: patients P11-P20 whose segments are characterized by short RR intervals.

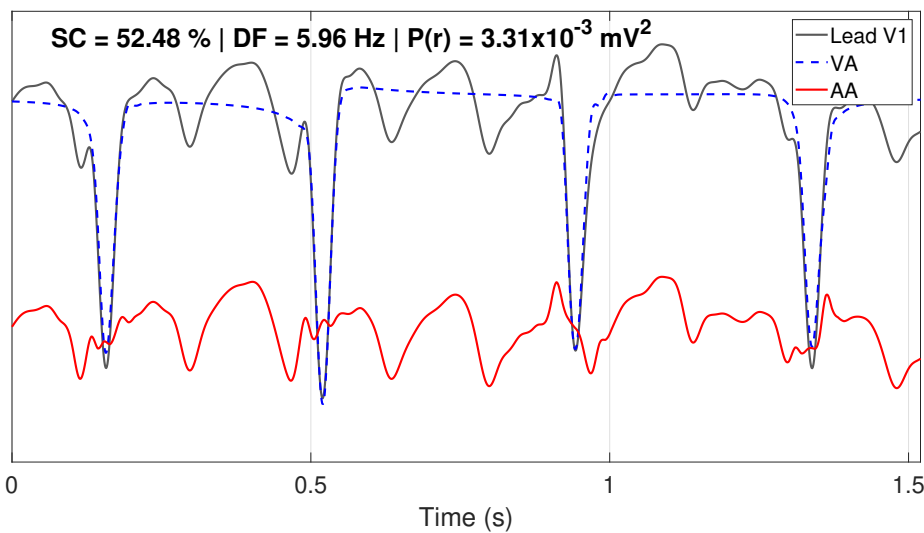


Figure 8.14: Original recording, VA and AA estimates in lead V1 of Patient P20 by LCAGL. The AA signal is vertically shifted for clarity.

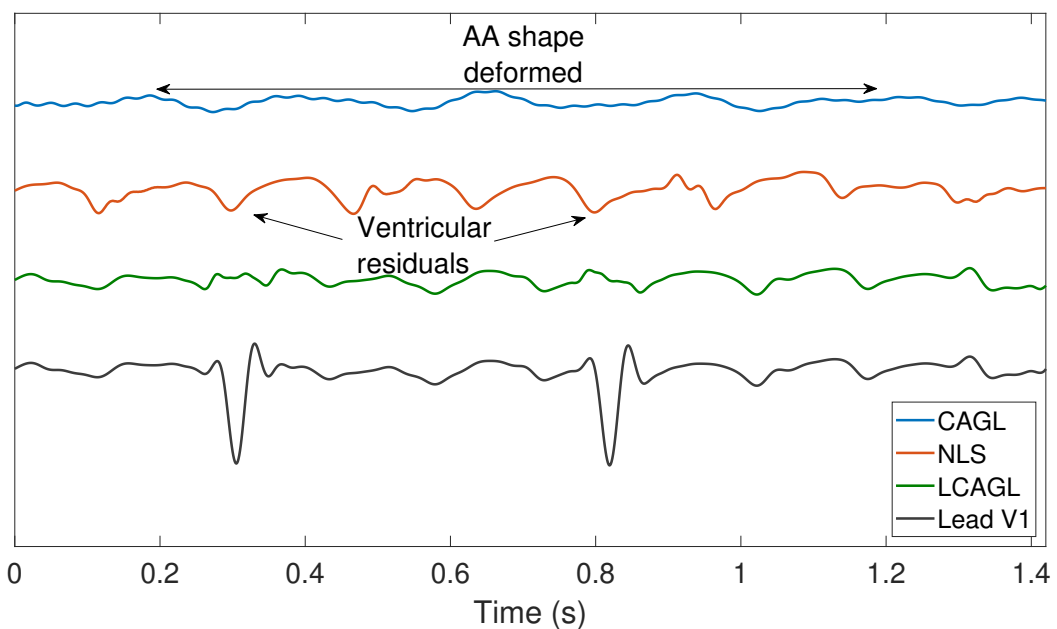


Figure 8.15: Estimated atrial source contribution to lead V1 in a segment of short RR intervals of Patient P18 by CAGL and the Löwner-BTDs computed by the NLS method and LCAGL. AA signal estimates are vertically shifted for clarity.

# Part III

## Conclusions



# Conclusions and Further Work

---

## Contents

<b>9.1</b>	<b>Summary and conclusions</b>	<b>113</b>
<b>9.2</b>	<b>Contributions</b>	<b>114</b>
9.2.1	Quantification of AA content and source classification	114
9.2.2	Patient evaluation of Hankel-BTD performance	114
9.2.3	BTD models for AF analysis	114
9.2.4	Improved algorithms for BTD computation	114
<b>9.3</b>	<b>Discussion and limitations</b>	<b>115</b>
<b>9.4</b>	<b>Further work</b>	<b>116</b>

---

## 9.1 Summary and conclusions

The present doctoral thesis has put forward and investigated several tensor-based approaches as AA extraction tools for persistent AF analysis. Motivated by the importance of AA extraction from ECG in the noninvasive AF analysis and the limitation of matrix-based BSS tools, it has been shown that tensor-based methods, in particular the BTD and its variants, can outperform the matrix approach in this challenging application. Experiments from synthetic and real AF data illustrated the ability of BTD to extract more information from the ECG and provide an AA signal with better estimation quality. Different variants of BTD have been shown to be suitable in different AF scenarios. The Hankel-BTD provides a better performance in cases where the AA can be well represented by exponential models, whereas the Löwner-BTD outperforms its Hankel counterpart in cases where the AA presents an extremely low amplitude or the observed ECG recording has short RR intervals. The coupled Hankel-BTD has been shown to provide an equivalent efficiency to its non-coupled version, with a gain in the computation cost measured by the number of iterations for the algorithm's convergence. Furthermore, the AGL, a recently proposed algorithm to compute BTD shown to overcome the ones present in the literature, has been validated as an AA extraction tool and AA complexity measurement tool. An optimal strategy to deal with its Löwner-constrained version was also put forward and assessed in synthetic and real AF ECGs. This thesis has also dealt with some problems that arise from the AA extraction from AF ECGs. For the problem of AA estimation quality measurement in experiments with real data (where the ground-truth is unknown), new indices have been proposed and assessed, complementing the ones available in the literature. Regarding the AA source classification after performing BSS, several approaches have been assessed, showing satisfactory accuracy. The contributions presented in this doctoral thesis are detailed in the next section.

## 9.2 Contributions

### 9.2.1 Quantification of AA content and source classification

When dealing with the BSS of real AF ECG data, quantifying the quality of AA estimation is a challenging task, since, by definition, the ground-truth is unknown in a blind problem. In order to provide more information about the AA source estimate, three new indices to measure the AA content of a source were proposed and assessed. Furthermore, detecting the AA source among the other sources can often be difficult, as the AA estimate can be mistaken with other low-amplitude interference sources with similar characteristics in the time and frequency domains. Several classification strategies for this problem, including machine learning algorithms and neural networks have been assessed, providing satisfactory accuracy.

### 9.2.2 Patient evaluation of Hankel-BTD performance

The Hankel-BTD was proposed as a potential AA extraction tool, assessed in fixed short AF ECG segments of selected patients suffering from persistent AF. The first aim of the present doctoral thesis was to validate this tensor-based approach as an AA extraction tool through experiments over a population of persistent AF patients and over a whole ECG recording of a patient of the observed population. The impact of the observation window size of the processed ECG signals were also assessed regarding the quality of the AA estimation. It was concluded that this tensor approach indeed provides a better AA extraction than the BSS matrix-based techniques, however, its performance is strongly dependent on its model structure and initialization of its matrix factors.

### 9.2.3 BTD models for AF analysis

ECG recordings with an extremely low AA amplitude and/or short RR intervals are quite common in persistent AF, where the AA signal can not be approximated by exponential models, hampering its estimation by the Hankel-BTD. To bridge this gap, a tensor approach based on the Löwner-BTD was proposed. It consists in estimating the VA and subtract it from the original ECG, resulting in a signal that, ideally, contains the AA. Such approach is supported by the fact that, in persistent AF, the morphology of QRS complexes remains relatively stable and can be well modeled by rational functions. When mapped into Löwner matrices, rational functions present a link with their rank. In addition, consecutive AF ECG segments were modeled as coupled Hankel-BTDs, in order to explore the temporal diversity of segments along with the spatial diversity of the leads. Such alternative BTD models provide a better performance than Hankel-BTD and/or less computational cost in terms of number of iterations

### 9.2.4 Improved algorithms for BTD computation

The AGL is a recently proposed algorithm to compute the BTD that has shown to have some advantages over other methods in the literature, as it is more robust to initialization and can estimate the number of blocks with their ranks (model structure). It was shown that the Hankel-constrained version of AGL, called CAGL, is not only an efficient AA extraction tool but also an AA complexity measurement tool in AF episodes. The latter could improve clinical analysis by providing a noninvasive real-time guidance in CA procedures. Also, an orthogonal strategy to ensure the Löwner structure of BTD matrix factor was also presented, yielding the Löwner-constrained version of AGL, called

LCAGL. Experiments with synthetic data validated LCAGL as an efficient VA estimator, whereas experiments with real data have showed that LCAGL can well extract the AA from the ECG through the proposed Löwner approach, with particular benefit over the Hankel approach, when providing AF ECG segments with weak AA or short RR intervals.

### 9.3 Discussion and limitations

The current state-of-the-art AA extraction methods based on BSS rely on matrix decompositions, which not only require imposing constraints in order to guarantee uniqueness, but limit the number of extracted components by the matrix lowest dimension. The present thesis took a step forward by showing that tensor decompositions provide a better performance with more relaxed constraints. First, the Hankel-BTD is presented to model the AA and extract it from the AF ECG via BSS. Since during AF episodes, the AA can be approximated by all-pole models and when mapped onto Hankel matrices, the number of poles matches their rank, this model suits the characteristics of AA during AF. However, it only works when applied in a segment with sufficient long RR interval, with the f waves well defined. Indeed, when applied in segments that present short RR intervals or fine AF, the Hankel-BTD fails to model the AA, due to the amount of VA interference or the very low AA amplitude. This limitation is dealt with the introduction of the Löwner-BTD, that focus on the VA modeling. The morphology of the VA during AF is not significantly changed and can be well approximated by rational functions that, when mapped onto Löwner matrices, their degree matches the rank of the respective Löwner matrix. The AA is then acquired by suppressing the estimated VA from the AF ECG. Both Hankel- and Löwner-based tensor models work satisfactorily in different scenarios of persistent AF, overcoming the matrix-based BSS methods. However, computing a tensor decomposition may require a high computational cost. Also, applying the decomposition in each AF ECG segment separately avoids the exploitation of the inter-segment diversity. Since AF signals are clearly non-stationary, the exploitation of the inter-segment diversity adds significant information to the decomposition. Assuming that consecutive segments have the same mixing matrix, the coupled Hankel-BTD, assessed for the first time in ECG signal processing, is presented as an AA extraction tool, exploring all the diversity in an AF ECG recording while reducing the computational cost. Only the Hankel structure was used to build the coupled tensors, leaving the coupled Löwner-BTD for further investigation.

Several algorithms exists in the literature to compute the BTD, where the most used ones are based on the NLS approach. Those NLS methods are very sensitive to initialization and require the model parameters of the decomposition as input. Also, there is no guarantee that, at the end of the operations, the structure of the matrix factor will be respected (Hankel, Löwner, etc). The constrained versions of the recently proposed algorithm called AGL deal with such limitations as they are more robust to initialization, guarantee the matrix factor structure at the end of the iterations and estimate the model parameters of the decomposition, i.e., the number of blocks and their multilinear rank. However, those algorithms require a penalization term (used in the formulation of the problem) as input, and an optimal choice of such term remains an open challenge. In addition, constraining the block matrices brings a heavier computational load, due to use of the SLRA algorithm, which is typically iterative, and the arguments that show the convergence of AGL no longer apply for their constrained versions.

Although providing extra information about the AF signal, the proposed indices present some limitations. The power contribution to lead V1, as the name suggests, is

only based on this lead. However, in some AF cases, other leads may provide strong AA content. The NMSE-TQ takes advantage of the AA in the TQ segment that is free from VA, but in some cases of persistent AF the presence of short RR intervals will hamper the assessment quality of this index. The proposed strategies to detect the AA source among the other sources after BSS are also performance-limited, as all of them requires visual inspection to achieve optimality. For this it is important to highlight that is practically impossible to acquire optimality in real-world classification problems.

Overall, this thesis has provided the first comprehensive study of tensor-based signal processing techniques applied to noninvasive AA extraction for AF analysis, including performance evaluation, new models and improved computational algorithms. It is expected that this work will open interesting further perspectives for the application of the powerful tensor approach in this challenging biomedical problem, and beyond.

## 9.4 Further work

The present doctoral thesis had studied and explored several tensor decompositions as noninvasive AA extraction tools for persistent AF analysis. Some challenges that arise from the AA extraction problem, as source classification and AA content quantification were also explored. The results are promising and raise some clinical and mathematical challenges as well as open questions about the tensor-based approach for AF analysis.

Chapter 5 proposed some approaches based on machine learning and neural networks for the automatic selection of the AA source among the other source estimates after performing BSS. These methods provide satisfactory accuracy, but they lack optimality. A line of research to bridge this gap could focus on the development of novel deep learning techniques that have proven their interest in medical areas as radiology and cancer detection, but remain poorly explored in cardiology. In addition, deep learning methods can be used for automatically detecting ablation zones, helping cardiologists to perform catheter ablation in an efficient and cost-effective manner and increasing its probability of long-term success. Hence, another line of research could focus on the proposition of novel indices for AA quantification, aiming to provide additional physiological information about the AA source.

The coupled Hankel-BTD was shown to also have a satisfactory performance, exploring multi-lead and inter-segment diversity simultaneously, which points to the feasibility of its coupled Löwner variant, i.e, coupling segments with the characteristics described in Chapter 7. Also, suitable and more powerful algorithms to compute these coupled tensor decompositions should be developed, aiming to provide better results and identifiability conditions, as for example, a variant of AGL for the coupled case. The coupled Löwner-BTD is also an interesting perspective of further study, in order to deal with consecutive segments that presents short RR intervals or AA with very low amplitude, both very common cases in persistent AF episodes.

CAGL proved to be an efficient AA extraction tool and a potential AA complexity measurement tool. Further works should explore the ability of this algorithm to assess AF complexity in order to guide CA procedures. Also, the proposal and analysis of an automated algorithm for selecting the best penalization parameter in CAGL would be of great interest. Further works should also aim in a study on the convergence of CAGL using a locally optimal SLRA method to impose the linear constraints.

In general, the tensor-based approach has proven useful for AA extraction from the surface ECG during persistent AF episodes. However, using different databases with a larger population of patients would be necessary to confirm and extend the clinical

relevance of the tensor approach in the study of this challenging cardiac arrhythmia. In addition, an extensive comparison of the proposed tensor-based techniques with the methods based on QRST suppression should also be the focus of further works, as the most recent methods for AA extraction are based on VA cancellation.



# Bibliography

- [1] E. Acar, Y. Levin-Schwartz, V. D. Calhoun, and T. Adali. ACMTF for fusion of multi-modal neuroimaging data and identification of biomarkers. In *Proceedings of the 25th European Signal Processing Conference - EUSIPCO-2017*, Kos, Greece, 2017.
- [2] R. Alcaraz and J. J. Rieta. Adaptive singular value cancellation of ventricular activity in single-lead atrial fibrillation electrocardiograms. *Physiological measurement*, 29(12):1351–1369, 2008.
- [3] M. Balandat, B. Karrer, D. R. Jiang, S. Daulton, B. Letham, A. G. Wilson, and E. Bakshy. BoTorch: Programmable bayesian optimization in PyTorch. *ArXiv*, 2019.
- [4] G. Bognár and F. Schipp. Geometric interpretation of QRS complexes in ECG signals by rational functions. *Annales Universitatis Scientiarum Budapestinensis de Rolando Eötvös Nominatae Sectio Computatorica*, 47:155–166, 2018.
- [5] D. L. Boley, F. T. Luk, and D. Vandevenoerde. Vandermonde factorization of a Hankel matrix. In *Proceedings of the Workshop on Scientific Computing*, Hong Kong, 1997.
- [6] B. E. Boser, I. M. Guyon, and V. N. Vapnik. A training algorithm for optimal margin classifiers. In *Proceedings of the 5th Annual Workshop on Computational Learning Theory - COLT-1992*, pages 144–152, Pittsburgh, U.S.A, 1992.
- [7] R. Bro. PARAFAC. tutorial and applications. *Chemometrics and Intelligent Laboratory Systems*, 38(2):149–171, 1997.
- [8] J. A. Cadzow. Signal enhancement-a composite property mapping algorithm. *IEEE Transactions on Acoustics, Speech, and Signal Processing*, 36(1):49–62, 1988.
- [9] J. D. Carroll and J. Chang. Analysis of individual differences in multidimensional scaling via an n-way generalization of “Eckart-Young” decomposition. *Psychometrika*, 35:283–319, 1970.
- [10] F. Castells, J. J. Rieta, J. Millet, and V. Zarzoso. Spatiotemporal blind source separation approach to atrial activity estimation in atrial tachyarrhythmias. *IEEE Transactions on Biomedical Engineering*, 52(2):258–267, 2005.
- [11] Y. J. Chen, S. A. Chen, Y. C. Chen, H. I. Yeh, P. Chan, M. S. Chang, and C. I. Lin. Effects of rapid atrial pacing on the arrhythmogenic activity of single cardiomyocytes from pulmonary veins: implication in initiation of atrial fibrillation. *Circulation*, 104(23):2849–2854, 2001.
- [12] E. M. Cherry, J. R. Ehrlich, S. Nattel, and F. H. Fenton. Pulmonary vein reentry—properties and size matter: Insights from a computational analysis. *Heart Rhythm*, 4(12):1553–1562, 2007.
- [13] G. D. Clifford, F. Azuaje, P. McSharry, et al. *Advanced methods and tools for ECG data analysis*. Boston: Artech House, 2006.

- [14] P. Comon. Independent component analysis, a new concept? *Signal Processing*, (36):287–314, 1994.
- [15] P. Comon. Tensors : A brief introduction. *IEEE Signal Processing Magazine*, 31(3):44–53, 2014.
- [16] P. Comon and C. Jutten. *Handbook of Blind Source Separation: Independent component analysis and applications*. Academic Press, 2010.
- [17] Z. Cui, W. Chen, and Y. Chen. Multi-scale convolutional neural networks for time series classification. *ArXiv*, abs/1603.06995, 2016.
- [18] H. Dai, S. Jiang, and Y. Li. Atrial activity extraction from single lead ECG recordings: Evaluation of two novel methods. *Computers in Biology and Medicine*, 43(3):176–183, 2013.
- [19] A. L. F. de Almeida and G. Favier. Double Khatri–Rao space-time-frequency coding using semi-blind PARAFAC based receiver. *IEEE Signal Processing Letters*, 20(5):471–474, 2013.
- [20] J. H. de M. Goulart, P. M. R. de Oliveira, R. C. Farias, V. Zarzoso, and P. Comon. Alternating group lasso for block-term tensor decomposition and application to ECG source separation. *IEEE Transactions on Signal Processing*, 68:2682–2696, 2020.
- [21] P. M. R. de Oliveira, J. H. de M. Goulart, C. A. R. Fernandes, and V. Zarzoso. Persistent atrial fibrillation analysis using a tensor decomposition with Löwner constraints. *IEEE Journal of Selected Topics in Signal Processing*, submitted.
- [22] P. M. R. de Oliveira, C. A. R. Fernandes, G. Favier, and R. Boyer. PARATUCK semi-blind receivers for relaying multi-hop MIMO systems. *Digital Signal Processing*, 92:127–138, 2019.
- [23] P. M. R. de Oliveira and V. Zarzoso. Block term decomposition analysis in long segments of atrial fibrillation ECGs. In *Proceedings of the XXXVI Simpóscio Brasileiro de Telecomunicações e Processamento de Sinais - SBrT-2018*, pages 578–582, Campina Grande, Brazil, 2018.
- [24] P. M. R. de Oliveira and V. Zarzoso. Source analysis and selection using block term decomposition in atrial fibrillation. In *Proceedings of the 14th International Conference on Latent Variable Analysis and Signal Separation - LVA/ICA-2018*, LNCS, pages 46–56, Guildford, United Kingdom, 2018. Springer.
- [25] P. M. R. de Oliveira and V. Zarzoso. Temporal stability of block term decomposition in noninvasive atrial fibrillation analysis. In *Proceedings of the 52nd Annual Asilomar Conference on Signals, Systems, and Computers - ACSSC-2018*, pages 816–820, Pacific Grove, U.S.A, 2018.
- [26] P. M. R. de Oliveira and V. Zarzoso. Block term decomposition of ECG recordings for atrial fibrillation analysis: temporal and inter-patient variability. *Journal of Communication and Information Systems*, 34(1):111–119, 2019.
- [27] P. M. R. de Oliveira and V. Zarzoso. Löwner-based tensor decomposition for blind source separation in atrial fibrillation ECGs. In *Proceedings of the 27th European Signal Processing Conference - EUSIPCO-2019*, pages 1–5, A Coruña, Spain, 2019.

- [28] P. M. R. de Oliveira, V. Zarzoso, and C. A. R. Fernandes. Source classification in atrial fibrillation using a machine learning approach. In *Proceedings of the Computing in Cardiology 2019 - CinC-2019*, pages 1–4, Biopolis, Singapore, 2019.
- [29] P. M. R. de Oliveira, V. Zarzoso, and C. A. R. Fernandes. Coupled tensor model of atrial fibrillation ECG. In *Proceedings of the 28th European Signal Processing Conference - EUSIPCO-2020*, Amsterdam, Netherlands, 2020.
- [30] O. Debals, M. Van Barel, and L. De Lathauwer. Löwner-based blind signal separation of rational functions with applications. *IEEE Transactions on Signal Processing*, 64(8):1909–1918, 2016.
- [31] P. Dolinský, I. András, L. Michaeli, and D. Grimaldi. Model for generating simple synthetic ECG signals. *Acta Electrotechnica et Informatica*, 18(3):3–8, 2018.
- [32] J. Du, C. Yuan, P. Tian, and H. Lin. Channel estimation for multi-input multi-output relay systems using the PARATUCK2 tensor model. *IET Communications*, 10:995–1002, 2016.
- [33] A. Dupre, S. Vincent, and P. A. Iaizzo. Basic ECG theory, recordings, and interpretation. pages 191–201. Springer, 2005.
- [34] J. R. Ehrlich, T. J. Cha, L. Zhang, D. Chartier, P. Melnyk, S. H. Hohnloser, and S. Nattel. Cellular electrophysiology of canine pulmonary vein cardiomyocytes: action potential and ionic current properties. *The Journal of physiology*, 551(3):801–813, 2003.
- [35] L. Faes, G. Nollo, M. Kirchner, E. Olivetti, F. Gaita, R. Riccardi, and R. Antolini. Principal component analysis and cluster analysis for measuring the local organisation of human atrial fibrillation. *Medical and Biological Engineering and Computing*, 39(6):656–663, 2001.
- [36] G. Favier, C. A. R. Fernandes, and A. L. F. de Almeida. Nested Tucker tensor decomposition with application to MIMO relay systems using tensor space-time coding (TSTC). *Signal Processing*, 128:318–331, 2016.
- [37] R. A. Fisher. The use of multiple measurements in taxonomic problems. *Annals of Eugenics*, 7(2):179–188, 1936.
- [38] S. Fridli, L. Lócsi, and F. Schipp. Rational functions systems in ECG processing. In *Proceedings of the 13th International Conference on Computer Aided Systems Theory - EUROCAST-2011*, pages 88–95, Las Palmas de Gran Canaria, Spain, 2012.
- [39] M. Garibaldi and V. Zarzoso. Algorithms for atrial signal extraction in atrial fibrillation ECGs: A comparison based on the correlation between endocardial and surface dominant frequency. In *Proceedings of the 7th International Workshop on Biosignal Interpretation*, Como, Italy, 2012.
- [40] Ary L Goldberger, Luis AN Amaral, Leon Glass, Jeffrey M Hausdorff, Plamen Ch Ivanov, Roger G Mark, Joseph E Mietus, George B Moody, Chung-Kang Peng, and H Eugene Stanley. PhysioBank, PhysioToolkit, and PhysioNet: components of a new research resource for complex physiologic signals. *Circulation*, 101(23):e215–e220, 2000.

- [41] M. Haïssaguerre, P. Jaïs, D. C. Shah, A. Takahashi, M. Hocini, et al. Spontaneous initiation of atrial fibrillation by ectopic beats originating in the pulmonary veins. *New England Journal of Medicine*, 339(10):659–666, 1998.
- [42] X. Han. *Robust low-rank tensor approximations using group sparsity*. PhD thesis, Université de Rennes 1, 2019.
- [43] X. Han, L. Albera, A. Kachenoura, L. Senhadji, and H. Shu. Low rank canonical polyadic decomposition of tensors based on group sparsity. In *2017 25th European Signal Processing Conference (EUSIPCO)*, pages 668–672, 2017.
- [44] X. Han, L. Albera, A. Kachenoura, H. Shu, and L. Senhadji. Block term decomposition with rank estimation using group sparsity. In *2017 IEEE 7th International Workshop on Computational Advances in Multi-Sensor Adaptive Processing (CAMSAP)*, pages 1–5, 2017.
- [45] R. A. Harshman. Foundations of the PARAFAC procedure: Models and conditions for an “explanatory” multi-modal factor analysis. *UCLA Working Papers in Phonetics*, 16:1–84, 1970.
- [46] R. A. Harshman and M. E. Lundy. Uniqueness proof for a family of models sharing features of Tucker’s three-mode factor analysis and PARAFAC/CANDECOMP. *Psychometrika*, 61:133–154, 1996.
- [47] F. L. Hitchcock. The expression of a tensor or a polyadic as a sum of products. *Journal of Mathematics and Physics*, 6:164–189, 1927.
- [48] H. Honjo, M. R. Boyett, R. Niwa, S. Inada, M. Yamamoto, K. Mitsui, T. Horiuchi, N. Shibata, K. Kamiya, and I. Kodama. Pacing-induced spontaneous activity in myocardial sleeves of pulmonary veins after treatment with ryanodine. *Circulation*, 107(14):1937–1943, 2003.
- [49] B. Hunyadi, W. Van Paesschen, M. De Vos, and S. Van Huffel. Fusion of electroencephalography and functional magnetic resonance imaging to explore epileptic network activity. In *Proceedings of the 24th European Signal Processing Conference - EUSIPCO-2016*, Budapest, Hungary, 2016.
- [50] A. Hyvarinen. Fast and robust fixed-point algorithms for independent component analysis. *IEEE Transactions on Neural Networks*, 10(3):626–634, 1999.
- [51] C. T. January, L. S. Wann, H. Calkins, L. Y. Chen, J. E. Cigarroa, J. C. Cleveland, P. T. Ellinor, M. D. Ezekowitz, M. E. Field, K. L. Furie, P. A. Heidenreich, K. T. Murray, J. B. Shea, C. M. Tracy, and C. W. Yancy. 2019 AHA/ACC/HRS focused update of the 2014 AHA/ACC/HRS guideline for the management of patients with atrial fibrillation. *Journal of the American College of Cardiology*, 74(1):104–132, 2019.
- [52] J. M. Johnson and T. M. Khoshgoftaar. Survey on deep learning with class imbalance. *Journal of Big Data*, 6(27), 2019.
- [53] I. T. Jolliffe. *Principal Component Analysis*. Wiley Online Library, 2005.
- [54] J. L. Wells Jr., R. B Karp, N. T. Kouchoukos, W. A. H. Maclean, T. N. James, and A. L. Waldo. Characterization of atrial fibrillation in man: studies following open heart surgery. *Pacing and Clinical Electrophysiology*, 1(4):426–438, 1978.

- [55] A. Kennedy, D. D. Finlay, D. Guldenring, R. Bond, K. Moran, and J. McLaughlin. The cardiac conduction system: Generation and conduction of the cardiac impulse. *Critical Care Nursing Clinics of North America*, 28(3):269–279, 2016.
- [56] P. Kirchhof, S. Benussi, D. Kotecha, A. Ahlsson, D. Atar, B. Casadei, M. Castella, H. C. Diener, H. Heidbuchel, J. Hendriks, G. Hindricks, A. S. Manolis, J. Oldgren, B. A. Popescu, U. Schottenand B. Van Putte, P. Vardas, and ESC Scientific Document Group. 2016 ESC Guidelines for the management of atrial fibrillation developed in collaboration with EACTS. *European Heart Journal*, 37(38):2893–2962, 2016.
- [57] P. Kirchhof and H. Calkins. Catheter ablation in patients with persistent atrial fibrillation. *European Heart Journal*, 38(1):20–26, 2016.
- [58] T. G. Kolda and B. W. Bader. Tensor decompositions and applications. *SIAM Review*, 51(3):455–500, 2009.
- [59] B. P. Krijthe, A. Kunst, E. J. Benjamin, G. Y. H. Lip, O. H. Franco, A. Hofman, J. C. M. Witteman, B. H. Stricker, and J. Heeringa. Projections on the number of individuals with atrial fibrillation in the European Union, from 2000 to 2060. *European heart journal*, 34(35):2746—2751, 2013.
- [60] D. E. Krummen, S. Hebsur, J. Salcedo, S. M. Narayan, G. G. Lalani, and A. A. Schricker. Mechanisms underlying AF: Triggers, rotors, other? *Current Treatment Options in Cardiovascular Medicine*, 17(4):1–16, 2015.
- [61] D. E. Krummen, V. Swarup, and S. M. Narayan. The role of rotors in atrial fibrillation. *Journal of Thoracic Disease*, 7(2), 2015.
- [62] J. B. Kruskal. Three-way arrays: rank and uniqueness of trilinear decompositions, with application to arithmetic complexity and statistics. *Linear Algebra and its Applications*, 18(2):95–138, 1977.
- [63] L. De Lathauwer. *Signal processing based on multilinear algebra*. PhD thesis, Katholieke Universiteit Leuven, 1997.
- [64] L. De Lathauwer. Decompositions of a higher-order tensor in block terms – Part II: Definitions and uniqueness. *SIAM Journal on Matrix Analysis and Applications*, 30(3):1033–1066, 2008.
- [65] L. De Lathauwer. Blind separation of exponential polynomials and the decomposition of a tensor in rank- $(l_r, l_r, 1)$  terms. *SIAM Journal on Matrix Analysis and Applications*, 32(4):1451–1474, 2011.
- [66] P. Langley, J. P. Bourke, and A. Murray. Frequency analysis of atrial fibrillation. In *Proceedings of Computers in Cardiology 2000 - CinC-2000*, pages 65–68, Cambridge, USA, 2000.
- [67] Y. LeCun, Y. Bengio, and G. Hinton. Deep learning. *Nature*, 521:436–444, 2015.
- [68] G. Lee, S. Spence, A. Teh, J. Goldblatt, M. Larobina, V. Atkinson, R. Brown, J. B. Morton, P. Sanders, P. M. Kistler, et al. High-density epicardial mapping of the pulmonary vein-left atrial junction in humans: Insights into mechanisms of pulmonary vein arrhythmogenesis. *Heart Rhythm*, 9(2):258–264, 2012.

- [69] M. Lemay, J. Vesin, A. Oosterom, V. Jacquemet, and L. Kappenberger. Cancellation of ventricular activity in the ECG: Evaluation of novel and existing methods. *IEEE Transactions on Biomedical Engineering*, 54:542–546, 2007.
- [70] S. Levy, G. Breithardt, R. W. F. Campbell, A. J. Camm, J. C. Daubert, M. Allessie, E. Aliot, A. Capucci, F. Cosio, et al. Atrial fibrillation: current knowledge and recommendations for management. *European Heart Journal*, 19(9):1294–1320, 1998.
- [71] T. Lin, K. H. Kuck, F. Ouyang, and R. R. Tilz. First in-human robotic rotor ablation for atrial fibrillation. *European Heart Journal*, 35(22):1432–1432, 2014.
- [72] I. N. Lira, P. M. R. de Oliveira, W. Freitas Jr., and V. Zarzoso. Automated atrial fibrillation source detection using shallow convolutional neural networks. In *Proceedings of the Computing in Cardiology 2020 - CinC-2020*, Rimini, Italy, 2020.
- [73] L. Lócsyi. Approximating poles of complex rational functions. *Acta Universitatis Sapientiae, Mathematica*, 1:169–182, 2009.
- [74] L. Mainardi, L. Sörnmo, and S. Cerutti. *Understanding Atrial Fibrillation: The Signal Processing Contribution*. Morgan & Claypool Publishers, 2008.
- [75] J. Malik, N. Reed, C. Wang, and H. Wu. Single-lead f-wave extraction using diffusion geometry. *Physiological Measurement*, 38:1310–1334, 2017.
- [76] M. Meo. *Spatio-temporal characterization of the surface electrocardiogram for catheter ablation outcome prediction in persistent atrial fibrillation*. PhD thesis, Université Nice Sophia Antipolis, 2013.
- [77] G. K. Moe, W. C. Rheinboldt, and J.A. Abildskov. A computer model of atrial fibrillation. *American Heart Journal*, 67(2):200–220, 1964.
- [78] C. A. Morillo, A. Banerjee, P. Perel, D. Wood, and X. Jouven. Atrial fibrillation: the current epidemic. *Journal of Geriatric Cardiology*, 14:195–203, 2017.
- [79] M. Mørup, L. K. Hansen, and S. M. Arnfred. Algorithms for sparse non-negative TUCKER. *Neural Computation*, 20(8):2112–2131, 2008.
- [80] M. Mørup, L. K. Hansen, C. S. Herrmann, J. Parnas, and S. M. Arnfred. Parallel factor analysis as an exploratory tool for wavelet transformed event-related EEG. *NeuroImage*, 29(3):938–947, 2006.
- [81] J. Pan and W. J. Tompkins. A real-time QRS detection algorithm. *IEEE Transactions on Biomedical Engineering*, 32(3):230–236, 1985.
- [82] J. Park, C. Lee, E. Leshem, et al. Early differentiation of long-standing persistent atrial fibrillation using the characteristics of fibrillatory waves in surface ECG multi-leads. *Scientific Reports*, 2019.
- [83] A. Petrenas, V. Marozas, A. Sološenko, R. Kubilius, J. Skibarkienė, J. Oster, and L. Sörnmo. Electrocardiogram modeling during paroxysmal atrial fibrillation: Application to the detection of brief episodes. *Physiological Measurement*, 38:2058–2080, 2017.

- [84] A. Petrenas, V. Marozas, L. Sörnmo, and A. Lukosevicius. An echo state neural network for QRST cancellation during atrial fibrillation. *IEEE Transactions on Biomedical Engineering*, 59(10):2950–2957, 2012.
- [85] S. S. Po, B. J. Scherlag, W. S. Yamanashi, J. Edwards, J. Zhou, R. Wu, N. Geng, R. Lazzara, and W. M. Jackman. Experimental model for paroxysmal atrial fibrillation arising at the pulmonary vein-atrial junctions. *Heart Rhythm*, 3(2):201–208, 2006.
- [86] D. Raine, P. Langley, E. Shepherd, S. Lord, S. Murray, A. Murray, and J. P. Bourke. Principal component analysis of atrial fibrillation: Inclusion of posterior ECG leads does not improve correlation with left atrial activity. *Medical Engineering & Physics*, 37:251–255, 2015.
- [87] L. N. Ribeiro, A. R. Hidalgo-Muñoz, and V. Zarzoso. Atrial signal extraction in atrial fibrillation electrocardiograms using a tensor decomposition approach. In *Proceedings of the 37th Annual International Conference of the IEEE Engineering in Medicine and Biology Society - EMBC-2015*, pages 6987–6990, Milan, Italy, 2015.
- [88] J. J. Rieta, F. Castells, C. Sánchez, V. Zarzoso, and J. Millet. Atrial activity extraction for atrial fibrillation analysis using blind source separation. *IEEE Transactions on Biomedical Engineering*, 51(7):1176–1186, 2004.
- [89] J. J. Rieta, V. Zarzoso, J. Millet, R. Garcia, and R. Ruiz. Atrial activity extraction based on blind source separation as an alternative to QRST cancellation for atrial fibrillation analysis. In *Proceedings of the Computers in Cardiology 2000 - CinC-2000*, pages 69–72, Cambridge, USA, 2000.
- [90] E. K. Roonizi and R. Sassi. An extended bayesian framework for atrial and ventricular activity separation in atrial fibrillation. *IEEE Journal of Biomedical and Health Informatics*, 21(6):1573–1580, 2017.
- [91] O. Sayadi, M. B. Shamsollahi, and G. D. Clifford. Synthetic ECG generation and bayesian filtering using a Gaussian wave-based dynamical model. *Physiological Measurement*, 31:1309–1329, 2010.
- [92] J. Seitz, C. Bars, G. Théodore, S. Beurtheret, et al. AF ablation guided by spatiotemporal electrogram dispersion without pulmonary vein isolation: A wholly patient-tailored approach. *Journal of the American College of Cardiology*, 69(3):303–321, 2017.
- [93] S. Shkurovich, A. V. Sahakian, and S. Swiryn. Detection of atrial activity from high-voltage leads of implantable ventricular defibrillators using a cancellation technique. *IEEE Transactions on Biomedical Engineering*, 45(2):229–234, 1998.
- [94] N. D. Sidiropoulos, R. Bro, and G. B. Giannakis. Parallel factor analysis in sensor array processing. *IEEE Transactions on Signal Processing*, 48(8):2377–2388, 2000.
- [95] J. Slocum, E. Byrom, L. McCarthy, A. V. Sahakian, and S. Swiryn. Computer detection of atrioventricular dissociation from surface electrocardiograms during wide QRS complex tachycardia. *Circulation*, 72:1028–1036, 1985.

- [96] J. Slocum, A. V. Sahakian, and S. Swiryn. Diagnosis of atrial fibrillation from surface electrocardiograms based on computer-detected atrial activity. *Journal of Electrocardiology*, 25(1):1–8, 1992.
- [97] A. K. Smilde, Y. Wang, and B. R. Kowalski. Theory of medium-rank second-order calibration with restricted-Tucker models. *Journal of Chemometrics*, 8(1):21–36, 1994.
- [98] M. Sørensen and L. De Lathauwer. Coupled canonical polyadic decompositions and (coupled) decompositions in multilinear rank- $(l_{r,n}, l_{r,n}, 1)$  terms - part I: Uniqueness. *SIAM Journal on Matrix Analysis and Applications*, 36:496–522, 2015.
- [99] M. Sørensen and L. De Lathauwer. New uniqueness conditions for the canonical polyadic decomposition of third-order tensors. *SIAM Journal on Matrix Analysis and Applications*, 36:1381–1403, 2015.
- [100] L. Sörnmo, M. Stridh, D. Husser, A. Bollmann, and S. B. Olsson. Analysis of atrial fibrillation: from electrocardiogram signal processing to clinical management. *Philosophical Transactions of the Royal Society A: Mathematical, Physical and Engineering Sciences*, 367(1887):235–253, 2009.
- [101] M. Stridh and L. Sörnmo. Spatiotemporal QRST cancellation techniques for analysis of atrial fibrillation. *IEEE Transactions on Biomedical Engineering*, 48(1):105–111, 2001.
- [102] T. Sueda, K. Imai, O. Ishii, K. Orihashi, M. Watari, and K. Okada. Efficacy of pulmonary vein isolation for the elimination of chronic atrial fibrillation in cardiac valvular surgery. *The Annals of Thoracic Surgery*, 71(4):1189–1193, 2001.
- [103] L. R. Tucker. Some mathematical notes on three-mode factor analysis. *Psychometrika*, 31:279–311, 1966.
- [104] E. Turajlic. A novel algorithm for ECG parametrization and synthesis. In *Proceedings of the 2012 IEEE-EMBS Conference on Biomedical Engineering and Sciences*, pages 927–932, Langkawi, Malaysia, 2012.
- [105] N. Vervliet, O. Debals, L. Sorber, M. Van Barel, and L. De Lathauwer. Tensorlab 3.0, Mar. 2016. Available online.
- [106] A. J. Weinhaus and K. P. Roberts. *Anatomy of the Human Heart*, pages 51–79. Humana Press, 2005.
- [107] P. Welch. The use of fast Fourier transform for the estimation of power spectra: A method based on time averaging over short, modified periodograms. *IEEE Transactions on Audio and Electroacoustics*, 15(2):70–73, 1967.
- [108] M. Yuan and Y. Lin. Model selection and estimation in regression with grouped variables. *Journal of the Royal Statistical Society: Series B (Statistical Methodology)*, 68(1):49–67, 2006.
- [109] V. Zarzoso. *Extraction of ECG Characteristics Using Source Separation Techniques: Exploiting Statistical Independence and Beyond*, pages 15–48. Springer Berlin Heidelberg, 2009.

- [110] V. Zarzoso. Parameter estimation in block term decomposition for noninvasive atrial fibrillation analysis. In *Proceedings of the IEEE International Workshop on Computational Advances in Multi-Sensor Adaptive Processing - CAMSAP-2017*, pages 1–5, Curaçao, Dutch Antilles, 2017.
- [111] V. Zarzoso and P. Comon. Automated extraction of atrial fibrillation activity from the surface ECG using independent component analysis in the frequency domain. In *Proceedings of the World Congress on Medical Physics and Biomedical Engineering*, pages 395–398, Munich, Germany, 2009.
- [112] V. Zarzoso and P. Comon. Robust independent component analysis by iterative maximization of the kurtosis contrast with algebraic optimal step size. *IEEE Transactions on Neural Networks*, 21(2):248–261, 2010.